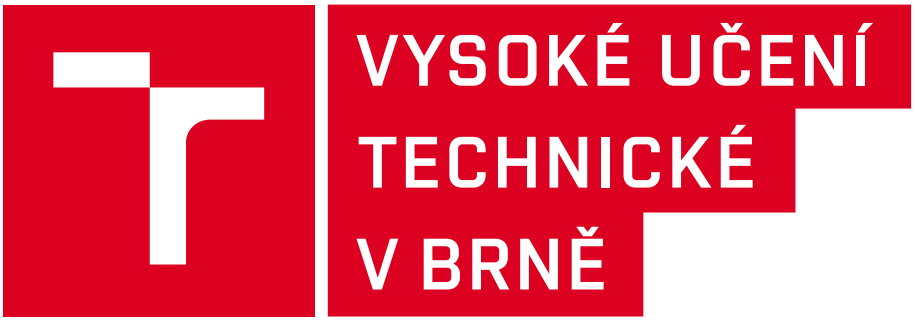

BRNO UNIVERSITY OF TECHNOLOGY
VYSOKÉ UČENÍ TECHNICKÉ V BRNĚ

FACULTY OF MECHANICAL ENGINEERING
FAKULTA STROJNÍHO INŽENÝRSTVÍ

INSTITUTE OF PHYSICAL ENGINEERING
ÚSTAV FYZIKÁLNÍHO INŽENÝRSTVÍ

METASTABLE IRON THIN FILM FOR MAGNETIC METAMATERIALS
PŘÍPRAVA METASTABILNÍCH VRSTEV ŽELEZA PRO MAGNETICKÉ METAMATERIÁLY

MASTER'S THESIS
DIPLOMOVÁ PRÁCE

AUTHOR — **Bc. Jakub Holobrádek**
AUTOR PRÁCE

SUPERVISOR — **Ing. Michal Urbánek, Ph.D.**
VEDOUCÍ PRÁCE

BRNO 2020

BRNO UNIVERSITY OF TECHNOLOGY
FACULTY OF MECHANICAL ENGINEERING

Specification Master's Thesis

Department:	Institute of Physical Engineering
Student:	**Bc. Jakub Holobrádek**
Study programme:	Applied Sciences in Engineering
Study field:	Physical Engineering and Nanotechnology
Supervisor:	**Ing. Michal Urbánek, Ph.D.**
Academic year:	2019/20

Pursuant to Act no. 111/1998 concerning universities and the BUT study and examination rules, you have been assigned the following topic by the institute director Master's Thesis:

Metastable iron thin films for magnetic metamaterials

Concise characteristic of the task:

Magnonics is emerging field of magnetism which investigates the properties of spin waves for their potential use in low–energy consumption information technology. For these applications, the key structure is the so–called magnonic crystals (structures with periodically modulated magnetic properties). Previous work suggests that metastable iron layers which are locally transformable by a focused ion beam are suitable materials for producing such crystals. Despite great progress in the study of this system in recent years, there are still some unanswered questions (the influence of deposition conditions on the magnetic properties of the layer, the influence of the focused ion beam parameters on the transformed structures,…) whose investigation will be the aim of this thesis.

Goals Master's Thesis:

Prepare metastable iron films on copper substrates under different deposition conditions.
Transform them using focused ion beam with alternating parameters (ion dose, scanning strategy, orientation toward the crystallographic directions etc.).
Investigate structural and magnetic properties of transformed structures with a variety of techniques (MOKE, EBSD, LEED, SEM).
Analyze the data and determine parameters which influence the direction and strength of magnetic anisotropy of the transformed structures.

Recommended bibliography:

URBÁNEK, M., L. FLAJŠMAN, V. KŘIŽÁKOVÁ, J. GLOSS, M. HORKÝ, M. SCHMID a P. VARGA. Research Update: Focused ion beam direct writing of magnetic patterns with controlled structural and magnetic properties. APL Materials. 2018, 6(6).

GLOSS, J. Metastable iron-nickel thin films. Dissertation. (Institute of Applied Physics, TU Wien, 2019).

Deadline for submission Master's Thesis is given by the Schedule of the Academic year 2019/20

In Brno,

L. S.

prof. RNDr. Tomáš Šikola, CSc. Director of the Institute	doc. Ing. Jaroslav Katolický, Ph.D. FME dean

Abstract
Magnetic nanostructures are widely investigated for applications in industrial and fundamental research thanks to their interesting properties. One of the concerned scientific disciplines is magnonics – a novel research topic in magnetism focuse on the physics of spin waves, which can be used for fabrication of novel devices for wave-based computing with low power consumption. Fabrication of magnonic structures by a focused ion beam (FIB) is an alternative method to the commonly used lithographic methods. The material used in this work – metastable iron – is able to undergo an ion-beam-induced phase transformation from a paramagnetic fcc to a ferromagnetic bcc phase. One of the properties, which affect the spin-wave propagation, is magnetic anisotropy. This thesis presents the influence of UHV conditions during the deposition of the metastable iron film on the magnetic anisotropy of the structures fabricated via FIB into this film. We also investigate the relationship between FIB parameters, crystallographic properties of the resulting structures, and their magnetic anisotropy.

Abstrakt
Magnetické nanostruktury mají zajímavé vlastnosti, které umožňují jejich aplikace v základním výzkumu i průmyslu. Jednou z těchto vědeckých disciplín je i magnonika - výzkumný obor, který se zabývá fyzikou spinových vln, které lze použít v nediskrétních výpočtech s nízkými ztrátami energie. Výroba magnetických struktur fokusovaným iontovým svazkem (FIB) je alternativní metoda k běžně používaným litografickým metodám. Materiál použitý v této práci - metastabilní železo - je schopen při ozáření iontovým svazkem podstoupit fázovou transformaci z paramagnetické plošně centrované kubické krystalové struktury na feromagnetickou fázi s prostorově centrovanou kubickou krystalovou strukturou. Jednou z vlastností, která ovlivňuje šíření spinových vlny, je magnetická anizotropie. Tato práce představuje vliv depozičních podmínek v ultra vysokém vakuu během přípravy metastabilní železné vrstvy na magnetickou anizotropii struktur vytvořených pomocí FIB do tohoto filmu. Dále prezentujeme souvislosti mezi parametry FIB, krystalografickými vlastnostmi výsledných struktur a jejich magnetickou anizotropií.

Keywords
Metastable iron, magnonics, ion transformation, focus ion beam, crystallography, electron back-scatter diffraction, ultra-hight vacuum, magnetic anisotropy, magnetism

Klíčová slova
Metastabilní železo, magnonika, transformace ionty, fokusovaný iontový svazek, krystalografie, difrakce zpětně odražených elektronů, ultra vysoké vakuum, magnetická anisotropie, magnetizmus

HOLOBRÁDEK, Jakub. *Metastable iron thin film for magnetic metamaterials*. Brno, 2020. 70 p. Diploma thesis. Brno University of Technology. Faculty of Mechanical Engineering. Supervised by Michal URBÁNEK.

I hereby declare that I have written my master's thesis on the theme of *Metastable iron thin film for magnetic metamaterials* independently, under the guidance of the master's thesis supervisor, Ing. Michal Urbánek, Ph.D., and using the technical literature and other sources of information which are all properly quoted in the thesis and detailed in the list of literature at the end of the thesis.

.....	.....
Place and date	Bc. Jakub Holobrádek

Acknowledgment

Chtěl bych poděkovat všem, díky kterým mohla vzniknout tato práce a kteří mě podporovali při jejím psaní. Jmenovitě bych rád poděkoval:
Michalu Urbánkovi, za skvělé vedení diplomové práce, za nesčetné čtení mých kapitol a za trpělivý a konstruktivní přístup obzvlášť v posledních dnech před odevzdáním.
Lukáši Flajšmanovi za zasvěcení do projektu metastabilního železa, ukázaní toho, jak může být vědecká práce fascinující i za možnost vařit si kávu v jeho kávovaru po jeho odjezdu do Finska.
Jonáši Glossovi za seznámení s PINUPem i celou větví projektu věnující se růstu metastabilního železa.
Igoru Turčanovi, Marku Vaňatkovi, Ondrovi Wojewodovi i dalším mladším studentům za skvělé prostředí a atmosféru v magnonické skupině. Igorovi s Ondrou pak i za pomoc s provedením a zpracováním magnetických měření.
Ondřeji Cahovi za několikanásobný pokus změřit na našich strukturách rentgenovou difrakci.
Členům Ceitec PC room crew (Káťa, Ondra, Lázňa, Ivoš, Tesy, Andrej) za společné dopisování diplomových prací i podporu a pomoc, když už měli odevzdáno.
Mému bratrovi Mihalovi za všechny společné zážitky, diskuze, softbalové nadhozy i hektolitry prolitého maté.
Našim rodičům za skvělé dětství, výchovu i podporu ve všem, pro co jsme se v životě rozhodli.
Mojí přítelkyni Emči, za velké pochopení pro moji práci a její nekonečné dokončování, společnou cestu životem i veškerou podporu.
And last but not least to Ulrike Diebold and Michael Schmid for wonderful Erasmus stay at TU Wien.
Thanks to all…

Bc. Jakub Holobrádek

Financial support from the Thermo Fisher Scientific is gratefully acknowledged.
CzechNanoLab project LM2018110 funded by MEYS CR is gratefully acknowledged for the financial support of the measurements/sample fabrication at CEITEC Nano Research Infrastructure.

Contents

1. Introduction **1**

2. Crystallography **3**
2.1. Basics . . . 3
2.1.1. Crystal lattices and systems . . . 3
2.1.2. Miller indices . . . 3
2.1.3. Crystallographic orientation . . . 5
2.2. Crystallography techniques . . . 11
2.2.1. Low-energy electron diffraction . . . 11
2.2.2. X-ray diffraction . . . 12
2.2.3. Electron backscatter diffraction . . . 13
2.2.4. Sofwares for postprocessing of the EBSD data . . . 17

3. Metastable iron-nickel thin films **18**
3.1. Basics and motivations of the project . . . 18
3.2. Growth of metastable iron-nickel thin films . . . 19
3.3. Ion transformation of the metastable iron-nickel layers and FIB direct writing of the magnonics structures . . . 21
3.4. Magnonic applications . . . 23

4. Growth of metastable films **25**
4.1. Metastable film on diamond substrate . . . 25
4.1.1. Preparation of the diamond(100) surface . . . 25
4.1.2. Deposition of the metastable film . . . 26
4.1.3. Discussion and conclusion of the experiment . . . 27
4.2. Metastable film on silicon substrate . . . 28
4.2.1. Preparation of the Si(100) surface . . . 28
4.2.2. Growth of the Cu(100) buffer layer . . . 29
4.2.3. Deposition of the metastable film . . . 30
4.2.4. Discussion and conclusion of the experiment . . . 31
4.3. Influence of the CO backpressure on the magnetic properties of the metastable films deposited on copper substrates . . . 32
4.3.1. Preparation of the Cu(100) surface . . . 33
4.3.2. Deposition of the metastable film . . . 33
4.3.3. Design of the CO experiment . . . 33
4.3.4. Characteristics of microscopes used for fabrication of the ion dose tests . . . 34
4.3.5. Initial ion dose for the fcc-bcc transformation . . . 35
4.3.6. Magnetic anisotropy of the films . . . 36

4.3.7. Types of fcc-bcc transformations . . . 37
4.3.8. Summary of the CO backpressure experiments . . . 37

5. Crystallographic experiments 39
5.1. EBSD measurement workflow . . . 39
5.2. EBSD data processing . . . 40
5.3. Experiment 1: Influence of the FIB energy and number of scans . . . 42
5.3.1. Motivation of the experiment . . . 43
5.3.2. EBSD measurement . . . 43
5.3.3. Summary of the experiment . . . 46
5.4. Experiment 2: Influence of the structure shape . . . 46
5.4.1. Motivation of the experiment . . . 47
5.4.2. EBSD measurement . . . 47
5.4.3. Summary of the experiment . . . 48
5.5. Experiment 3: Influence of the concentricity of scanning . . . 48
5.5.1. Motivation of the experiment . . . 48
5.5.2. EBSD measurement . . . 48
5.5.3. Summary of the experiment . . . 49
5.6. Experiment 4: Influence of the sense and starting direction of scanning . . . 50
5.6.1. Motivation of the experiment . . . 50
5.6.2. EBSD measurement . . . 51
5.6.3. Summary of the experiment . . . 52
5.7. Experiment 5: Influence of the direction of the fast scanning axis . . . 52
5.7.1. Motivation of the experiment . . . 52
5.7.2. EBSD measurement . . . 53
5.7.3. Summary of the experiment . . . 54
5.8. Perspectives of the orientation analysis . . . 54
5.9. XRD measurements . . . 54

6. Magnetic experiments 56
6.1. Magnetic anisotropy mesurement workflow . . . 56
6.2. Influence of FIB energy and number of scans to magnetic anisotropy . . . 56
6.2.1. Motivation of the experiment . . . 57
6.2.2. Magnetic anisotropy measurement . . . 57
6.2.3. Summary of the experiment . . . 58
6.3. Magnetic anisotropy in homogeneous regions . . . 58
6.3.1. Motivation of the experiment . . . 59
6.3.2. Magnetic anisotropy measurement . . . 59
6.3.3. Summary of the experiment . . . 59

7. Discussion of the crystallographic and magnetic results 60
7.1. Influence of different transformation number of scans and FIB energy to magnetic and crystallographic properties . . . 60
7.2. Influence of the direction of the fast scanning axis to the magnetic and crystallographic properties . . . 61
7.3. Overview of alternating FIB parameters and its importance to the resulting properties . . . 62
7.4. XRD measurement perspectives . . . 62

8. Conclusion **63**

References **65**

List of abbreviations **69**

A. Structures fabrication by focus ion beam **i**
A.1. Aligning the sample before the FIB transformation i
A.2. Structures fabrication ii
A.3. Contrast evolution during tilting the sample v

B. Orientation domain analysis **vii**

1. Introduction

Magnetic properties of the materials have fascinated humanity for centuries. This wonderment does not come only from the surprise about observing an invisible force attracting two objects to each other, but also about the applications that can improve everyday life and raise the level of human knowledge. The inventions based on magnetism started in ancient times by magnetic compasses for navigation, and continued by exploring the relationship between magnetism and electricity. Nowadays, a wide range of magnetic applications in information technologies such as hard-drivers or magnetic random access memories (MRAM) are in use.

One of the biggest challenges for today's information technologies is to find devices with high data-transfer speeds and low power consumption. A very promising candidate came from the field of magnonics, where the propagating spin waves can transfer an information [1]. Magnonic approach avoids Joule losses and associated heating in contrary to the transfer of the information by moving electric charges as in conventional devices. In recent years, the investigation of the elementary building blocks of magnonic circuitry and envisioned all magnon on-chip devices is dynamically developing [2]. The discovery of suitable magnonic materials can be the impuls that will bring magnon-based devices to the market.

A potential candidate to such material are nickel-stabilized iron thin films epitaxially grown on copper single crystal [3]. These as-deposited films are paramagnetic and have a face-centered cubic crystal structure. They are referred to as metastable, because they are capable to undergo to ion-beam induced phase transformation to the ferromagnetic body-centered cubic phase. This transformation can occur locally by focus ion beam (FIB) and allows FIB direct writing of the magnonic structures. Recent research showed that magnetic properties of the resulting structures can be tuned by FIB parameters [4].

The objective of this thesis is to investigate the crystallographic ordering of the FIB - transformed structure according to the FIB parameters and correlate it with their magnetic properties of this structures.

In the Chapter 2, we begin with an introduction to the basic crystallographic terms used in the rest of the theis. In the second section of this chapter, we present the theory behind the experimental diffraction techniques, which are able to probe the crystallographic properties of the materials.

In the Chapter 3, we provide a historical overview with the references to the literature of the metastable iron project. We discuss the growth of the metastable films, their ion irradiation, and already published magnonic applications.

The Chapter 4 summarized the work done during my Erasmus stay at TU Wien. One of the goals was to learn to perform UHV deposition of the metastable films on different substrates. We also carried out a set of experiments in order to investigate the influence of the deposition conditions on the magnetic properties of consequently written structures.

The second contribution of the experimental part consists of the crystallographic (Chapter 5) and magnetic (Chapter 6) experiments performed on the structures fabricated with alternating FIB parameters (structures are described in the Appendix A). We study the influence of these parameters on the crystallographic and magnetic properties. In the Chapter 7, we discuss and correlate these findings together with what can bring new perspectives for the fabrication of future magnonic structures.

2. Crystallography

Crystallography is an experimental science that explores the arrangement of atoms in crystalline solids. In this chapter, we discuss basic crystallographic concepts (Section 2.1) and crystallography techniques (Section 2.2) used in this thesis.

2.1. Basics

With the term crystal, we refer to a solid material whose elements (atoms, ions, molecules) are periodically arranged. This arrangement is often favourable in nature because of it minimizes the energy. The smallest group of particles that repeats in the material is the unit cell. The crystal structure and symmetry have a big impact on many physical properties of matter.

2.1.1. Crystal lattices and systems

We can describe an ideal crystal by a periodically repeated atom or atoms labelled as the basis. The basis positions are determined by a crystal lattice. Translation vectors can be assigned to each point of the crystal lattice. Therefore, any point of the lattice can be described by its position vector as follow [5]:

$$\vec{r} = u\vec{a_1} + v\vec{a_2} + w\vec{a_3}, \tag{2.1}$$

where u, v, w are integers. If the product $\vec{a_1} \cdot (\vec{a_2} \times \vec{a_3})$ corresponds to the minimum volume needed to build the crystal (a primitive cell), vectors $\vec{a_1}$, $\vec{a_2}$, $\vec{a_3}$ are primitive translation vectors of the lattice. By mutual distances (a_1, a_2, a_3) and angles (α, β, γ) between these vectors, we can define so called *Bravais lattices*. Any two Bravais lattices are considered equivalent if they have isomorphic symmetry groups. In this sense, we can identify 14 unique Bravais lattices in three-dimensional space. These are obtained by combining seven lattice systems (triclinic, monoclinic, orthorhombic, tetragonal, rhombohedral, hexagonal, cubic) with centering types (simple, body, face). All the possible 3D Bravais lattices also with the relations between mutual distances and angles are presented in the Figure 2.1. For the purpose of this thesis, the most important Bravais lattices are body-centered cubic (bcc) and face-centered cubic (fcc) [see Figure 2.1 (g)]. These two systems correspond with the possible arrangements of Fe atoms used in this thesis (for more information, see the chapter 3 about metastable iron-nickel thin films).

2.1.2. Miller indices

The experimental part of this thesis is, among others, dedicated to the investigation of the linkage between focus ion beam (FIB) parameters and crystallographic properties of the

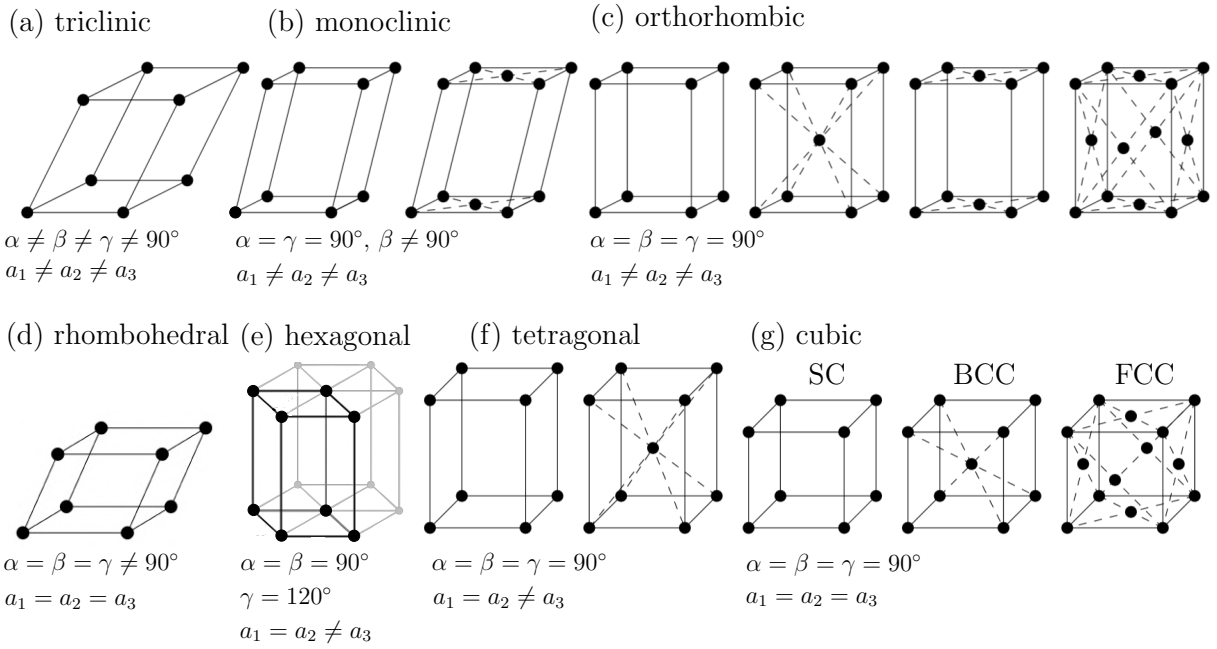

Figure 2.1: 14 Bravais lattices in 3D. Under each system a definition by the relations between distances and angles of the primitive vectors is present. In the (g) subfigure face centered cubic and body centered cubic systems are outlined. Adapted from [6].

transformed structure. Miller indices are an essential tool for this, as they describe the vectors and planes in a crystal lattice by the three-value Miller index notation. A family of equivalent crystallographic planes is determined by three integers h, k and l, which are called the Miller indices.

To define the meaning of the Miller indices, we need to employ primitive reciprocal lattice vectors $\vec{b_1}$, $\vec{b_2}$, $\vec{b_3}$, derivable from primitive vectors using the following formula:

$$\vec{b_1} = 2\pi \frac{\vec{a_2} \times \vec{a_3}}{\vec{a_1} \cdot (\vec{a_2} \times \vec{a_3})}. \tag{2.2}$$

Similarly the terms for $\vec{b_2}$ and $\vec{b_3}$ can be derivated in a similar fashion. Then, the Miller indices determine the family of planes g_{hkl} orthogonal to the reciprocal lattice vector as follows:

$$g_{hkl} = h\vec{b_1} + k\vec{b_2} + l\vec{b_3}. \tag{2.3}$$

Common procedure to determine the Miller indices of the plane in the cubic lattice systems is to use intersections of the plane with x, y, z axes. We mark these intersections as x_0, y_0, z_0. The Miller indices are proportional to these inverses of the intersections $h' = = 1/x_0, k' = 1/y_0, l' = 1/z_0$. The actual Miller indices (h, k, l) are then the smallest coprime integers of h', k', l'. To interpret these indices, we can say that they determine how many times sections intersected by the plane on the crystallographic coordinate axes can be placed in the period of the crystal lattice in the corresponding direction. The Miller index 0 represents the situation when the plane does not intersect the corresponding axis (intersection in ∞; $h' = \frac{1}{\infty} = 0$). Negative indices are indicated with horizontal bars, as in $(h\bar{k}l)$. In the Figure 2.2, several planes are illustrated with the corresponding Miller indices.

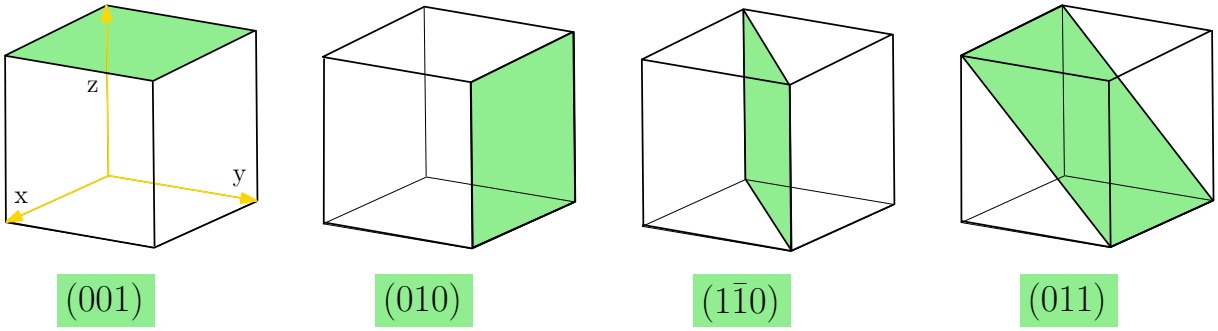

Figure 2.2: An example of the planes with low Miller indices. Coordinate axes are described in the first cube.

With Miller indices, it is possible to mark not only a single specific plane but also the family of equivalent planes and crystallographic directions. To distinguish between these cases, different brackets are used:

- (hkl) – single plane
- $\{hkl\}$ – family of parallel (equivalent) planes
- $[uvw]$ – crystallographic direction
- $\langle uvw \rangle$ – family of parallel (equivalent) directions

As a crystallographic direction, we can consider the vector from the origin of the coordinate system to a point of the crystallographic lattice. This vector is described in the equation (2.1). Miller indices of the direction are the integers $[uvw]$ from this equation.

2.1.3. Crystallographic orientation

In crystallography, one of the most important attribute is the orientation of the crystal unit cell in the space, as it affects other properties of the material. Similar attributes (such as rotation in three-dimensional space) are widely used also in other scientific fields, such as geometry, aerospace, virtual reality or computer graphics [7]. Therefore, various formalisms exist to express the 3D rotation as a mathematical transformation. In general, we can describe 3D rotation by a rotation axis (vector) and the angle of rotation around this axis. However, for plenty of applications, this formalism is not ideal. In these cases, one can use other formalism as quaternions, Euler angles or rotation matrix. Naturally, the conversion between these formalisms is possible. Any rotation may be uniquely described by a minimum of three real parameters. Many formalisms use more than the necessary minimum of three parameters, although each of them still has only three degrees of freedom [8]. In this subsection, we explain several formalisms used in this work.

In the electron back-scatter diffraction (EBSD) measurements (see the subsection 2.2.3), which is a widely used technique in the experimental part of this work, **Euler angles** are the most often used tool to describe the crystal orientation. These angles express the rotations around various coordinate axes required to unify the coordinate systems of the sample and the crystal cell. This unification is presented in the Figure 2.3 (a), where $\left\{e_{\mathrm{i}}^{\mathrm{S}}\right\}$ is the coordinate system of the sample, $\left\{e_{\mathrm{i}}^{\mathrm{C}}\right\}$ is the coordinate system of the crystal and $\left\{e_{\mathrm{i}}^{\mathrm{C}'}\right\}$ is the aligned coordinate system of the crystal after the rotation

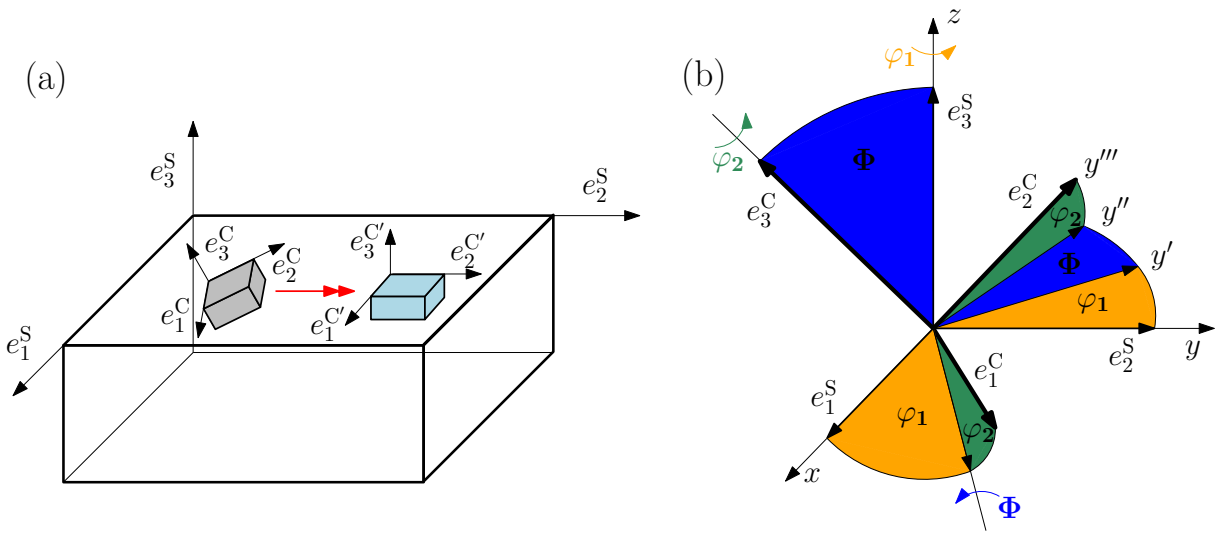

Figure 2.3: (a) A sketch of the geometrical definition of general Euler angles with the coordinate system of the sample $\left\{e_i^S\right\}$ and coordinate systems of the crystal $\left\{e_i^C\right\}$, $\left\{e_i^{C'}\right\}$. The grey prism represents the orientation of the crystal unit cell and the lightblue prism represents the same crystal unit cell unifed with sample coordinate system after the rotation by Euler angles. Adapted from [9]. (b) Euler angles φ_1,Φ,φ_2 by Bunge (zx′z″ convention). Each colour represents one rotation. For y axis, the successive moving is marked (y', y'', y'''). The whole transformation transfer sample coordinate system $\left\{e_i^S\right\}$ to the crystal coordinate system $\left\{e_i^C\right\}$. Adapted from [10].

(the red double arrow represents the transformation). In this notation $\left\{e_i^X\right\}$ indicates three vectors e_1^X, e_2^X, e_3^X which define the coordinate system of X body.

In other words, by Euler angles we spread one rotation around a general axis to three consecutive rotations around characteristic defined axes. Due to the wide spectrum of applications, plenty of notations of Euler angles exist. They vary in the definition of rotation axes. Numerically identical Euler angles in different notations lead to different orientations in the space. Therefore, it is really important to use Euler angles only with specified notation. We can classify two principal types of rotations and Euler angles notations – intrinsic and extrinsic. Intrinsic rotations are elemental rotations that occur around the axes of a coordinate system attached to a moving crystal cell. Therefore, the coordinate axes change their orientation after each elemental rotation. Temporary coordinate axes orientation may be denoted as x′y′z′ (after first rotation), x″y″z″ (after second rotation). Extrinsic rotations are elemental rotations that occur about the axes of the fixed coordinate system [11]. In systems of EBSD, the most used notation is the one introduced by Bunge (Bunge intrinsic notation) [12]. Euler angles in Bunge notation φ_1,Φ,φ_2 are visualised by colour in the Figure 2.3 (b). Furthermore, the successive moving of the rotations axes is nicely visible. Commonly, Euler angles are defined according to the right-hand rule – positive values for clockwise directions. Euler angles are in the following ranges to cover whole space: $\varphi_1, \varphi_2 \in [0, 2\pi]$; $\Phi \in [0, \pi]$. In crystallography, also other notations are sometimes used (e.g. Roe, Kocks). In [13] one can find the relations between these notations. They differ in combination of the rotation axes. However, all notations use the same axis for both the first and third elemental rotations (e.g. zx′z″ for Bunge notations). In the context of Euler angles we can speak about the so-called *Euler*

space. Any orientation expressed by Euler angles can be represented as a point in a 3D coordinate system whose axes are given by the Euler angles [13]. This will be used in the EBSD data visualization in the experimental part of this work.

The most similar formalism to Euler angles is called **Tait-Bryan angles**. These two formalisms are almost the same and are often confused with each other. The only difference is that Tait-Bryan angles use rotations about three distinct axes (e.g. xy′z″). This formalism is widely used for aerospace applications. Therefore, these angles are often called yaw, pitch and roll.

For both of these formalisms, Euler angles and Tait-Bryan angles, some disadvantages exist. One of them, so-called *gimbal lock*, is a well-known problem in many scientific disciplines such, as mechanical engineering. This phenomenon is problematic because we lose one degree of freedom in 3D due to the parallel configuration of two rotation axes. In case of Euler angles it happens for $\Phi = 0$ and $\Phi = \pi$. Hence, only for $\Phi \neq 0$ and $\Phi \neq \pi$ Euler angles determine the rotation in the space unambiguously. Otherwise, if $\Phi = 0$ only the sum of φ_1 and φ_2 is uniquely related to the orientation, so $(\varphi_1, 0, \varphi_2)$ and $(\varphi_1 + \alpha, 0, \varphi_2 - \alpha)$ describe the same orientation (α is arbitrary and addition and substraction of α is modulo 2π). Analogously, if $\Phi = \pi$, the difference between φ_1 and φ_2 is uniquely related to the orientation, so $(\varphi_1, 0, \varphi_2)$ and $(\varphi_1 + \alpha, 0, \varphi_2 + \alpha)$ describe the same orientation [14]. To avoid the gimbal lock, the transformation to the other formalism (e. g. quaternions) is necessary.

In the postprocessing of orientation data yet another complication can emerge. Each orientation can be described by multiple equivalent ways and this can cause the promlematic distinguish between two orientations. For example, in the case of fcc paramagnetic as deposited metastable iron (used in the experimental part of this work) corresponding Euler angles in Bunge notations can be (335°, 90°, 179°) or (65.2°, 90.9°, 0.2°) or (155.2°, 89.8°, 0.9°). This is based on the symmetry of the crystal and in the case of cubic crystals it leads to 24 equivalent combinations of Euler angles for any crystal orientation. The full set of 24 solutions can be obtained by symmetry operations – 2 rotations of 120° about each of the four $\langle 111 \rangle$ directions, 3 rotations of 90° about each of the three $\langle 100 \rangle$ directions and one rotation of 180° about each of the six $\langle 110 \rangle$ directions, plus the identity. This means that Euler space can be subdivided into 24 equivalent subspaces. However, if we perform the rotations around $\langle 111 \rangle$ directions resulting subspaces will have non-trivial shapes. Therefore, in practice, only the rest of the symmetry operations are used and Euler space is divided into 8 subspaces. Following the above considerations, the ranges of Euler angles necessary to build the equivalent subspaces are $\varphi_1 \in [0, 2\pi]$ and φ_2,$\Phi \in [0, \pi/2]$ (equivalent orientations according to rotations around $\langle 111 \rangle$ directions still can be presented in one subspace). Many different names are used to call this subspace, where every orientation is represented only once: fundamental region (the term used in this thesis), asymmetric domain, asymmetric unit, asymmetric region, symmetrically equivalent area, fundamental zone or Mackenzie cell [13]. In the experimental part of this work, we transferred Euler angles to the fundamental region by MTEX software described in the subsection 2.2.4.

In the subsection 2.1.2, we presented **Miller indices** as a tool to describe crystallography planes or directions. Here we add the description how to employ Miller indices as determinants of crystal orientations. The orientation is presented in plane-direction notation as $\{hkl\}\langle uvw \rangle$, where $\{hkl\}$ are the crystal planes perpendicular to the sample normal and $\langle uvw \rangle$ are the crystal directions in the specimen surface aligned with some significant direction expressed in the coordinate system of the crystal [14]. In our case of

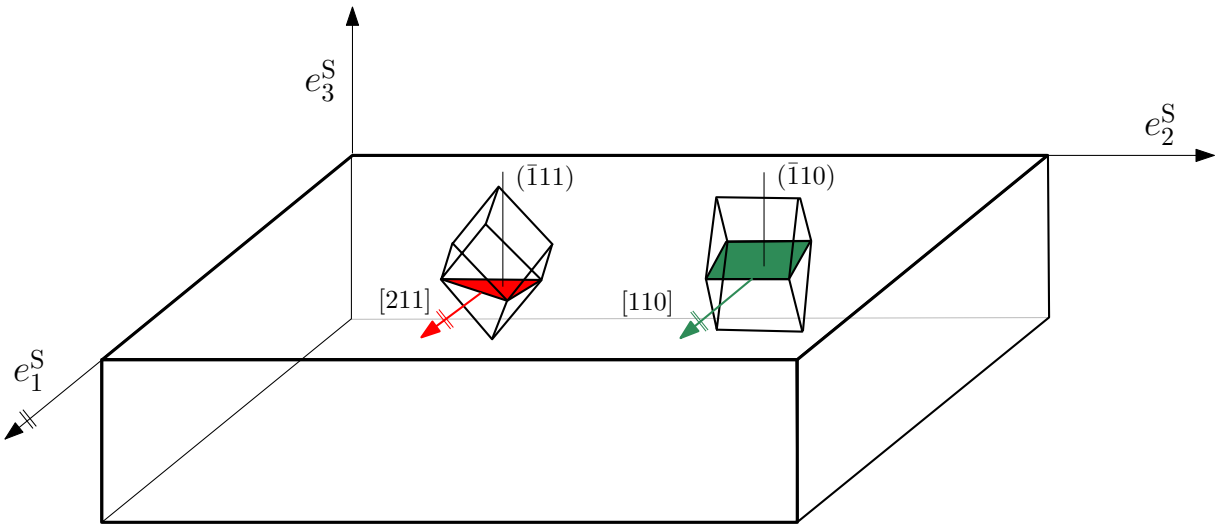

Figure 2.4: Sketch of cubic cells with orientations $\{\bar{1}11\}\langle 211\rangle$ and $\{\bar{1}10\}\langle 110\rangle$ in the Miller notation. Planes and directions used in this notation are marked by green and red colors. Please note, that two perpendicular vectors are representing by two different sets of Miller indices [211] and [110] for two different notations conected with two different planes.

EBSD measurement, this significant direction is one of the coordinate axes of the sample. In other applications, this reference direction can be for example the direction of rolling (in the case of rolled metal sheets). Two examples of crystal orientations notated by Miller indices are presented in the Figure 2.4. Planes perpendicular to the normal vector of the surface are colored by red and green color. Direction vectors parallel to significant coordinate axes e_1^S have also these colors. This formalism has the advantage over the Euler angles that it relates directly back to planes and directions in the crystal, what is also demonstrated in the figure.

Similarly, as in Euler angles formalism also in Miller notation, some orientations given by different sets of indices are physically equivalent because of symmetry. For octahedral crystal symmetry (4 threefold 3 fourfold axes for symmetry rotation), all symmetrically equivalent orientations can be created as follows: values of indices are permuted simultaneously in both $\{\}$ and $\langle\rangle$. If the number of permutations is even, the number of '$^-$' signs added to the original values of indices must be also even. If the number of permutations is odd, the number of added bars must be also odd [14]. As an example, we can state a couple of orientations from the 24 possible equivalent orientations to $\{123\}\langle 63\bar{4}\rangle$: $\left\{21\bar{3}\right\}\langle 364\rangle$, $\left\{\bar{2}1\bar{3}\right\}\langle\bar{3}\bar{6}4\rangle$, $\{312\}\langle\bar{4}63\rangle$. This rule applies to the fcc and bcc crystal systems used in this thesis. In the case of cubic systems, the Miller indices of a given plane are the same as the indices of the direction normal to it. As can been seen in the Figure 2.4, the normal vector of the plane and direction vector are orthogonal, there occurs $hu + kv + lw = 0$. This condition of orthogonality needs to be kept in mind when working with the Miller indices formalism for example in the software for postprocessing of EBSD.

As was already mentioned above, a transformation between different crystallographic orientations formalisms is possible. Here we present the mathematical relationships be-

tween two more used formalism in this work – Euler angles $(\varphi_1, \Phi, \varphi_2)$ and Miller indices $(\{hkl\}\langle uvw\rangle)$ [15]:

$$\cos\Phi = \frac{l}{\sqrt{h^2+k^2+l^2}} \tag{2.4}$$

$$\cos\varphi_2 = \frac{k}{\sqrt{h^2+k^2}} \qquad \sin\varphi_2 = \frac{h}{\sqrt{h^2+k^2}} \tag{2.5}$$

$$\sin\varphi_1 = \frac{w}{\sqrt{u^2+v^2+w^2}}\sqrt{\frac{h^2+k^2+l^2}{h^2+k^2}} \tag{2.6}$$

The last presented orientation formalism is **Pole figure (PF)** and **Inverse pole figure (IPF)**. Unlike the previous ones, these formalisms use graphic expression of crystallographic orientation and therefore, are widely used in orientation mapping tools. Both formalisms are mathematically exactly derived in [14]. Here we present the essence of them to have the necessary notion of their meanings to use them in orientation analysis. Figure 2.5 (b), (c) presents example of a pole figure as a 2D representation of crystal orientation. The orientation of a particular crystallographic plane is completely specified by a single line, passing through the origin and oriented in the direction normal to the plane. This

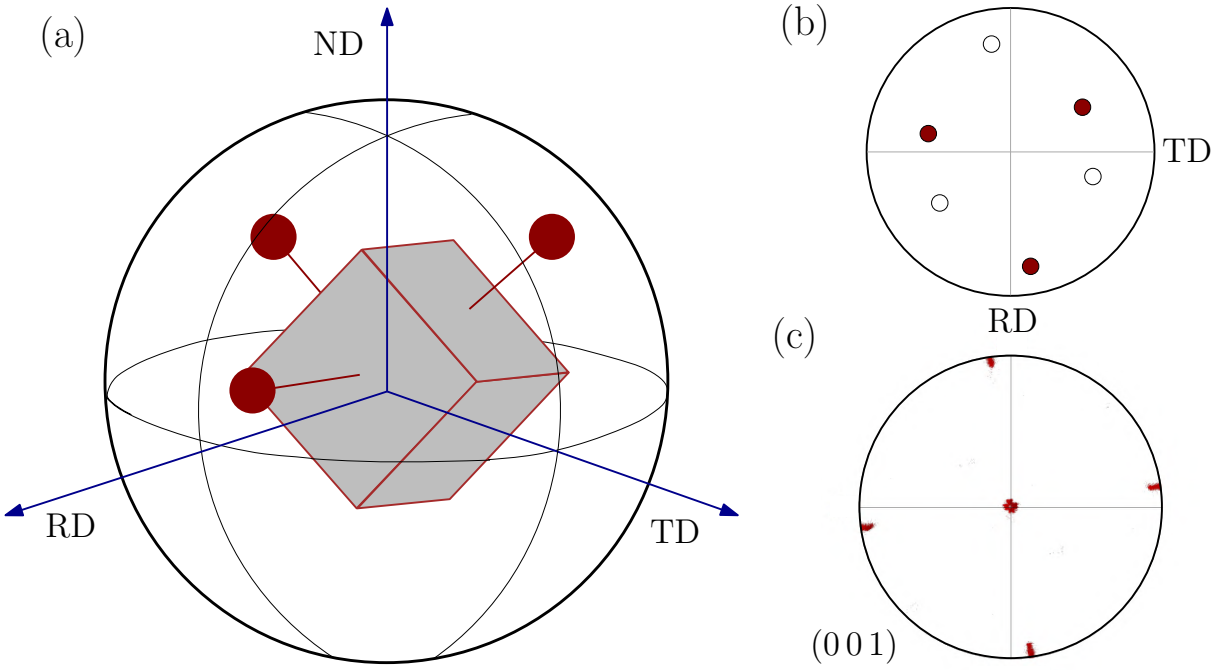

Figure 2.5: Geometrical explanation of the meaning of the pole figure. (a) A grey cube represents the crystal unit cell. Brown points (poles) are the intersections of the normal vector of three cube sides with the unit sphere centered on the origin of the sample coordinate system. In the case of pole figures, directions of coordinate axes are named: normal direction (ND), transverse direction (TD), and rolling direction (RD). (b) When the poles are considered and the hemisphere is stereographically projected into two dimensions, a pole figure is obtained. The clear points correspond to point extending into the bottom half of the sphere and they are symmetrical over the origin with the dark points. (c) Experimentally acquired pole figure from the EBSD measurement of the array of bcc microstructures fabricated by FIB patterning into metastable iron. (a) and (b) was adapted from [15].

line intersects a unit sphere (centered on the origin) in two diametrically opposed points. Since the line passes through the origin, either one of these two points uniquely identifies the line. The orientation of a single crystallographic plane is then completely specified by the point of intersection of the vector normal to the plane with the positive hemisphere of the unit sphere; this point is referred to as the pole [16]. Three poles of three different crystallographic planes are marked by brown color in the Figure 2.5 (a). To fully determine the orientation of an object (cube in our case) it is not enough to employ only a single pole – by rotation around the normal line, we are able to get more orientations with the same pole. The orientation of the object is fully determined by the use of poles of two planes that are not parallel [17]. Finally, the pole figure [Figure 2.5 (b)] is the stereographic projection (projection of the sphere with the intersections to the plane) of the poles [Figure 2.5 (a)] used to represent the orientations of cells from the selected area. In the Figure 2.5 ND, TD, RD are the shortcuts of crystallographic directions: in the context of pole figures with meanings normal, transverse and rolling direction. To determine the arrangement of these directions in the pole figure, one chooses a particular crystal direction and appoints it as normal direction (ND). The intersection of this pole with the sphere is then the center of the pole figure. Such a pole figure is marked as for example {001} *pole figure*, where {001} is the family of planes perpendicular to the pole. In the Figure 2.5 (c), an example of the {001} *pole figure* evaluated from the EBSD measurement of the FIB transformed microstructures in the metastable iron film is shown.

As can be seen in the Figure 2.5 (c), four quadrants of pole figure are equivalent. Therefore, due to this geometrical symmetry, the whole pole figure could be reproduced from any single one of the four quadrants. The same is not true for so-called inverse pole figures (IPF). Whereas a pole figure shows the sample directions aligned with a particular crystallographic pole, an inverse pole figure does the opposite, indicating the crystallographic poles aligned with a specified sample direction (ND, TD or RD). The procedure for constructing an inverse pole figure is quite similar to that of a pole figure, with one exception; instead of projecting a crystallographic pole onto a plane determined

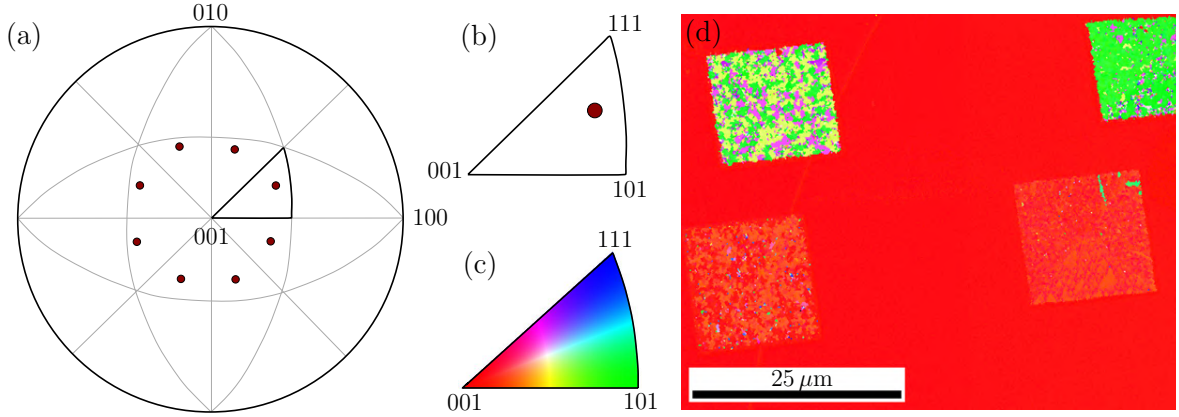

Figure 2.6: Inverse pole figure. (a) Normal-direction full size IPF with all symmetrically equivalent points. It is obtained by the stereographic projection of the unite sphere similarly to PF. Grey lines divided whole image to the 24 stereographic triangles with the standard stereographic triangle outlined. (b) Standard stereographic triangle with only one unique orientation. (c) Standard stereographic triangle with color code for orientation mapping. d) 2D orientation EBSD map measured on the four rectangles prepared with different FIB parameters. (a), (b) and (c) was adapted from [15].

by the sample geometry, the vector pointing along a given sample direction (e. g. normal direction) is projected onto planes determined by the local crystallographic orientation [16]. In an inverse pole figure, the axes of the projection sphere are aligned with crystal directions. As an example a [001] *inverse pole figure* shows which crystal direction in the crystal lattice is aligned with the normal of the sample reference frame.

Figure 2.6 (a) shows an example of normal-direction IPF. As indicated by the grey lines, the cubic crystal symmetry divides the projections into twenty-four stereographic triangles, each containing the identical orientation information [16]. Therefore, the usual presentation of IPF provides only standard stereographic triangle which is marked by bold line in the Figure 2.6 (a). In this work, IPF is used mainly for orientation 2D mapping. For this purpose, we assign different parts of the standard stereographic triangle different contrasting colors. The resulting color code is presented in the Figure 2.6 (c). This code enables to assign a different color to each pixel from an EBSD measurement based on its crystallographic orientation. Such an IPF map is shown in the Figure 2.6 (d).

2.2. Crystallography techniques

In this section, we will present the principles and theoretical concepts of the techniques which can probe the crystallographic properties of our samples. Most of the techniques are based on evaluation of diffraction patterns. Three types of projectiles are typically used. X-ray (XRD) interact with the spatial distribution of electrons, electrons (LEED, EBSD) interact with the total charge distribution and neutrons (elastic neutron scattering) are scattered by the atomic nuclei. Therefore, each projectile has a different pattern and is suitable for different applications.

2.2.1. Low-energy electron diffraction

Low-energy electron diffraction (LEED) is an ultra-high vacuum technique for the determination of the surface structure of crystalline samples. In our project, we use LEED mostly for the characterization of the as grown metastable films and during the in-situ ion transformations.

This technique operates with a collimated beam of electrons with energies between (50 – 500) eV which corresponds to de Broglie wavelengths of (1.7 – 0.5) Å. These wavelengths are comparable with interatomic distances, therefore, crystal lattice must fullfill the diffraction condition. With these energies, the mean free path of the electrons is in the order of few monolayers (ML), hence this technique is surface-sensitive (e. g. LEED can study the surface reconstructions).

In practise, LEED measurements are realised with an electron gun and phosphor screen. From the position of the diffraction spot on the screen, one can determine the crystalline order of the surface. LEED experiments can be described by kinematic theory of diffraction. This means that electron collisions with the crystal can be depicted as single case of elastic scattering. Reciprocal space is conveniently used for the description of the diffraction. The condition of constructive interference can be determined by applying the law of conservation of momentum:

$$(\vec{k_0} - \vec{k'})_{\parallel} = |\vec{G}|, \tag{2.7}$$

where $\vec{k_0}$ is wave vector of incoming electron beam, $\vec{k'}$ is the scattered wave vector and $\vec{G}$ is a vector of the reciprocal lattice. If the scattering is elastic, the magnitudes of both

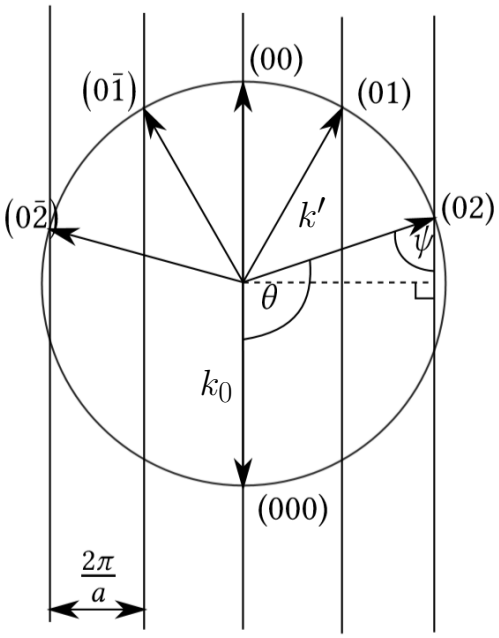

Figure 2.7: Schematic sketch of Ewald sphere in the reciprocal space for the normal incident of the electron beam. $\vec{k_0}$ is the incident wave vector, $\vec{k'}$ is the scattered wave vector, θ is the diffraction angle and ψ is the exit angle to the surface normal. $\frac{2\pi}{a}$ is the primitive vector of the reciprocal space. Taken from [18].

wave vectors are the same, $|\vec{k_0}| = |\vec{k'}|$. This condition is in crystallography called Laue condition.

The Laue condition can be visualized by so called Ewald´s sphere (see Figure 2.7). This sphere has radius $|\vec{k_0}|$ and origin at the center of the incident wave vector. Laue condition is satisfied for a vector $\vec{k'}$ (direction of the reflected beam) beginning in the origin and terminating at an intersection between the sphere and rods pointing perpendicular from each point of the reciprocal lattice. These intersections are marked as (hk) in the figure. The points of these intersections will occour as bright spots on the fluorescent LEED screen.

2.2.2. X-ray diffraction

X-ray diffraction (XRD) or alternatively X-ray crystallography (XRC) is a technique which employs X-rays to diffract in a crystal. Each crystal structure has specific diffraction pattern (directions of constructive interference). In our case, we used this technique as a comparative measurement of the transformed area in metastable films to electron backscatter diffraction (EBSD).

In practice, these measurements are realised with the X-ray source and rotatable detector. The X-ray tube is used as a source of X-rays, which are generated by heating a filament to produce electron, which bombards a target. When electrons have sufficient energy to dislodge inner shell electrons of the target material, characteristic X-ray spectra are produced. The samples is irradiated with a characteristic X-ray beam of fixed wavelength and the angle of the detector is varied gradually. The output of these measurements is the dependence between the detector angle and the beam intensity for the

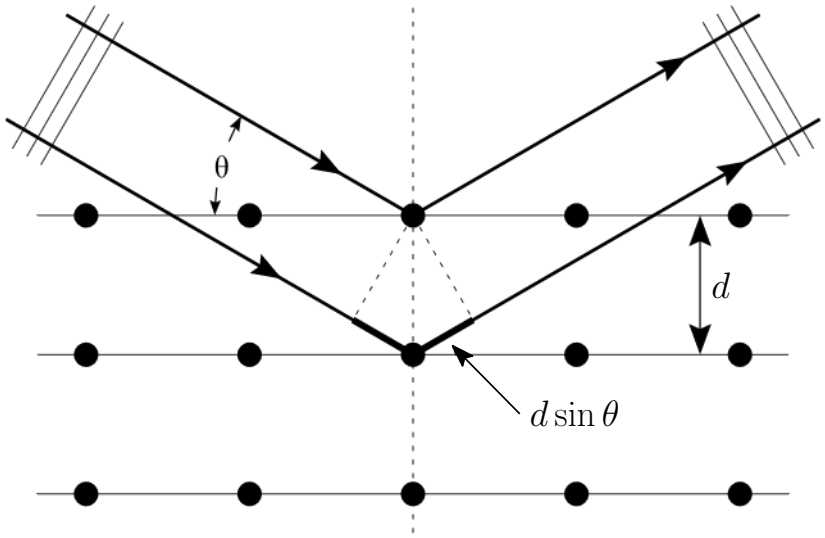

Figure 2.8: The sketch of X-ray reflection on the crystal plane. Condition of constructive interference is given by Bragg law (equation 2.8). Taken from [19].

corresponding geometry. The position of the peaks (i. e. fulfiled condition of constructive interference) is determined by the Braggs law:

$$2d \sin \theta = n\lambda, \tag{2.8}$$

where d is the spacing between two diffraction planes, θ the incidence angle and n is an integer number. This geometry is shown in the Figure 2.8. From the positions and the intensities of the peaks, it is possible to determine the crystal structure and Miller indices of the reflections planes.

2.2.3. Electron backscatter diffraction

Electron backscatter diffraction (EBSD) is characterization technique in electron microscopy and is commonly used in the studies of crystalline and polycrystalline materials. It uses backscattered electrons (BSE) to provide information about the individual crystal grain orientations, local texture, point-to-point orientation correlations, phase identification and distributions [16]. We employ this technique to analyze the crystallographic orientation of the transformed microstructures and its dependence on the focus ion beam parameters. The follow-up intention was to find and understand the linkage between crystallographic and magnetic properties of the investigated structures.

Historically, this technique started to evolve in 1928 when Nishikawa and Kikuchi observed for the first time a diffraction pattern in backscattered electrons in calcite [20]. With the same volume, they observed diffraction pattern also in the transmission mode. Therefore, these patterns are called *Kikuchi patterns*. In the beginning, EBSD was an alternative to X-ray diffraction measurement. With the development in the field of electron microscopy, such as high spatial resolution, high scanning speed, or automated pattern recognition, the new possibilities, such as orientation mapping of large areas became available. Nowadays, the EBSD is a technique with both scientific and industrial applications.

In practice, these measurements are typically realised in the conventional scanning electron microscope with the sample at a high tilt angle (approx. 70 ° from the horizontal direction) towards the diffraction camera. This sharp angle towards the primary beam is

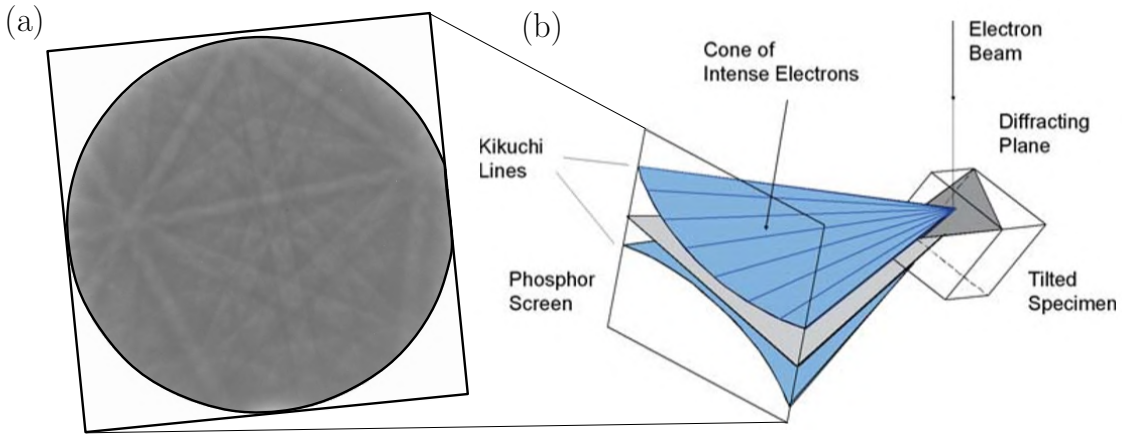

Figure 2.9: EBSD Kikuchi pattern. (a) Kikuchi pattern of the fcc iron-nickel thin film from our typical measurement. (b) Sketch of diffraction cones in the geometry with the electron beam, diffraction plane and phosphor screen. Taken from [16].

necessary for securing high enough contrast of the diffraction pattern (phosphor screens have a threshold number of incident electrons for successful electron – photon conversion). This is achieved thanks to a shorter escape path for diffracted electrons with tilted sample (shorter escape path also avoids the inelastic scattering). Diffraction patterns [see Figure 2.9 (a)] from the detection screen are acquired on a CCD camera and sent to the computer for subsequent analysis. The CCD camera together with the detection screen form the retractable *EBSD detector*. To get the best signal-to-noise ratio, the final angle and distance optimization of each system is needed. The origin of the noise is in the diffracted BSE with additional inelastic collisions and from tbe BSE without diffraction. A sketch of the experimental geometry with the primary beam, a specimen and the phosphor screen is shown in the Figure 2.9 (b).

EBSD yields all the information by the evaluation of the Kikuchi patterns [one example is shown in the Figure 2.9 (a)] that are the centrepiece of the technique. The characteristic feature of the Kikuchi pattern is the regular arrangement of bright bands (not a regular array of diffraction spots as in LEED or XRD). This arrangement can be interpreted as a gnomonic projection (projection from the sphere to the plane touching the sphere in the pole) of the crystal lattice on the flat screen with the centre of the projection in the point where the primary beam interacts with the sample. Diffracted BSE must exit the sample near the Bragg angle (to fulfil the diffraction condition) and form the Kikuchi band. Figure 2.9 (b) is showing a given unit cell orientation with a specified diffraction plane. The edges of the diffraction band are formed by two diffraction cones from the Figure 2.9. The centre of the band is the projection of the plane through the centre of the diffraction cone on the screen [16]. This simple geometric idea together with kinematic approximation (single elastic scattering) can not fully explain the intensity distribution of the pattern. To fully quantify the intensity distribution, the dynamical theory of electron diffraction must be employed [21].

At the beginning of this section, we have allready indicated several material properties which can be extracted from the EBSD diffraction pattern. In the following list, we describe the linkage between the pattern features and the crystallographic properties. The inspiration for the outline of this list was found in [9].

- **Angles between diffraction bands**
  - When we consider correction from the gnomonic projections, the angles between diffraction bands match with the angles between corresponding crystallographic planes [22]. In the Figure 2.10 is marked the example of such angle as α.
- **Width of the diffraction band**
  - The (angular) width of the band $\{hkl\}$ is twice the Bragg angle ϑ_{hkl}. Thus, we can calculate the interplanar spacing d_{hkl} from the Bragg's law: $2 \cdot d_{hkl} \cdot \sin \vartheta_{hkl} = = n \cdot \lambda$, where d_{hkl} is a interplanar spacing, n is the order of reflection, λ is the wavelength of the incident electron beam and $\{hkl\}$ are Miller indices of the plane (and also Kikuchi band) [16]. In the Figure 2.10 is marked the example of such width as $2\,\vartheta_{hkl}$.
- **Brightness gradient at the boundary of diffraction bands**
  - Elastic strain of the crystal lattice is in connection with the brightness gradient in the edge of the band [23].
- **Intersections of diffraction bands**
  - From the mutual positions of the bands in the pattern it is also possible to determine the symmetry of the crystal (crystallography point and space symmetry group) [24]. Changes in the distance between intersections are proportional to the elastic stress in the lattice and to the lattice distortion. In the Figure 2.10 orange points mark the intersections of the most significant bands which can be used for such analysis.
- **Total contrast of the diffraction bands to the background**
  - The contrast of the pattern corresponds with dislocation density in the sample, what can be detected with image quality (IQ) parameter of the pattern. It can be used for example for the determination of the recrystallized fractions in metals [25].
- **Higher order diffraction bands**
  - These parallel bands originate from diffraction from the planes with higher Miller indices. With more dislocations and deformation of the material, these higher order bands disappear [26]. In the Figure 2.10 green lines mark the example of higher order diffraction bands.

It was already shown that the geometry of a Kikuchi pattern is unique for a particular crystal structure and lattice orientation. Hence, from positions and widths of some bands in the pattern, it is possible to index the crystallographic structure and extract other information about the volume where the pattern was collected. Nowadays, computers are widely employed to recognize and evaluate Kikuchi patterns. However, it is not so straightforward. Unlike the computer, the human eye can easily perceive lines, curves, and other regular motifs in diffuse or noisy images [16]. To get a fully automated EBSD system, it is necessary to process the patterns as follows: In the first step, the background

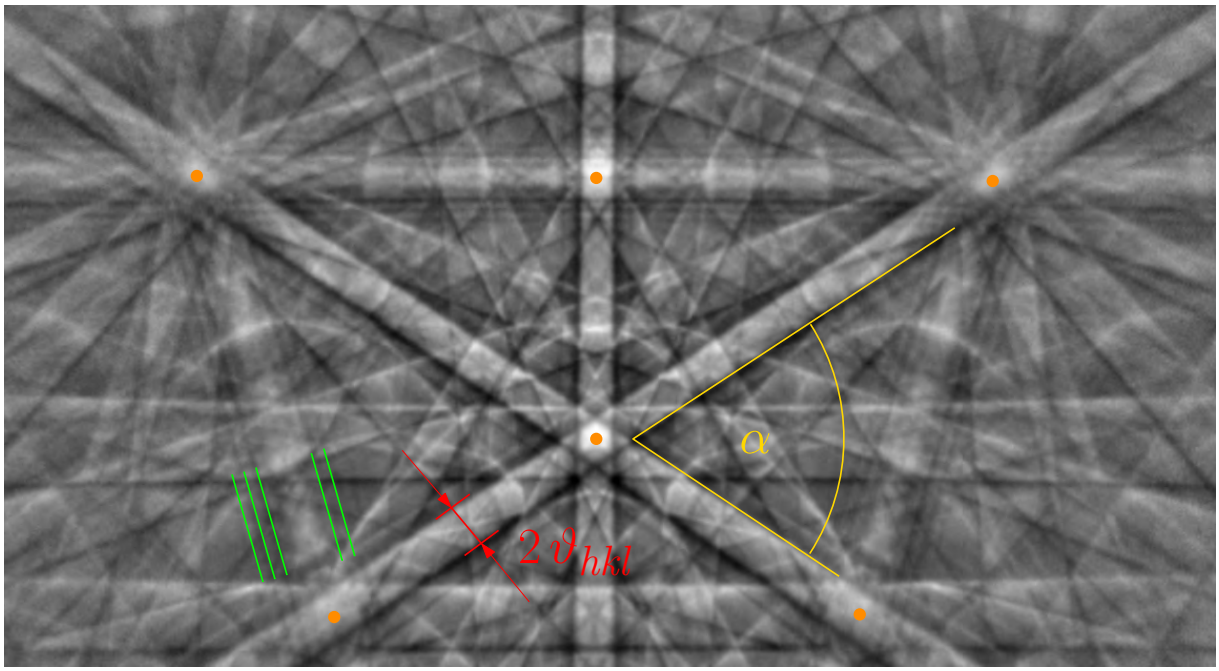

Figure 2.10: Diffraction pattern collected from silicon at 20kV accelerating voltage. Adapted from [27]. In the pattern are highlighted some important features which are more commented in the text.

is subtracted and also contrast and brightness of the image are optimized by modification of the brightness histogram. In the second step, the detection of diffraction bands by modified Hough transformation (a special case of Radon transformation) takes place [29]. This transformation is commonly used in the image processing to find linear features in the image. The essence of Hough transformation is conversion of a line to the parameter space. Commonly, the line is expressed parametrically by the following formula: $y = = mx + b$. However, this expression is highly impractical for image processing because the vertical lines slope parameter m is ∞. Therefore, the Hough transformation uses so called Hesse normal parametric form: $\varrho = x \sin\theta + y \cos\theta$, where ϱ is the smallest distance from the origin and θ is the angle between the line and x axis [see the Figure 2.11 (a)]. Each band from the pattern can be represented as a point in the Hough space [see the Figure 2.11 (b)]. The intensity of all points from the Kikuchi band is accumulated and

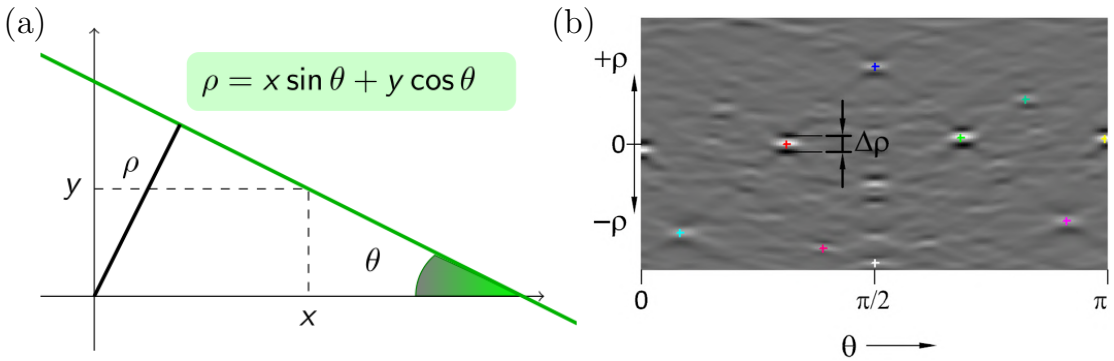

Figure 2.11: Hough transformation. (a) Line in Cartesian space (x, y) define by ϱ and θ. Taken from [28]. (b) Kikuchi pattern transformed to the Hough space (ϱ, θ). Each color cross corresponds with one band from the pattern.

corresponds to the intensity of the point in the Hough space [16]. Therefore, the task is not to find the line in the space but to find the most intensive points, which is easier for the software.

The next step is the indexing of the Hough transformed Kikuchi pattern. It is based on the comparison of measured interplanar angles (which correspond to the angles between Kikuchi bands) and interplanar spacing (which are represented by the width of the bands) with theoretical values from the library of the crystal structures [16]. Consideration of the first 3 to 4 bands is usually enough to recognize the $\{hkl\}$ plane family of the crystal. Practically, the judgment of the crystal structure is realised by the so called *Vote scheme* [30]. From the recognized bands, all possible combinations of triple bands are assembled and the angles between them are compared with the angles from the table with the possible orientation of the selected phase. If the angular deviation is smaller than the tolerance (e. g. 5° [30]) the orientation gets a vote. The orientation with the most votes is the most probable one. From this indexing, we can get an important parameter called the *confidence index (CI)*, which refers to the reliability of the result. It can be defined for example in a following way [30]:

$$\mathrm{CI} = \frac{V_1 - V_2}{V_{\mathrm{ideal}}}, \tag{2.9}$$

where V_1 and V_2 are numbers of votes for the first and the second most probable orientation and V_{ideal} is the total number of possible votes. CI possesses the values between 0 and 1. By a comparison of automatically and manually indexed fcc pattern, it was derived that solutions with $\mathrm{CI} > 0.1$ are indexed with 95 % success rate [30]. CI plays the key role in the EBSD data postprocessing (see the Section 5.2).

2.2.4. Sofwares for postprocessing of the EBSD data

The raw EBSD data can be displayed and processed to provide a wide variety of information about the sample microstructure in several softwares. Here, we briefly introduce two software packeges used in the experimental part of this work – OIM Analysis™ and MTEX Toolbox.

OIM Analysis is a commercially available technique based on the automated collection and analysis of EBSD patterns. This mapping data provides information on the crystallographic orientation, phase distribution, grain size and shape, grain boundary structure, and local deformation of crystallographic microstructures [31]. In our case, the most often used tools are: data clean-up based on the values of CI, 2D fcc/bcc phase map, 2D IPF orientation map, cropping parts of the data, crystallographic orientation charts, etc.

MTEX is a free objective oriented Matlab toolbox for analyzing and modeling crystallographic textures employing EBSD or pole figure data [32]. The software has a rich online tutorial and documentation. For our purpose we use mainly the operations in the Euler space (such as transformation to the fundamental region) and comparison of the orientation data from the different areas of the sample.

3. Metastable iron-nickel thin films

The story of the metastable iron project began around the year 2000 at TU Wien in the Surface physics research group of prof. Peter Varga (first article about metastable iron was published by the group from the University of Witwatersrand Johannesburg in 1967 [33]). In the year 2001 A. Biederman et al. published their study about the crystallographic structure of ultrathin Fe films grown on Cu(100) [34]. Then the investigation of the behavior of the ultrathin iron films continued. In the year 2008 W. Rupp et al. published the article about Ion-beam induced fcc-bcc transition in ultrathin (1.5 nm) iron films epitaxially grown on Cu(100) crystal and its possible perspectives in applications to ultrahigh density magnetic recording and other nanoscale magnetic systems [35]. In the following years, investigation of this system was ongoing in such directions as the growth of thicker metastable films and using substrates with more suitable properties.In the year 2012, the project was extended about the collaboration of prof. Varga with M. Urbánek from the Brno University of Technology. First idea was to jointly explore the possibilities of applications to the magnetic recording. However, after time research focus was shifted to the direct-writing of the microstructures by FIB and its utilization in magnonics. Unfortunately, on 27. 10. 2018, the project initiator prof. Varga passed away. However, the cooperation on the project still continues thanks to the formidable relationship of our group with prof. Ulrike Diebold and prof. Michael Schmid from TU Wien. The goal of this chapter is to present the relevant references, main findings and state of art of different part of the project: Basics and motivations of the project (Section 3.1), Growth of metastable iron-nickel thin films (Section 3.2), FIB direct writing of the magnonics structures (Section 3.3) and Magnonics applications (Section 3.4).

3.1. Basics and motivations of the project

The crystallographic structure of iron in bulk material at room temperature is body centered cubic (α-Fe) with ferromagnetic behaviour. Another alothropic configuration of iron has a face centered cubic crystallographic arrangement and exhibits paramagnetic behaviour (γ-Fe). The Curie temperature of iron (the temperature above which material looses its permanent magnetic properties) is approx. 770 °C and for even higher temperature of 900 °C the iron recrystallizes to the fcc γ-Fe phase. It was found that this high-temperature γ-Fe phase can be stabilized also at the room temperature by epitaxial deposition of the thin film onto the suitable substrate with small lattice mismatch to the fcc phase of iron [35]. At the room temperature, the fcc Fe lattice has a lattice constant of 3.588 Å, and the bcc Fe has a lattice constant of 2.680 Å. The copper has an fcc lattice with a lattice constant of 3.615 Å. This makes the fcc Fe structure more suitable to epitaxially grow on copper substrates. By the same precondition (i. e. low lattice mismatch) also other substrates able to stabilize fcc Fe can be selected and tested. More information

about the tested substrates and stabilization of the fcc metastable phase can be found in the Section 3.2.

The most promising application of the metastable iron is the single-step manufacturing of the magnetic micro and nanostructures in the nonmagnetic surroundings by ion induced fcc to bcc transformation. The ion beam induces a structural and magnetic phase change by overcoming the potential barrier between the fcc local minimum and the bcc global minimum and therefore we call these fcc films metastable. The transformation can be done in-situ in the growth chamber by a broad ion beam irradiation [3]. Basic patterning is possible using a mask [36] or ex-situ in dual beam FIB/SEM system [4]. For the magnonics structures (waveguides, magnononics crystals,...) the most suitable tool for fabrication is FIB. This is due to by FIB parameters is possible to tune the magnetic and crystallographic properties of the material [4]. The FIB preparation of the magnonic structures is elaborated in more focus in the Section 3.3.

3.2. Growth of metastable iron-nickel thin films

Thickness of the deposited iron has strong influence on the growth regime [37]. Three iron growth regimes on Cu(100) were observed: below 4 ML iron grows with bcc-like structure with out-of-plane magnetic anisotropy; between 5 and 10 ML iron grows following the fcc (100) substrate and exhibits paramagnetic behaviour; above 10 ML (critical thickness) iron relaxes to the stable ferromagnetic bcc phase. The growth regimes are summarized in the Figure 3.1. The critical thickness of 10 ML is highly limiting for upcoming applications and therefore the stabilization of the fcc iron phase in the thicker films was one of the most important goals of this part of the project.

Fortunately, two approaches that are able to push the critical thickness were developed. Firstly, a stabilizing effect of CO was found and allowed to push the 10 ML thickness limitation to approx. 22 ML (∼4 nm) [38]. The principle of this stabilization is as follows: CO is dissociated at the surface and carbon gets buried in the growing film while the

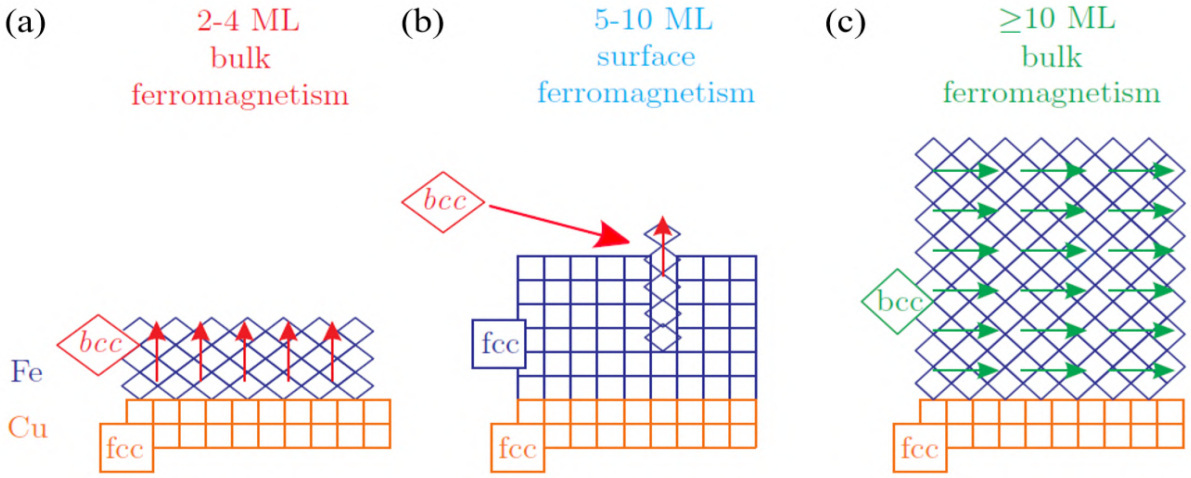

Figure 3.1: Fe growth regime on Cu(100). (a) Below 4 ML, Fe has bcc structure with out-of-plane magnetization. (b) Above 4 ML and below the critical thickness of 10 ML, the films are epitaxial, paramagnetic and fcc. (c) Above 10 ML, the films spontaneously transform into relaxed bcc stable ferromagnetic phase. Taken from [18].

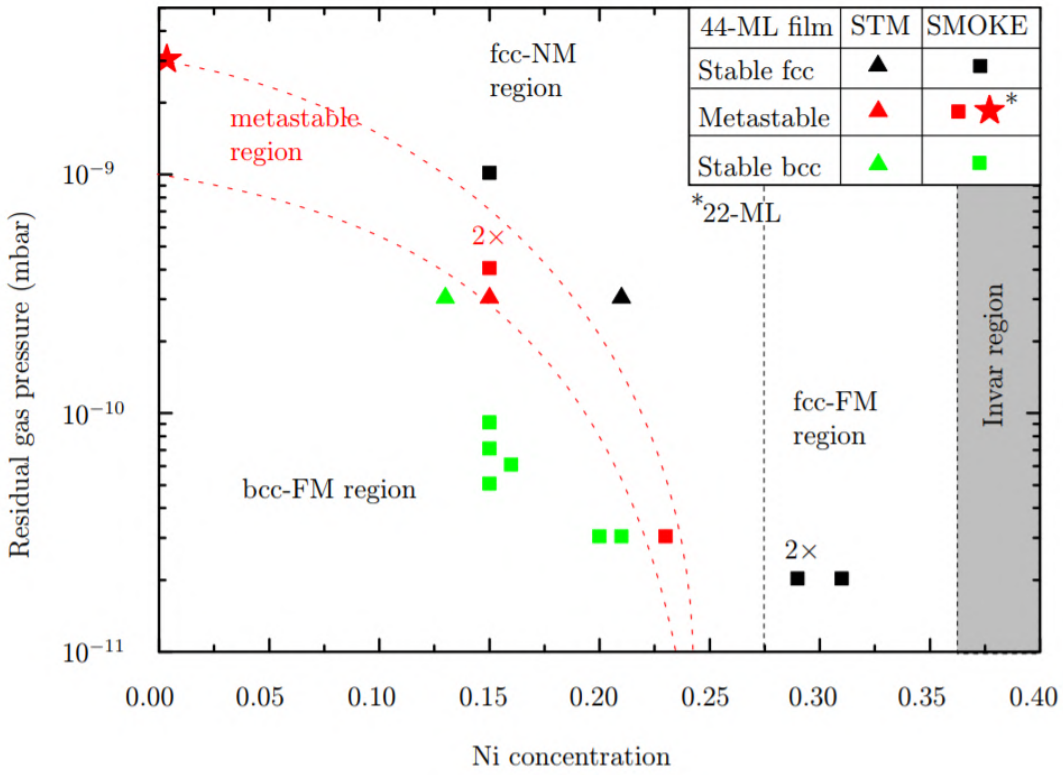

Figure 3.2: Experimentally determined phase diagram of the dependence of the structural and magnetic phases of $Fe_{1-x}Ni_x$ films on Ni concentration and on the residual gas pressure during the deposition. The depositions were done on Cu(100) substrate and thicknesses of the films were 44 ML (∼8 nm). The data are combined from the experiments done in two UHV setups (STM, SMOKE). Different color refers to a different phase and different shapes to different UHV setup. The CO stabilized 22-ML thick pure iron film from [38] is marked by an asterisk. At Ni concentrations above 28 % the films are fcc ferromagnetic (black dotted line divides the fcc region to nonmagnetic and ferromagnetic). Taken from [3].

oxygen floats on the surface and helps to realize layer-by-layer growth. Details can be found in [38] and [3]. However, there is still a thickness limitation due to the surface saturation by oxygen. Later it was also found that when the iron is alloyed with approx. 20 % of nickel (room temperature crystallographic structure of nickel is fcc), the layers can keep the fcc structure with no thickness limitation; nevertheless the layers can be still transformed by an ion beam to the stable bcc phase [3]. All stabilization experiments were summarized by Gloss in [3]. Deposition experiments with different CO pressures and different Fe/Ni ratio were concluded in the experimentally determined phase diagram (see the Figure 3.2). The phases from the diagram (stable fcc, stable bcc, and metastable fcc) were distinguished by the Surface Magneto-Optical Kerr effect (SMOKE) and in-situ irradiation by broad low-energy Ar^+ ion beam. Based on these experiments, for the future usage the concentration of the Ni was fixed on 22 %.

Most research on metastable Fe or Fe-Ni films in the past was done on copper crystals. Also in this work, most of the experiments were done with films on Cu(100) as it exhibits the most suitable substrate yet found. Nevertheless, also other substrates were investigated. One of them was diamond (lattice mismatch 0.1 % with γ-Fe) – an attractive material for both scientific and industrial applications. For us a very inter-

esting and important property of diamond is its transparency to the visible light and the lack of electrical conductivity, which might open some interesting applications in magnonics. With the transparent and nonconductive substrate, magnons can be excited via parametric pumping [39]. Gloss showed in his dissertation thesis [18] that the deposition of metastable fcc $Fe_{78}Ni_{22}$ films on diamond substrates is possible. Unfortunately, the growth regime (in the CO atmosphere and with the sample temperature elevated to 450 °C) takes place in the island growth mode (Volmer-Weber) which is highly unfavorable when compared to uniform layer by layer growth observed on Cu. These films can be transformed by ion irradiation to the bcc phase, but the resulting layer has different magnetic properties than $Fe_{78}Ni_{22}$/Cu(100). Discontinuous layers are not very interesting for magnonics/spintronics as they are not conductive and would cause huge losses in the spin-wave propagation due to spin-wave scattering and total lack of exchange interaction between the islands.

The second investigated substrate was silicon – an interesting substrate for industry applications for its low cost and well-known properties. It was shown by Gloss et all. that it is possible to grow metastable, epitaxial fcc $Fe_{78}Ni_{22}$ on H-Si(100) with a Cu(100) buffer layer, and than by using a focused ion beam create magnetic micro- and nanostructures with tuneable saturation magnetization by modifiing the ion dose [40]. Iron-nickel films do not grow epitaxially directly on Si(100) yet it is possible to grow Cu(100) buffer layer on the silicon substrate and the follow-up growth of metastable iron-nickel films is possible [41]. The preferred crystallographic orientation of copper on silicon is (111). To achieve the desired (100) crystallography orientation it is necessary to have the Si(100) surface unreconstructed and hydrogen-terminated. This can be done in two possible ways - chemically, by etching the Si in 10 % HF or in-situ, by annealing at 1200 °C followed by adsorption of atomic hydrogen. In recent years the equivalence of these two techniques for growth of $Fe_{78}Ni_{22}$/Cu(100)/H-Si(100) was proven [40]. During the growth of the Cu(100) buffer layer, silicides are formed on Si-Cu interference. These silicides induce strain into the film and thus support its island growth mode. It was also shown that the surface morphology improves with increasing thickness of the film [42]. Furthermore, it was shown that it is not possible to grow Cu(100) with pure copper on an in-situ prepared crystal. However, the depositions were successful with a small amount of Ca contamination [18]. This is not still well understood but it seems that copper needs some impurities as a surfactant for the growth of (100)-oriented Cu films.

The more recent state of art about the growth of metastable iron on different substrates is summarized in the dissertation thesis of Jonáš Gloss [18].

3.3. Ion transformation of the metastable iron-nickel layers and FIB direct writing of the magnonics structures

Magnetic nanopatterning plays a central role in the development of novel devices and magnetic metamaterials with properties unachievable in bulk systems. The patterning is conventionally achieved by using optical or electron-beam lithography in combination with lift-off and etching procedures. Direct writing of magnetic patterns by focused ion- or electron-beam irradiation is a single-step process, which is an advantage over traditional multi-step lithography techniques thanks to the simplicity and straightforwardness of the

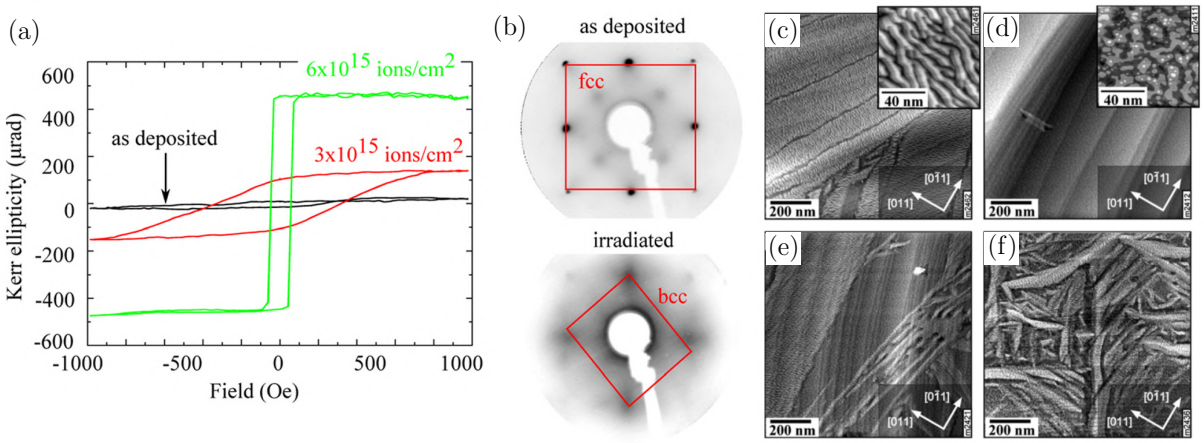

Figure 3.3: Ion transformation of the metastable iron-nickel films. (a) Hysteresis loops measured by SMOKE on a $Fe_{77}Ni_{23}$ layer deposited at a base pressure 3×10^{-11}mbar. Hysteresis loops for as-deposited film (black), partially transformed film (red) and fully transformed film (green) are present. (b) LEED patterns of the as-deposited (fcc lattice with c(2×2) O superstructure) and fully transformed film (bcc(110) lattice). (c), (d) STM images of as-deposited films with different Ni concentration (c – 13%, d – 15%). $Fe_{85}Ni_{15}$ film was then irradiated by 2 keV Ar^+ ions with a dose of (e) 2×10^{14}cm^{-2} and (f) 3×10^{15}cm^{-2}. Areas transformed to bcc appear brighter (higher) in the STM images. In (c) is spontaneously transformed film. Taken from [3].

method. Therefore, a big interest in our project is focused on the ion irradiation of the films.

Several findings about the ion irradiation of the metastable iron-based films were done. Rupp et al. irradiated 1.5 nm thick iron film on Cu(100) substrate by low-energetic Ar^+ ions and observed the change of magnetic behavior from paramagnetic to ferromagnetic (measured in-situ by SMOKE). That was accompanied by in-situ scanning tunneling microscopy (STM) measurement which showed the evolution of the crystallography during the irradiation from the as grown fcc(100) film to fully transformed bcc(110). The transformation took place in the form of small bcc needles [35]. Similar work has been later published by Shah Zaman et al. in the system of 4 nm Fe stabilized by dosing CO [38]. In the Figure 3.3 is presented more recent irradiation experiment done by Gloss on the film on Cu(100) stabilzed by both Ni and CO [3]. In the Figure 3.3(f) is STM picture of fully transformed film with bcc needles oriented preferentially in [0$\bar{1}$1] directions.

In [4] Urbánek et al. reported the controlling of the structural and magnetic properties by varying the FIB parameters (Ga^+ ions were used). This work proved to be very important as it opened new possibilities for direct writing of magnetic patterns. Experiments were done in $Fe_{78}Ni_{22}$ film deposited on Cu(100) substrate in the CO atmosphere. Two different regimes of transformation were observed depending on the scanning approach: (1) by performing 100 fast scans over the full irradiated area and (2) by applying the full ion dose in one (slower) scan. By the first 100 scans approach transformation process is stochastic and result in small bcc nuclei which grow with increasing ion dose. In the case of a single scan, it was observed so-called critical ion dose. With this dose, the bcc needles start to expanding in a triangular fashion from the point of initiation. The ion dose needed to sustain the growth once it was initiated is significantly lower than in the case of nucleation of the bcc nuclei from the pure fcc material. Even more important

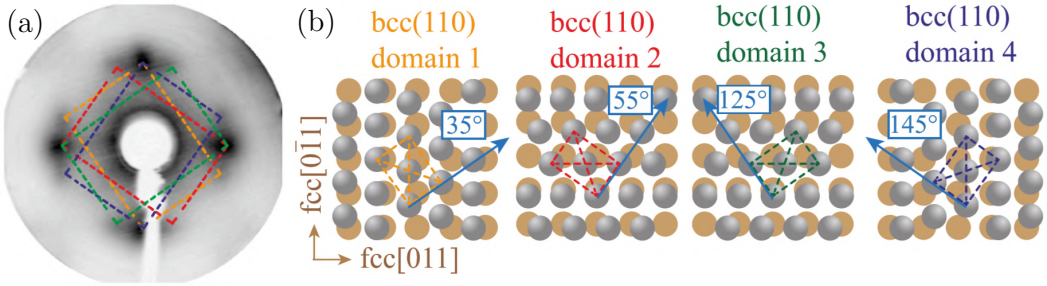

Figure 3.4: (a) LEED pattern showing four bcc (110) domains after the in-situ transformation by a broad ion beam. (b) Schematic of four bcc domains with arrows indicating directions of the easy axes. Adapted from [4].

finding is the possibility to control the magnetic anisotropy of the transformed patterns by changing the FIB scanning directions (concluded from the hysteresis loops measured by a home-made magnetometer) [43]. To explain the behavior of the evolution of the magnetic uniaxial anisotropy with respect to the direction of the FIB scanning a crystallography model was employed. The LEED pattern [see the Figure 3.4 (a)] of the in-situ transformed film by Ar^+ ions shows four possible bcc (110) domains. The Figure 3.4 (b) shows these possible bcc domains with blue arrows indicating the angles of the easy axis, which is presented as an explanation of the observed anisotropy evolution.

Other interesting knowledge about the FIB direct writing was summarized in the dissertation thesis of L. Flajšman, which focuses on the applicability of the material to the field of magnonics [43]. It was shown, that long and narrow waveguides for spin wave propagation can be grown by creating an overdosed initiation region.

To get better insight into the ion transformation process, Gloss [18] and Flajšman [43] performed calculations of the interaction of the ions with the sample using the SRIM (Stopping and Range of Ions in Matter) package. Both calculations were done for 8 nm FeNi/Cu system. Gloss calculated the irradiation by 2 keV and 4 keV Ar^+ as well as 30 keV Ga^+. Flajšman extended the calculations for Ga^+ ions in the energy range from 5 keV to 50 keV. From these calculations, it follows that for 2 keV the ions stop in the topmost layers of the iron-nickel film, where they also deposit most of their energy. For 4 keV a small fraction of the ions are able to penetrate through the whole iron-nickel film and stop in the top layers of Cu. For 30 keV, the ions penetrate deep into the copper. Intermixing of copper with iron starts at approx. 6 keV for Ar^+ and at 10 keV for Ga^+. For the maximum ion beam energy given by the Ga^+ ion beam source of the Tescan Lyra 3 microscope (30 keV) the mean projected ion range is close to 10 nm. For ion energy of 5 keV, the mean range drops to 3 nm. The calculation also shows that for 30 keV majority of the ions ends up in the substrate, whereas for 5 keV all the ions will be implanted into the iron-nickel layer.

3.4. Magnonic applications

Some magnonic experiments in the system of metastable iron were already done. In [4] fabrication of two types of magnonic crystals is reported. It wasachived by alternating the ion dose (affecting the magnetization) or by alternating scanning direction (affecting the direction of magnetic anisotropy).

In the recent work of Flajšman et al., a zero-field propagation of spin waves in waveguides prepared by FIB in the metastable iron-nickel film was reported [44]. The magnetocrystalline anisotropy in waveguides is strong enough to stabilize the magnetization in the direction perpendicular to the long axis of narrow waveguides. Therefore, it is possible to propagate spin waves in these waveguides in the favorable Damon-Eshbach geometry (propagation of the spin wave is perpendicular to the static magnetization direction) without the presence of any external magnetic field. Phase-resolved microfocused Brillouin light scattering (BLS) was employed to measure the spin-wave dispersion in the system.

So far the last experiments in the field of magnonics on the system are presented in the publication by Wojewoda et all. He reports on the propagation of spin waves through a Néel domain wall [45]. This Néel domain wall was stabilized in the FIB prepared waveguides in metastable iron. The spin waves were excited by the microwave antenna. Two regimes (dependent on excitation frequency) of spin wave propagation were observed by the BLS measured intensity 2D map. In the first regime (7.15 GHz) two spin wave beams are created in the vicinity of the domain wall. On the contrary, in the second regime (9 GHz) the spin waves propagate through the domain wall and create a single spin-wave beam.

4. Growth of metastable films

Experiments from this chapter were done during my Erasmus stay in TU Wien in the Surface physics group of prof. Diebold. My work was supervised by prof. Schmid and Dr. Gloss. In the Sections 4.1 and 4.2, depositions on diamond and silicon substrates are presented. In the case of diamond substrate, we tried to use the substrate with large terraces and in the case of silicon substrate, we deposited a thicker Cu buffer layer than in previous experiments (extensions of previously done experiments). In the subsection 4.3 the set of experiments with the varying CO pressure during the deposition was presented. For the current knowledge about the depositions on the silicon and diamond substrates and the role of CO during the deposition see the Section 3.2.

All the growth and film analyzation experiments were done in the ultra-high vacuum (UHV) system PINUP (Projekt Ionenneutralisation und Ultraviolett Photoelektronenspektroskopie) – μ-metal chamber with the base pressure of 5×10^{-11} mbar. The chamber is equipped by an ion sputter gun with a Wien filter, a broad-beam ion gun for sputtering, two electron-beam evaporators, a Knudsen effusion cell, quartz crystal microbalance (QCM), Low-energy electron diffraction (LEED), Auger electron spectroscopy (AES), H-cracker and SMOKE.

4.1. Metastable film on diamond substrate

In the conclusion of his diamond chapter in the dissertation thesis Gloss mentions the possible use of diamond crystals with step-bunching and large terraces fabricated in Augsburg [18]. These crystals are grown via microwave plasma chemical vapor deposition (MWPCVD) on the Ir/YSZ/Si template [46] in a microwave resonator with a power of 30 kW [Figure 4.1 (a)]. The grown crystal is shown in the Figure 4.1 (b), (c). Here we present the experiment of the deposition of the 12 nm $Fe_{78}Ni_{22}$ layer on such a substrate.

4.1.1. Preparation of the diamond(100) surface

It was shown that etching a diamond sample in the Piranha solution before inserting it in UHV makes no differences in the cleanness of the diamond crystal and properties of deposited iron-nickel films [18]. Therefore we introduced the MWPCVD grown diamond sample described above into UHV, outgassed it at 670°C (measured by a pyrometer on the molybdenum sample plate), etched it in atomic hydrogen from H-cracker (home-made source of atomic hydrogen added to the PINUP chamber by J. Gloss) in 3 cycles with elevated temperature (400°C, 500°C, 560°C) and annealed it at 810°C. The resulting dose of hydrogen was 10 600 L. After these procedures, we checked the purity and quality of the surface with AES and low-energy electron diffraction (LEED). In AES we saw no significant peak of impurities and G-factor [47] [ratio of the difference between the

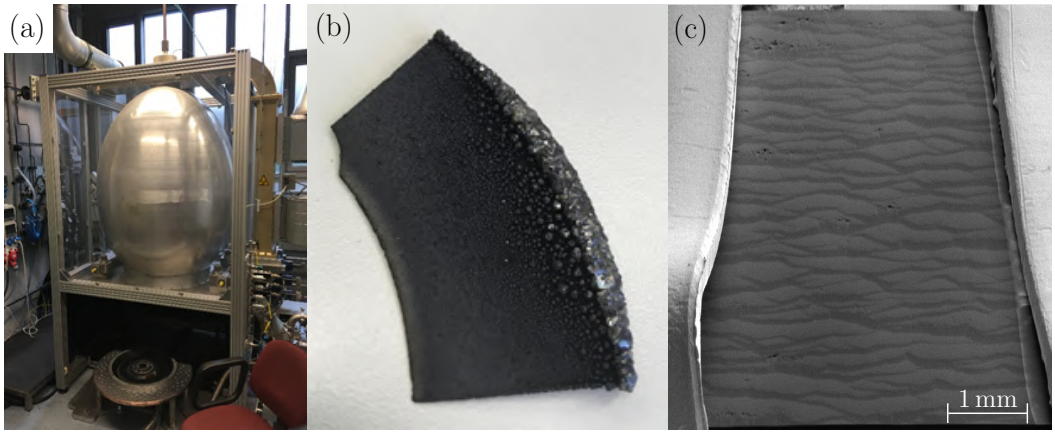

Figure 4.1: The growth of diamond single crystals. (a) Microwave resonator chamber for growth in Augsburg. The photo taken by L. Flajšman. (b) As grown piece of diamond after the MWPCVD process. The size of the imaged area is approx. $10 \times 10\,\mathrm{cm}^2$. (c) SEM image of a diamond sample clamped on UHV palette with visible terraces.

graphitic (sp^2) and diamond (sp^3) average peak-to-peak height (APPH) and the APPH of the whole C-peak] was -4.6 – comparable value with the previous succesfull experiments. More details about the G-factor evaluation during the cleaning procedure can be found in [18]. In the Figure 4.2 one can see the difference between the LEED patterns from this experiment [Figure 4.2 (a), (b)] and the previous experiment on diamond single crystals done by Gloss [Figure 4.2 (c)]. I suggest that these differences may come from the step-bunching, terraces and other sources of the surface roughness.

4.1.2. Deposition of the metastable film

The deposition of 12 nm of iron-nickel took place in the next step. The temperature of the sample was kept between 475 °C and 505 °C (measured by a pyrometer on the sample plate) during the deposition in CO atmosphere (between 4.8 and 5.4×10^{-10} mbar). The deposition rate was 1.33 Å per minute.

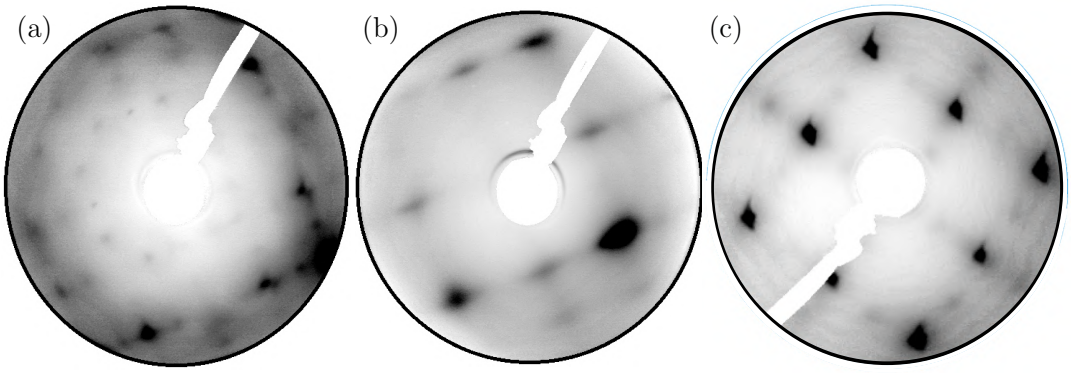

Figure 4.2: LEED images of diamond before deposition. (a) LEED at 260 eV after hydrogen etching by 10 600 L. (b) LEED at 140 eV after hydrogen etching by 10 600 L. (c) LEED of single crystal diamond [different sample then in (a), (b)] at 125 eV after hydrogen etching by aprox. 1000 L. Taken from [18].

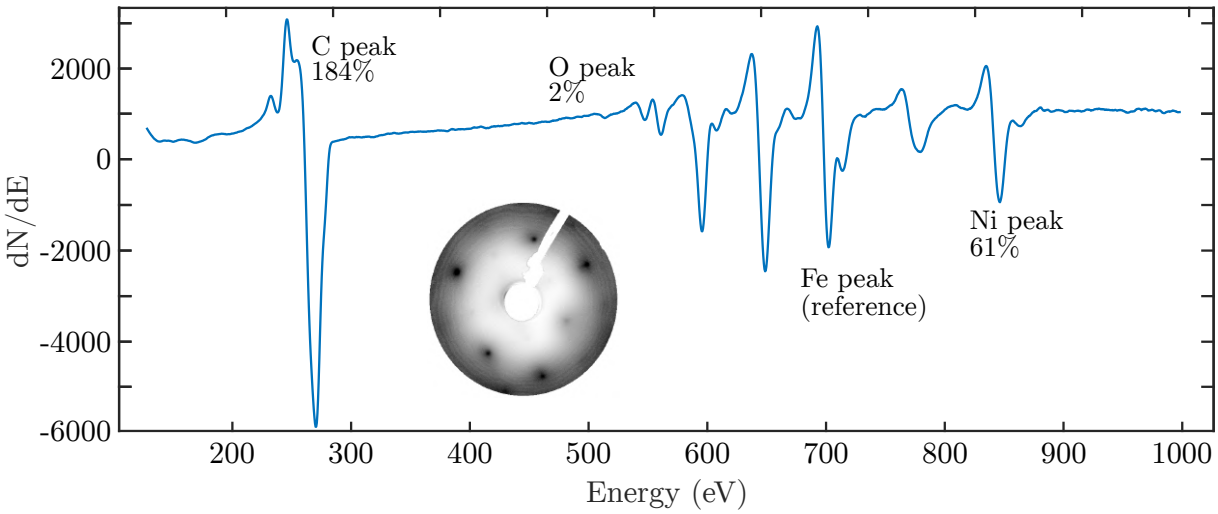

Figure 4.3: Analysis of 12 nm $Fe_{78}Ni_{22}$/C(100) deposited at temperature 475 – 505 °C. AES spectrum of the film with relative heights of peaks in comparison with the iron peak is depicted. Inside the graph, LEED pattern at 210 eV with the visible fcc(100) pattern is placed.

The deposited film was investigated via several techniques. Figure 4.3 shows an AES spectrum of the iron-nickel film and LEED pattern, which shows the fcc structure. Unfortunately, SMOKE could not be measured in-situ because of the scattering of the laser beam by the terraces of the sample.

The rest of the analysis was done in Brno. We get similar images of the island-like surface by the SEM observation as from previously done deposition on a diamond substrate. Slightly magnetic behavior were then observed in the Kerr microscope.

4.1.3. Discussion and conclusion of the experiment

We deposited thicker iron-nickel film (12 nm) at a higher temperature (approx. 490 °C) on the different crystal (with terraces and step-bunching) than in previously done experiments. The cleaning of the sample was already discussed in the Section 4.1.1. We suggest that the nature of the LEED pattern after cleaning may come from step-bunching, terraces and other surface roughness. In the Figure 4.3 one can observe in the AES spectrum the same carbon triple peak as was presented by Gloss [18]. This most probably comes from the formation of a new phase of Fe:C. On the other hand, the C:Fe ratio of APPH is different from previous experiments. Gloss presented in his chapter 6. 3. 1. the decrease of this ratio with the increasing thickness of the film [18]. He conducted a similar experiment to our own using an 8 nm thick film deposited at 450 °C. In that experiment, he measured a C:Fe ratio of approx. 1 while we observed the value of this ratio 1.84. This was caused by the higher deposition temperature and, possibly, due to a different intermixing process. We compared the SEM images with previously deposited films. In our experiment, the growth mode was still island-like but the shape and size of islands significantly differs. In principle, a higher temperature is enough for better diffusion and thus more 3D-like growth (higher island covering a lower fraction of the surface).

4.2. Metastable film on silicon substrate

It was already mentioned in Section 3.2 that with the increasing thickness of the Cu buffer layer on the silicon substrate the resulting surface morphology of the metastable film improves. In this section we report on the experiment with the thicker Cu buffer layer than in usual experiments (e. g. from the [40] paper).

4.2.1. Preparation of the Si(100) surface

The experiment presented in this subsection was done on Si#31, a B-doped crystal with dimensions of $(3\times12)\,\mathrm{mm}^2$. This crystal was mounted into the home-build molybdenum sample plate for direct-current heating without any previous ex-situ chemical procedures. The drawings of the sample holder and heating stage can be found in Appendix D in [18]. The resistance of the mounted crystal against the ground was $2.5\,\mathrm{k\Omega}$. The crystal was then inserted into UHV chamber and outgassed via e-beam heater in the chamber manipulator. The temperature was held at 520 °C (emission current of the heater 30 mA) for 205 minutes with a maximum pressure of 4×10^{-8} mbar. To decrease the pressure, we then filled the cryo baffle of the chamber with liquid nitrogen (LN_2). Another round of outgassing was executed after transferring the crystal to the direct-current heating stage (for details see Appendix C in [18]). An applied voltage brought us a temperature of 572 °C measured by a pyrometer on the crystal.

In the next step, flash annealing took place in order to remove the native SiO_2 and contaminations. We used five 5-second cycles of flashing with a change of electric polarity after the 4^{th} one. This change must be done to compensate the flow of material in the opposite direction of electric current. Temperature of the crystal during flashing was 1150 °C. The crystal was then checked by AES (not presented here) and LEED. The LEED pattern after flashing, showing a (2×1) reconstruction, is in the Figure 4.4 (a).

The last step of the crystal preparation for the deposition was hydrogen termination. During this process, the atomic hydrogen from the H-cracker saturated the free bonds on the surface and made it inert. Since the last silicon experiment, a new turbomolecular pump was installed, in the PINUP main chamber. That changed the conditions during the termination and therefore the termination with the same parameters as before did not

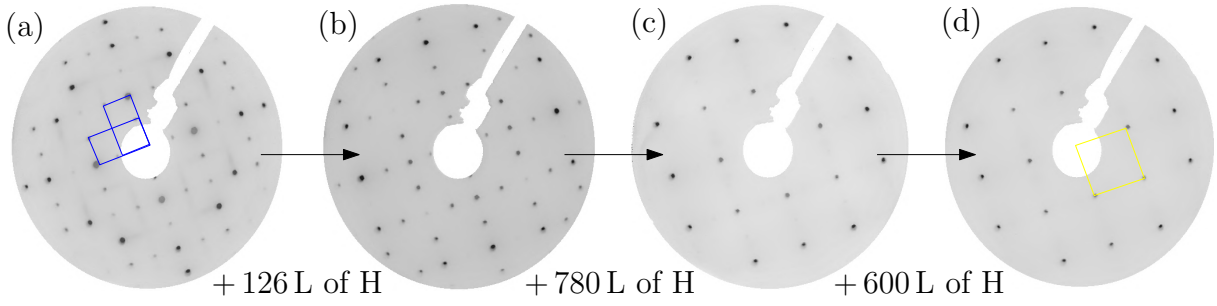

Figure 4.4: LEED images at 120 eV of the cleaning process of Si(100). The dose of hydrogen was calculated from the pressure measured by ion gauge in the main chamber. (a) LEED after 5 cycles of flashing at 1200 °C. Blue rectangles highlight the (2×1) reconstruction. (b) LEED after dosing atomic hydrogen (120 L). The (2×1) reconstruction is still strongly visible. (c) LEED after 906 L of H. (2×1) reconstruction is still slightly visible. (d) LEED after 1506 L of H. The (2×1) reconstruction disappeared and the yellow square highlights the (1×1) Si-unit cell.

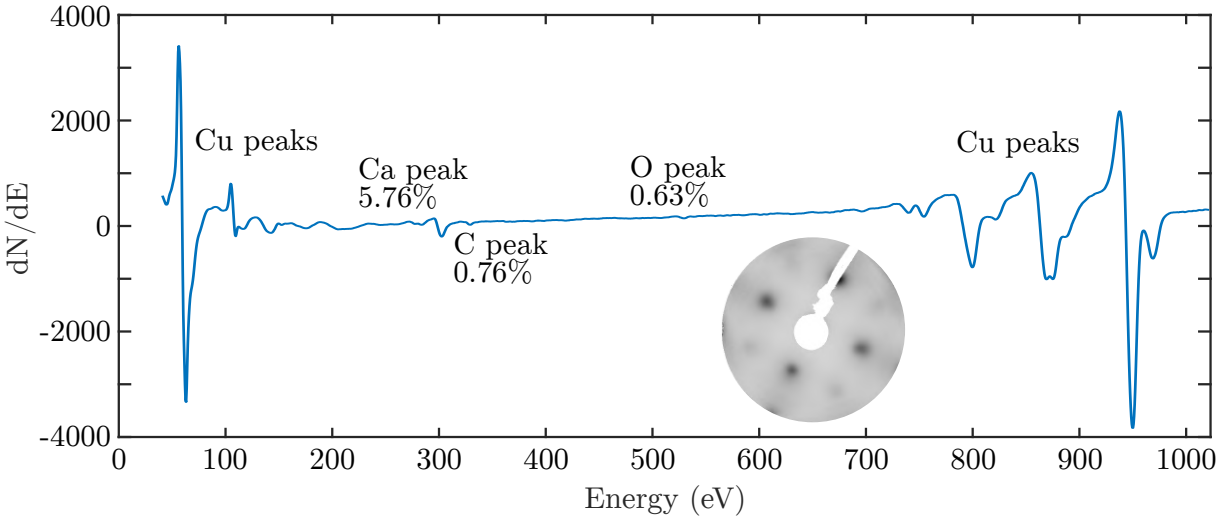

Figure 4.5: Analysis of a 180 nm thick Cu buffer layer. AES shows copper peaks and also peaks of oxygen, carbon and calcium with relative hight to main copper peak (920 eV). The inset is the LEED pattern at 140 eV of Cu(100). Visible are both silicon and copper (1×1) unit cells.

provide us enough hydrogen to saturate the whole surface. For the verification of these, we used LEED and checked the disappearing of (2×1) reconstruction spots. One can observe their gradual disappearance in the Figure 4.4 (b) – (d) with increasing hydrogen dose. The first cycle of termination was done at 1.5×10^{-7} mbar while the second and third at 1×10^{-6} mbar.

4.2.2. Growth of the Cu(100) buffer layer

We used a CreaTec effusion cell with Ca contaminations in the crucible for the deposition of the copper buffer layer. The cryo baffle of the chamber was cooled by LN_2 and the effusion cell was cooled by a constant flow of water during the deposition. The deposition of 180 nm of Cu was done in two steps because of the long deposition time. We deposited

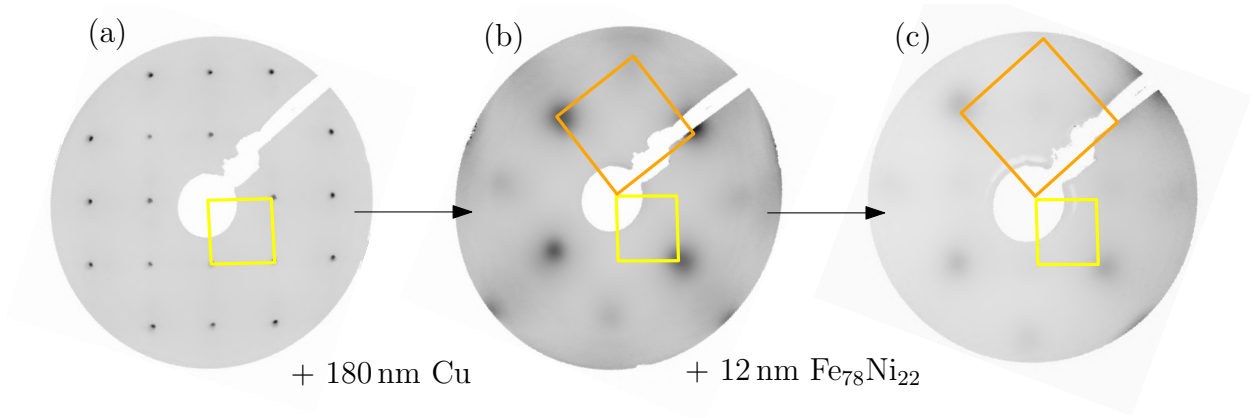

Figure 4.6: Development of the LEED images. Yellow rectangles mark (1×1) H-Si(100) unit cells and orange rectangles mark (1×1) fcc unit cells. (a) H-terminated surface from Figure 4.4 at 120 eV, (b) 180 nm thick Cu buffer layer at 140 eV, (c) 12 nm $Fe_{78}Ni_{22}$/180 nm Cu(100)/H-Si(100) at 120 eV.

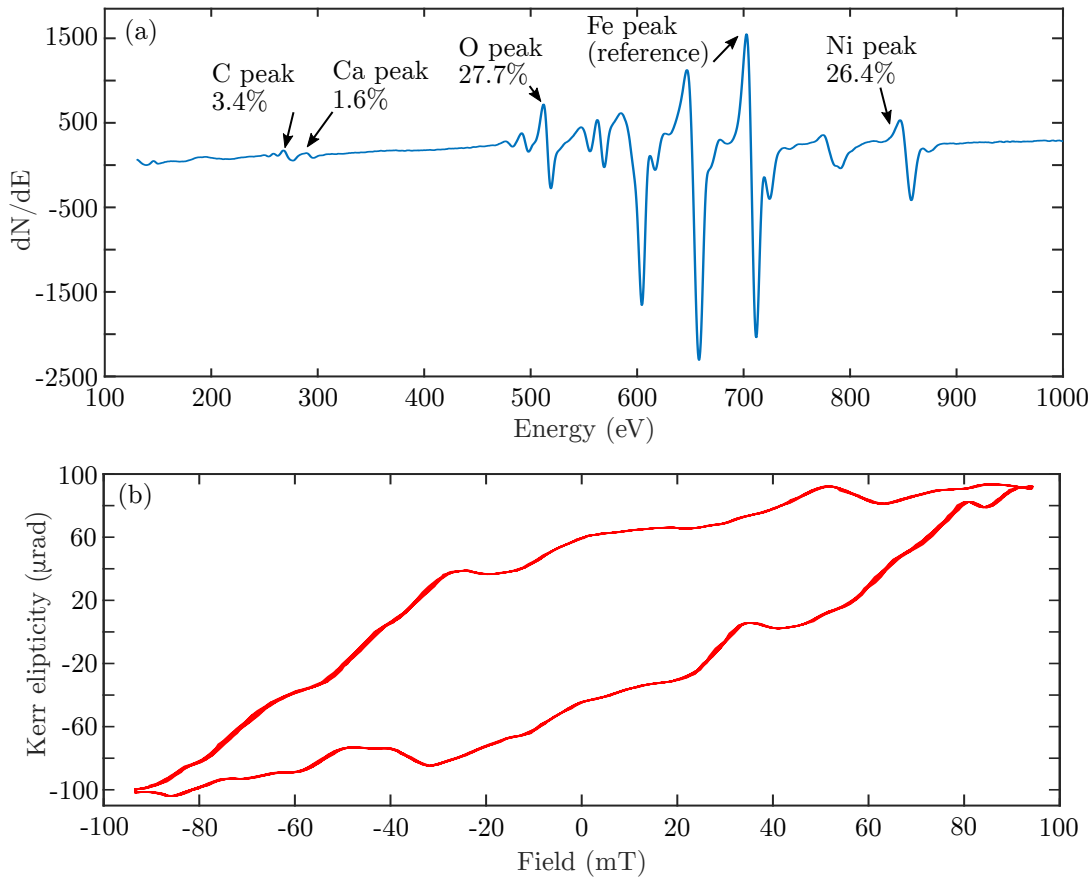

Figure 4.7: In-situ analysis of 12 nm $Fe_{78}Ni_{22}$/180 nm Cu(100)/H-Si(100). (a) AES with relative peaks height to main iron peak. Ca peak from copper deposition is still present though with a smaller relative amount. (b) SMOKE measurement with slightly ferromagnetic behaviour.

67.2 nm of Cu with a deposition rate of 3.2 Å/min (with an effusion cell temperature of 1055 °C) and the pressure between 1.5×10^{-10} and 8×10^{-11} mbar in the first step. Then in the second step we deposited 112.8 nm of Cu with a deposition rate of 3.68 Å/min (temperature of effusion cell 1060 °C) at a pressure of approx. 5×10^{-11} mbar. An analysis of the Cu layer is presented in the Figure 4.5. In AES, a Ca peak is visible. The inset shows the fcc Cu(100) pattern.

4.2.3. Deposition of the metastable film

We deposited 12 nm (same thickness which we use on copper crystals) of iron-nickel as the last step. We used an EFM3 e-beam evaporator cooled by LN_2 for the deposition. The deposition rate was measured by a QCM and was set to 1.33 Å per minute. The pressure before the deposition was 2.5×10^{-11} mbar. Unfortunately, during the CO setup, a CO pressure accident happened due to careless handling and CO expanded to the chamber to maximum pressure 1×10^{-4} mbar. Fortunately, this accident did not destroy anything. The iron-nickel deposition was then unusually unstable with a strong influence of the flow of LN_2. The pressure during deposition oscillated between 4×10^{-10} and 7×10^{-9} mbar. This instability might be due to the increased CO pressure and could have also affected the growth mode and quality of the film.

Analysis of the film took place after the end of the deposition. We measured LEED [see Figure 4.6 (c)], AES [see Figure 4.7 (a)] and SMOKE [see Figure 4.7 (b)], in situ in the PINUP apparatus.

Ex-situ analysis was then done in Brno. Two FIB dose tests [presented in Figure 4.8 (a), (b)] were done with the Focused Ion Beam/Scanning Electron Microscope FEI Helios NanoLab 660. These dose tests were executed with 30 keV Ga^+ ions with a beam current of 85.4 pA. Also the SEM images of the surface were taken in same microscope [see Figure 4.8 (c), (d)]. The surface texture and corrugations visible in the Figure 4.8 (d) are similar as in the previous silicon experiments.

The last analysis was done by Kerr microscopy. We analyzed both dose tests [presented in Figure 4.8 (a), (b)] but only the data from the second one are presented in the Figure 4.9.

4.2.4. Discussion and conclusion of the experiment

As can been seen in the Figure 4.9 we prepared a metastable (transformable by ions) iron-nickel film on the Cu buffer layer deposited on a silicon substrate. For the H-termination of flashed silicon, we found new parameters of this process as discussed in subsection 4.2.1. We planned to deposit a 180 nm thick copper buffer layer. From the QCM check after the end of the second part of the copper deposition we could determine a decrease of deposition rate with the same deposition parameters from 3.68 Å to 3.36 Å/minute. So the resulting layer was a little thinner than 180 nm.

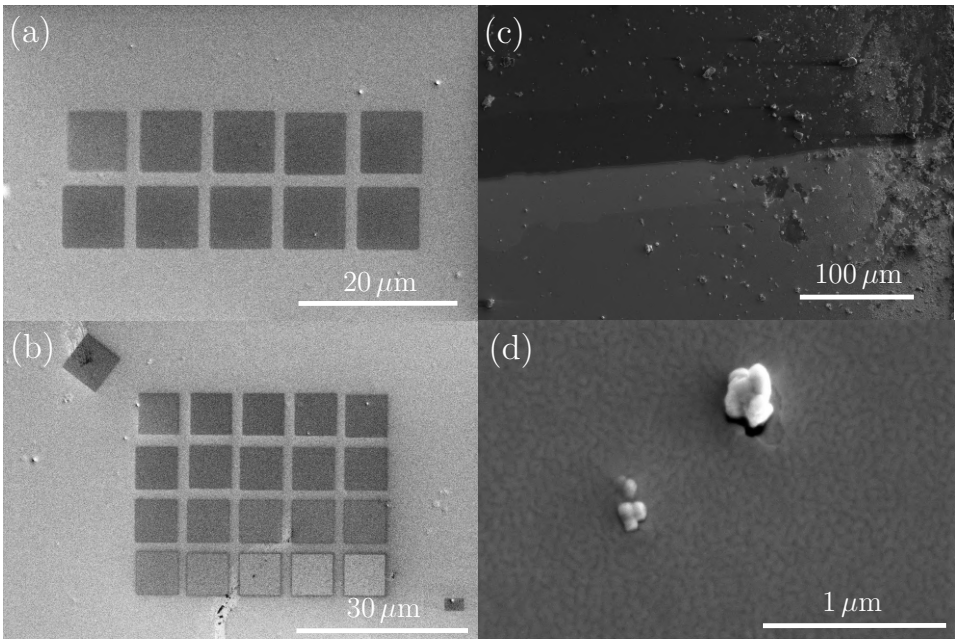

Figure 4.8: SEM images from Helios microscope. (a) Ion dose test with finer step in doses. The calculated doses range is from 5.34×10^{13} to 2.4×10^{15} ions/cm^2. (b) Ion dose test with a larger range of doses from 5.34×10^{13} to 2.67×10^{16} ions/cm^2. (c) Interface between the silicon area at the top (covered during the depositions) and the metastable-film area. (d) Detail of the iron-nickel surface texture with some impurities on the surface.

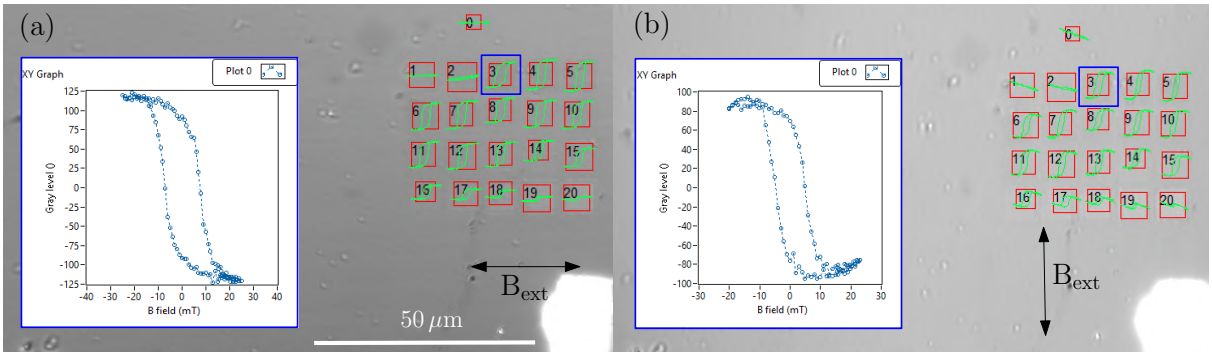

Figure 4.9: Analysis of the magnetic properties of the ion dose test in the Kerr microscope. Hysteresis loops for each structure are overlaping the image. In both subfigures, in the inset are details of the hysteresis loop of structure 3 where the fcc-bcc transformation was started. This structure had a dose of 5.34×10^{14} ions/cm^2. In (a) is configuration with parallel external magnetic field to FIB scanning direction. In (b) the external magnetic field is perpendicular to the FIB scanning direction.

After the iron-nickel deposition, an analysis presented in subsection 4.2.3 took place. In AES [see Figure 4.7 (a)] we can observe relatively high oxygen peak of 27.7 %. For example, Gloss presented in his thesis on silicon an oxygen peak with a relative height of 5 % [18]. The most probable explanation for this is the different thickness of the films (different deposition time) and the CO overshoot accident (reported in the first part of the subsection 4.2.3). In the hysteresis loop from the SMOKE measurement of the as deposited film [Figure 4.7 (b)] one can notice a stronger magnetic signal than in iron-nickel films on copper. However, this is typical on silicon and was presented before. This slightly ferromagnetic behavior comes from bcc domains, which grow in small amounts in the otherwise fcc film. Fortunately, this does not affect the fcc-bcc transformability of the whole film.

As we remarked in the caption of Figure 4.8, the iron-nickel grew with a grain surface texture. This can be one possible explanation why we cannot see the initiation of bcc grow as on copper crystal on SEM images [see Figure 4.8 (a), (b)]. The initial dose of 5.34×10^{14} ions/cm^2 (see Figure 4.9) is approx. two times lower than on similar film transformed with a similar beam on copper. This agrees with the previous observation done by L. Flajšman. I suggest that this might come partly from surface grains and partly from as-deposited bcc grains which can serve as nucleation points to the transformation. Another interesting property of the film is the magnetic anisotropy. In Figure 4.9 we can observe a slightly different shape of hysteresis loops in easy and hard axes, but the data are not sufficient to deduce the anisotropy quantitively.

4.3. Influence of the CO backpressure on the magnetic properties of the metastable films deposited on copper substrates

It was observed, that deposited metastable films had different crystallography and magnetic behavior. One of the possible explanations is the different CO pressure during depositions. Furthermore, recently 22% of nickel was identified as an ideal Fe-Ni ratio for

the growth of a metastable FeNi alloy. Unfortunately, the phase diagram in the Figure 3.2 does not contain many points for $Fe_{78}Ni_{22}$. The lack of experiments focused on the CO pressure influence on the growth of metastable fcc $Fe_{78}Ni_{22}$ together with discrepancies in the magnetic properties of the seemingly similar samples motivated us to established the role of CO in the growth as the main goal of my Erasmus research stay. Therefore, in this subsection, we present a set of depositions with different CO pressure and subsequent magnetic analysis to find the linkage between the CO pressure and properties of the deposited films.

4.3.1. Preparation of the Cu(100) surface

The Cu(100) surface was, prior to the deposition of FeNi, treated by sputter anneal cycling. Sputtering was realized with 2 keV Ar^+ ions leading to the removal of the previous FeNi film and also surface impurities (C, Ca, S, ...). Annealing is realized by the e-beam bombardment of the back of the sample plate. The temperature of the sample is measured by a thermocouple or by a pyrometer. Annealing serves for both removing the surface oxygen and other gas molecules and also for restoring a well- ordered, flat surface after the sputtering. Usually, we used three cycles of sputtering (the first for approx. 40 minutes and the others for 10 minutes). Usual sputtering parameters are: sample current $I_s \approx 6\,\mu$A, chamber argon pressure 4×10^{-6} mbar, energy of Ar^+ ions 2 keV. Each sputtering cycle was followed by sample annealing to approx. 520 °C. For the preparation of virgin crystal (first use of the crystal) the substrate was first sputtered at elevated temperature (400 °C) in order to remove sulfur impurities segregated from the bulk of the crystal. The purity and quality of the crystal surface were verified after each step by AES and LEED.

4.3.2. Deposition of the metastable film

The deposition of iron-nickel on Cu(100) was realized by the electron beam bombardment of the $Fe_{78}Ni_{22}$ rod in the EFM3 evaporator. The evaporator and the cryobaffle of the titanium sublimation pump (TSP) are cooled by liquid nitrogen (LN_2) during the deposition. We ran the TSP before filling CO to the chamber. We set the nominal thickness of the film to 12 nm (enough for follow-up magnonics experiments), and the deposition rate to 1.33 Å per minute (measured by a quartz crystal microbalance). During the deposition we applied a voltage of 1.5 kV at the orifice of the evaporator to avoid transformations of the film by energetic ions from the evaporator during the deposition.

4.3.3. Design of the CO experiment

We ran several depositions of 12 nm of $Fe_{78}Ni_{22}$ (for summary see the Table 4.1) with a range of CO pressures between 4×10^{-11} and 1×10^{-6} mbar. After the in-situ analysis (AES, LEED, SMOKE) we performed micropatterning with different 30 keV Ga^+ ion doses using a FIB/SEM electron microscope. The irradiated areas were then analyzed by Kerr microscopy and Labview software postprocessing. We observed mainly two properties of the film: anisotropy field (from the fitting of the hard axis hysteresis loop) and the ion dose needed for initiating the fcc-bcc transformation. We have chosen the initial dose and not the dose needed for the maximum magnetic saturation because the value of the magnetization strongly depends on the manually chosen area in the software; the software

determines the average grey level of the whole area. So we can more accurately determine the dose where the fcc-bcc transformation starts.

4.3.4. Characteristics of microscopes used for fabrication of the ion dose tests

At the beginning of this work, we used a FIB/SEM TESCAN LYRA3 as was usual also in the past in the experiments done by L. Flajšman or V. Křižáková [43], [6]. Unfortunately, in June 2019 the LYRA FIB was sent to France for service. To continue with the FIB experiments we continued on another, for us no as well known, microscope system – FIB/SEM FEI Helios NanoLab 660.

In the LYRA3 experiments, the ion dose was usually calculated from beam current, dwell time, and pitch of the beam (used for example in [4] or [43]). The Helios operation software has the ion dose as one of its output parameters. This value was found to be highly inaccurate. This was also confirmed by the manufacturer (Thermofisher Scientific). For that reason, we calculate the dose the same way as in LYRA3. As we show below, the ion dose values for the fcc-bcc transformation of a given sample using the Helios are lower than the LYRA ones. One explanation we found is the not well-defined value of the pitch of the Helios beam (the set value of 10 nm is not realistic).

We also made the analysis of the profile of the ion beams in both microscopes. Post process analysis of the Gaussian profile of the ion beam was done at the chosen surface step from the images in software ImageJ. In the analysis, dX is 1/e of a width of an error function (equivalent to the convolution of a Gaussian curve with a step function). The chosen step has a big influence to the quality of the fit and, thus, to the width of the

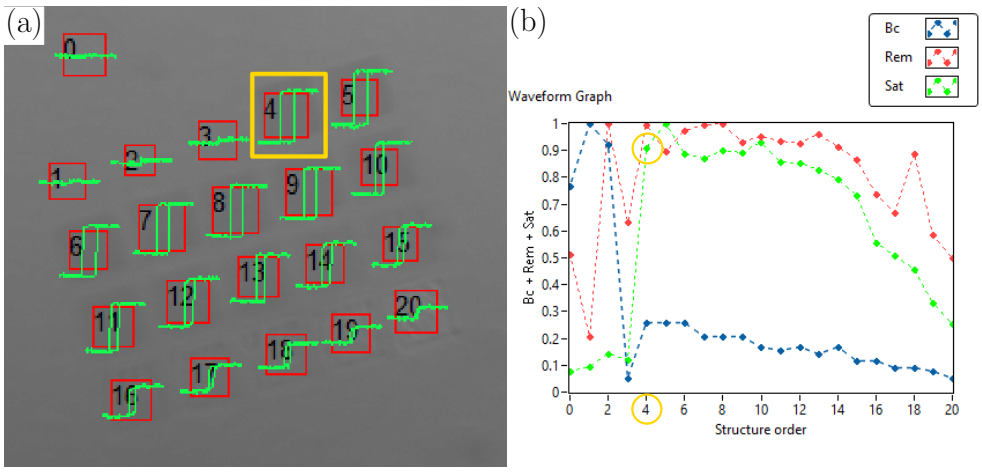

Figure 4.10: Determination of the ion dose needed to initiate the growth of bcc phase. In this case (Cu#17, CO pressure 5×10^{-10} mbar) the initial dose corresponds to structure number 4 (marked by gold markers on both parts of the Figure). (a) Image from the Kerr microscope with overlapping hysteresis loops for each structure in the dose test. (b) The magnetic properties coercivity, remanence, and saturation (in arbitary units) determined for the loops. For the determination of the initial ion dose the most important curve is the one representing the magnetic saturation (green). The x axis (labeled as structure order) coresponds to increasing ion dose in the range of 10^{13} to 10^{16} ions/cm^2. The steps on the x axis are not a linear function of the ion dose. The exposure times for the steps are between 400 ns and 5 µs.

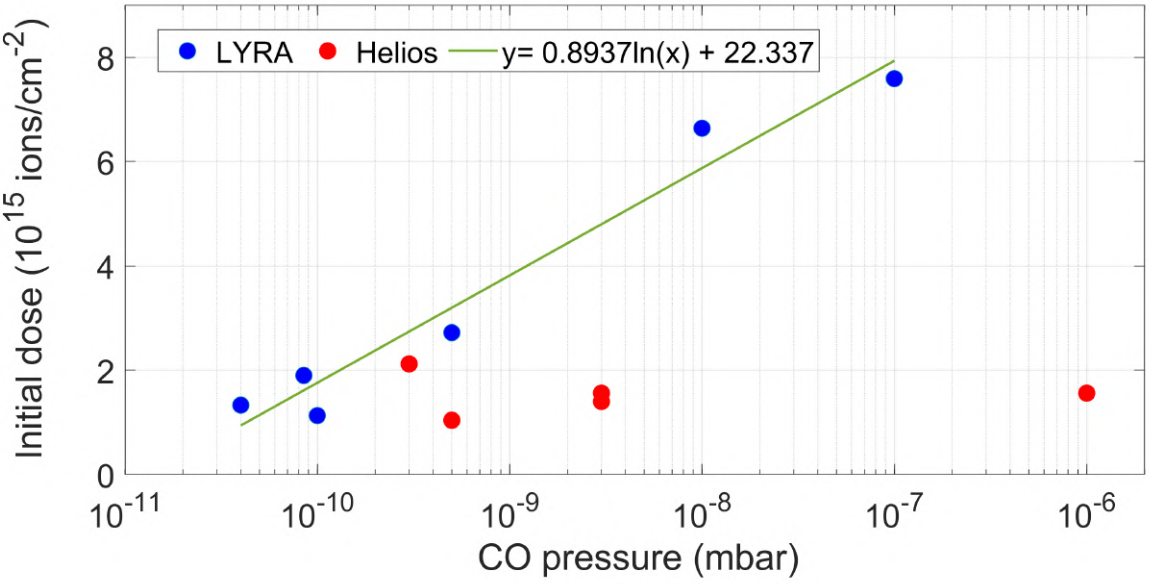

Figure 4.11: Dependence of the initial ion dose on the CO backpressure during the deposition for films irradiated in both microscopes. In the LYRA case we are able to fit the data (fitting equation visible in the legend), which is impossible in the Helios case. Details about some data points are mentioned in the text.

Gaussian curve so the analysis is not very accurate. By finding the sharpest step we tried to make them as accurate as possible. The Gaussian profile of the Helios beam (dX = = 27.1 nm) is narrower than the LYRA one (dX = 35.2 nm). We suggest that with better defined profile of the beam we need a lower calculated ion dose (more localized energy deposition), which is consistent with data presented in the Figure 4.11. Unfortunately, we cannot easily compare results for both microscopes so we present them separately below.

4.3.5. Initial ion dose for the fcc-bcc transformation

The initial dose values were obtained from the analysis of the Kerr microscope measurements in the Labview software programmed by L. Flajšman. One case of this analysis is shown in the Figure 4.10. The concept of the initial ion dose is described in the caption of this figure.

We analysed data from all crystals and plotted them in the Figure 4.11. In the LYRA part we can see a fit of the dose vs the logarithm of the CO pressure. These data were measured on samples Cu#16 and Cu#17 with 12 nm thick iron-nickel films. Only the film deposited at a pressure of 5×10^{-10} mbar had a thickness of 8 nm. After the deposition at 1×10^{-10} mbar we observed lots of terraces (visible in SEM) on the surface. That can be the reason for reduced value of the initial dose. Unfortunately, in the Helios data we could not determine any correlation between the initial ion dose and the CO pressure. The data measured after deposition with pressures of 3×10^{-10} and 3×10^{-9} mbar come from virgin crystals of Cu#18, Cu#19, which could influence the quality of the iron-nickel films and its properties.

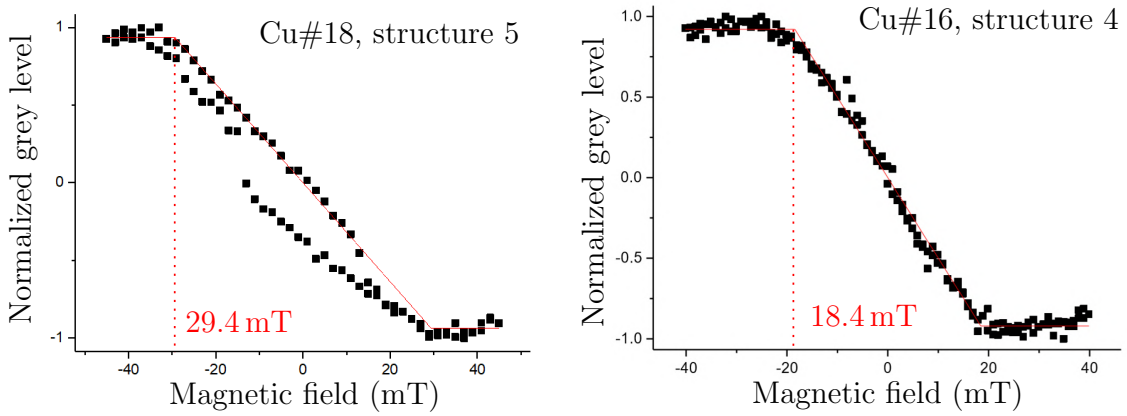

Figure 4.12: Hysteresis loops of iron-nickel films deposited on different crystals at the same pressure 3×10^{-9} mbar. The films show different anisotropy fields (dotted lines).

4.3.6. Magnetic anisotropy of the films

Magnetic anisotropy is an important property for applications in magnonics. Therefore, for every dose test, we took hysteresis loops from the structure with the initial dose (these loops have the highest anisotropy) and used the Origin software to fit the data by three line segments, two horizontal ones and a slope between them (see Figure 4.12). From this fit, we can extract the value of the anisotropy field (field necessary to saturate the structure).

In the Figure 4.13 is a plot of the magnetic anisotropy as a function of the CO backpressure for samples irradiated in both microscopes. We can see that the Helios data points have on average higher values. The highest anisotropy fields are found in the interval from 3×10^{-10} to 3×10^{-9} mbar; the anisotropy decreases with increasing CO pressure.

In the Figure 4.13 it is also visible that there are are two data points with a big difference between their values at a pressure of 3×10^{-9} mbar. Fits of both loops are presented in the Figure 4.12. A possible explanation is a fact that the crystal with the higher anisotropy field (29 mT) is virgin. Therefore its surface had fewer defects, which

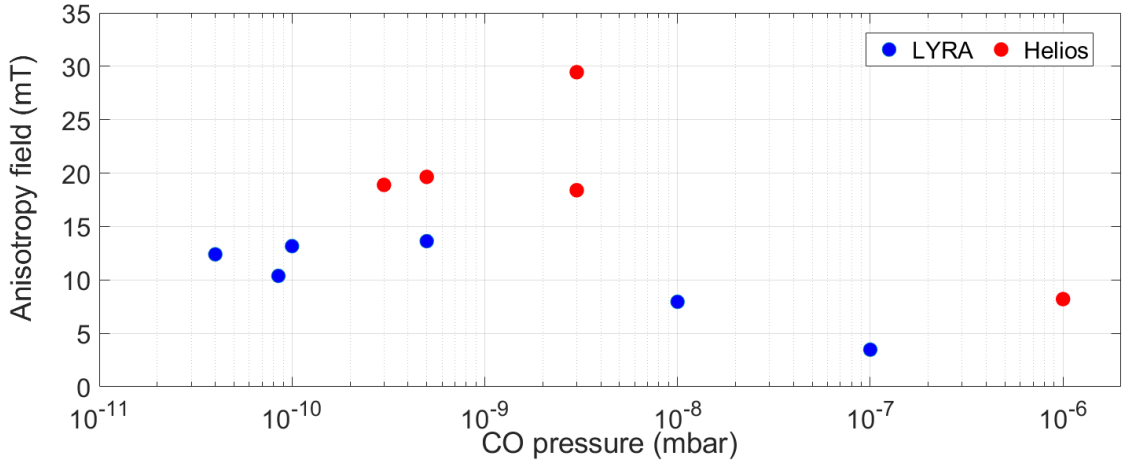

Figure 4.13: Analysis of the anisotropy field as a function of the CO backpressure during the deposition. Data extracted from the analysis described in the Figure 4.12.

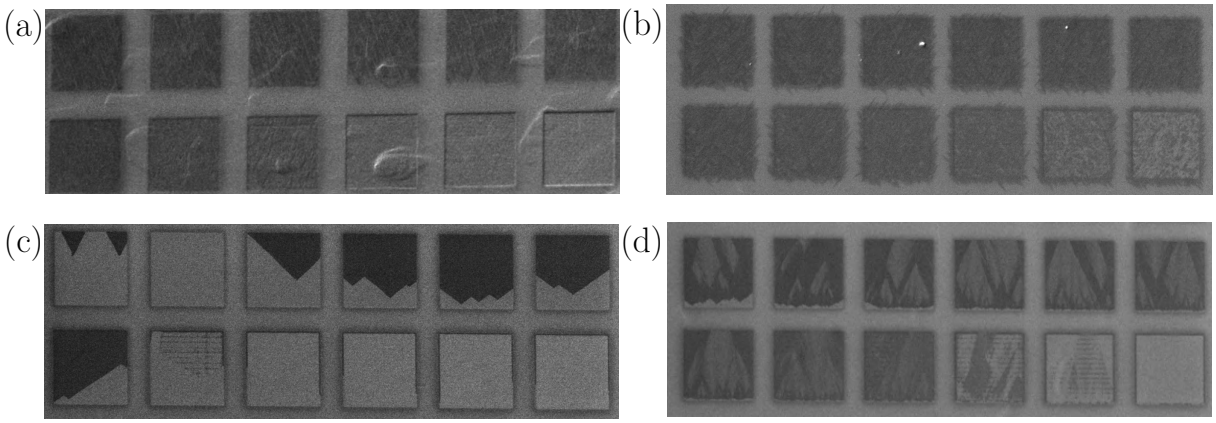

Figure 4.14: Different types of bcc growth. Black color corresponds to the bcc phase. White colur in the second line of the squares corresponds to the whole film sputtered away.

is expected to have a positive influence on the magnetic properties of the deposited films. Unfortunately, this breaks our intention to determine a simple dependence between CO pressure and magnetic anisotropy because other parameters also play a significant role.

4.3.7. Types of fcc-bcc transformations

During the experiment, we observed different types of initiation and bcc growth. Investigating these growth modes more in detail in follow-up work should help us to better understand the fcc-bcc transformation via FIB. Four main modes are presented in the Figure 4.14. In all subfigers, the black area clearly corresponding to the bcc phase. On the other hand, it is not clear whether the white color corresponds to the fcc phase or the film sputtered-away. In (a) are visible small needles in bcc areas. In (b) bcc needles protruding from the irradiated structures. In (c) the initiation at the defects and consequence homogenous growth is presented. The borders of the bcc areas with untransformed fcc ones in all structures have similar angles. That might be in the connection with the crystallography and characteristic rotation of the bcc lattice. In (d) different grayscales textures in transformed bcc areas are visible. To investigate their origin the view to crystallography is necessary.

Other observed difference from the magnetic measurements is in the manner of the initiation of the growth (an increase of the magnetization) and removal of the film. In some cases, it takes place in one step in the doses. In the others that take place continuously in a wide range of the ion doses.

Unfortunately, no straightforward explanation for this growth modes and different behavior was discovered. The variables which can play a role are: CO backpressure during the deposition, angle of a FIB scanning with respect to crystallographic directions during the irradiation, purity and flatness of the copper substrate crystal and its history (virgin crystal versus the many times used one).

4.3.8. Summary of the CO backpressure experiments

We executed a series of iron-nickel depositions on copper and varied the CO backpressure during the deposition. All the successful depositions are summarized in Table 4.1. There were also unsuccessful experiments. Part of them was done on Cu#12 and Cu#13, which

Table 4.1: Overview of all successfully transformed samples from the CO experiment. Contents of carbon and oxygen were taken from AES measurements and were presented as % of the main iron peak.

Crystal	$\mathbf{p_{CO}}$ **(mbar)**	**C and O**	**FIB**	**Initial dose [10^{15}ions/cm^2]**	**Anisotropy (mT)**
Cu#16	1×10^{-10}	–	LYRA	1.13	13.2
Cu#16	3×10^{-9}	1 %; 34.5 %	Helios	1.4	18.4
Cu#16	1×10^{-8}	0.4 %; 34.8 %	LYRA	6.64	7.9
Cu#16	1×10^{-7}	2 %; 43 %	LYRA	7.59	3.5
Cu#16	1×10^{-6}	2.3 %; 43.4 %	Helios	1.04 - 2.08	8.2
Cu#17	4×10^{-11}	1 %; 2.5 %	LYRA	1.33	12.4
Cu#17	8.5×10^{-11}	7 %; 7.1 %	LYRA	1.90	10.4
Cu#17	5×10^{-10}	1.5 %; 18 %	Helios	1.04	19.6
Cu#17 [1]	5×10^{-10}	–	LYRA	2.72	13.6
Cu#18	3×10^{-9}	0.9 %; 29.5 %	Helios	1.56	29.4
Cu#19	3×10^{-10}	1.7 %; 20 %	Helios	2.12	18.9

were contaminated during the fabrication of the waveguides by the lithography process. We identified carbon coating on their surface by Energy-dispersive X-ray spectroscopy (EDX) analysis in the LYRA3 microscope. One deposition on Cu#17 was done from the end of the FeNi rod in the evaporator and was therefore very unstable. Nevertheless, we did the dose test and all of the structures had the same hysteresis loops in Kerr microscope. But it is possible that we measured the dose test from the previous experiment which is still visible. Higher doses of gallium ions sputter away not only the iron-nickel film but also copper. It seems that these holes are deep enough to not to be flat again after the sputter-anneal cycles. This problem may also occur in future experiments when a crystal is reused. Therefore we started to fabricate distinguishing structures as part of the dose tests.

One of the motivations for this CO experiment was to verify different regions presented in the phase diagram in the Figure 3.2. We showed that also with pressures of 4×10^{-11} (base pressure without added CO) and 1×10^{-6} mbar we are able to deposit metastable $Fe_{78}Ni_{22}$ films (see Figure 4.11 and Table 4.1). This contradicts the borders of the metastable region from Figure 3.2 because for these pressures Gloss expected ferromagnetic bcc and stable fcc behaviour, respectively. However, Gloss transformed the films by the broad 2 keV Ar^+ beam and not by FIB. It is possible that films that are stable fcc under the Ar^+ irradiation can be transformed with the FIB.

[1] 8 nm of iron-nickel. Rest of the samples had 12 nm.

5. Crystallographic experiments

In this chapter, we present the crystallographic experiments done on structures fabricated by FIB in metastable iron-nickel films. In the Section 5.1, we present typical workflow of the EBSD measurement, which is a crucial experimental technique for this thesis. In the Section 5.2, we discuss the EBSD data processing in the OIM software. In Sections 5.3 – 5.7, we present five experiments aimed at probing different crystallography properties of the structures prepared with different FIB parameters. The details about the fabrication of the studied structures are described in the Appendix A.

5.1. EBSD measurement workflow

All EBSD measurements were done in High-Resolution Scanning Electron Microscope FEI Verios 460L (Verios). As was already mentioned in the Section 2.2.3, a sample tilt of 70 ° from the horizontal direction, is needed for the observation of Kikuchi diffraction patterns. Unfortunately, the maximum Verios stage tilt is 55 °. Therefore, a special sample holder with a pre-tilt of 15° is usually used for EBSD measurements [see the Figure 5.1 (a)].

After inserting the sample into the microscope chamber, alignment of the electron beam is done first. Then, we tilt the sample and insert the retractable EBSD detection camera into the chamber. Afterward, the camera parameters are set.

The camera parameter called binning must be chosen first. By this parameter, it is possible to determine how many pixels are merged together. By this merging, thanks to the increase of the image intensity, the image capture frequency will also increase. On the other hand, binning decreases the image resolution. So in the dependence on the dimensions of the analyzed area and the required resolution, we choose the appropriate binning. In the experiments presented in this thesis, we typically use 2×2 and 8×8 binning. For better signal-to-noise ratio, we use averaging of 64 images.

In the next step, we need to find a homogenous area on the surface, let the electron beam scan over it and tune the camera exposure time and gain until we can observe nice and clear Kikuchi pattern at the camera screen. An example pattern is presented in the Figure 5.1 (b).

Then, we set up the pattern image processing procedure. First, a background signal is measured. Two background types are used: usually used static background and a dynamic background, which must be used for our system of transformed bcc structures in thin film on the copper fcc substrate. This is necessary for dealing with the low contrast and noisy diffraction patterns images. Static background in similar single grain systems can remove the pattern completely instead of smoothing it. Dynamic background techniques are based on blur filtering before the background extraction [48]. Specifically, we use the function called *dynamic background division* followed by *intensity histogram normalization*. After that, the background signal is acquired. The recognition of the patterns must be tested

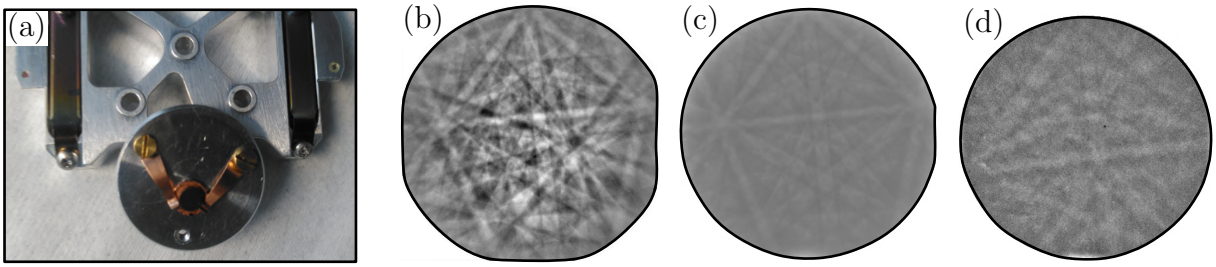

Figure 5.1: EBSD measurement in the FEI Verios 460L. (a) Copper crystal with the metastable layer placed on 15° pretilted sample holder for EBSD measurement. (b) Background, (c) fcc, (d) bcc Kikuchi patterns acquired during the setting of the EBSD measurement.

before the orientation mapping can be started. For this purpose, we use the pattern from the dose test fabricated during the structure preparation. We know from the previous experiments that the transformed areas possess a bcc-lattice. With this knowledge, we can perform spot pattern acquisition and autoindexing. Based on the result of the Vote scheme (mechanism for determination of the crystallographic orientation described in the Section 2.2.3), we consequently tune the parameters of the image processing, pattern indexing, and Hough transformation. Examples of measured fcc and bcc patterns are shown in the Figure 5.1 (c) and (d), respectivelly.

When we are satisfied with the indexing results [points from the dose test pattern are indexed as bcc with high confidence index (CI) – see Section 2.2.3], we can proceed to the orientation mapping measurement. In the end, we set the dimensions of the measured area and the scanning step and start the measurement. Based on the measurement parameters, a running time is calculated. Typical measurement takes approx. 10 – 14 hours. When the measurement is finished, we retract the camera and withdraw the sample.

5.2. EBSD data processing

As was mentioned in the Section 2.2.4, we use OIM Analysis™ software for postprocessing and visualization of raw EBSD data. Measurement output dataset consists of crystallographic information extracted from Kikuchi patterns from each point (pixel) of the measurement. OIM Analysis™ software offers a rich variety of tools for editing and visualizing them. Usually, we start with rendering of a 2D phase map [presented in the Figure 5.2 (a)] and the orientation inverse pole figure (IPF) map [presented in the Figure 5.2 (c)] from the raw data.

Then we perform a so-called cleanup data process. The Kikuchi pattern indexing is generally quite effective in identifying the orientation from the diffraction pattern. However, sometimes the software has difficulty identifying some orientations, e. g. at the grain boundaries where the patterns are often made up of two superposed diffraction patterns from both crystal lattices separated by the grain boundary. This will lead to wrong results at some points [15]. As a grain, you can consider a cluster of pixels with the same orientations. Practically, the grains are defined in OIM by minimum and maximum size and grain tolerance angle. OIM software provides several cleanup methods, which attempt to ”clean up” the erroneous data. These methods generally clean up individual data points based on the orientations of neighboring pixels. This cleaning procedure is based on changing the data so a care must be taken to avoid introducing any artificial

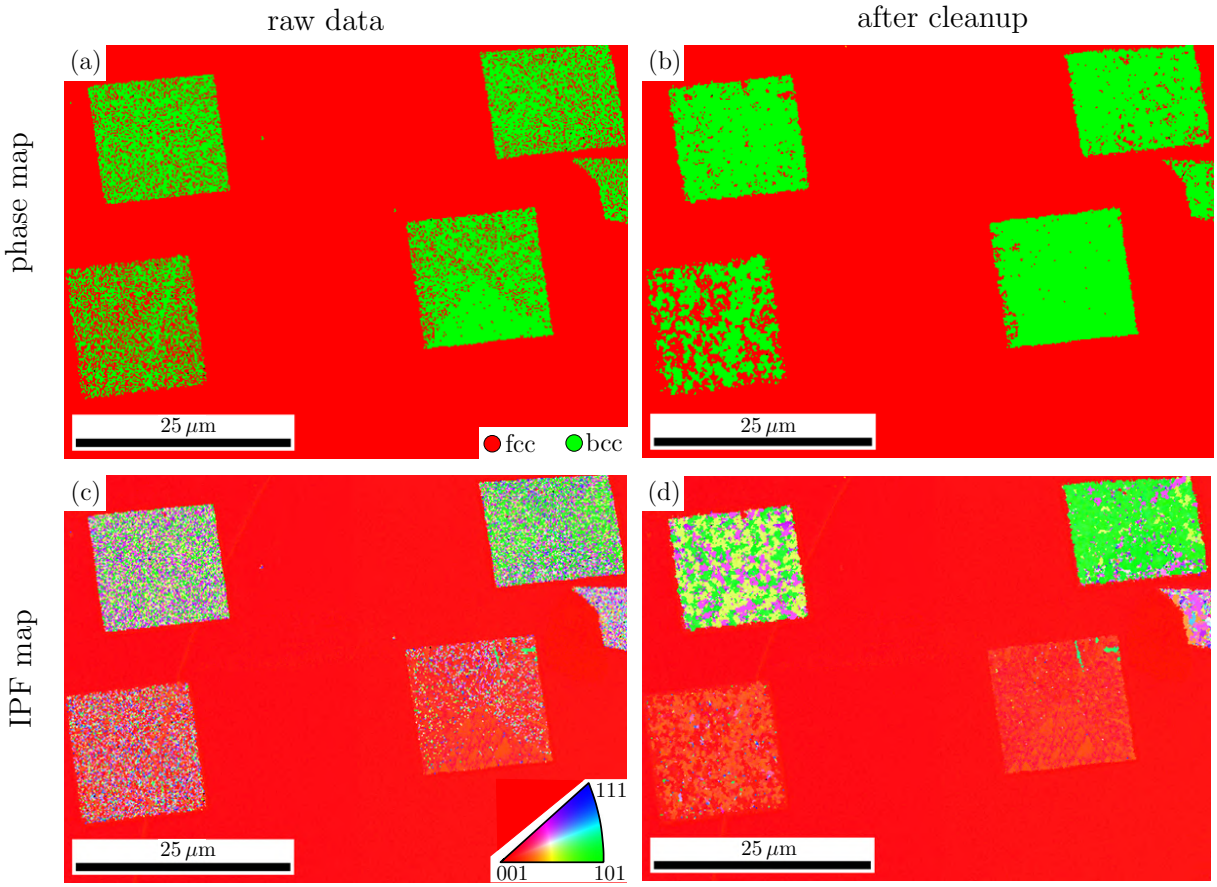

Figure 5.2: Demonstration of the data cleanup process on EBSD data measured on *Structures I.* (a) Raw data phase map, (b) phase map after cleanup, (c) raw data IPF map, (d) IPF map after the CI based cleanup process.

trends into the data. In the following paragraphs, we describe three cleanup methods used in this thesis.

First, we usually perform nondestructive *Grain CI standartization*. The CI is a crucial parameter for all cleanup methods. This cleanup method changes the CIs of all points in the grain to the maximum CI found among all points belonging to the grain [15]. It essentially enables a point with a low CI, yet having an orientation similar to that of the surrounding measurements and thus likely representing the correct indexing, to be distinguished from a point with a low CI where no correlation exists between the point and its neighbors (most likely representing an incorrect orientation measurement). It should be noted that no modification of the crystallographic orientation is made in this cleanup method, it simply upgrades the confidence index.

In the following step, we apply *Neighbor Orientation Correlation*. This cleanup method operates by examining each data point individually and testing it for three conditions. First, the CI must be lower than some adjustable minimal treshold value (normally, we use 0.1). The second condition is a check to determine whether the orientation is different from its immediate neighbors. If the required number of nearest neighbors differs, the third condition is tested. This condition determines the number of nearest neighbors with similar orientations within the given tolerance angle. If both the second and the third conditions are satisfied, the orientation of the point changes to the orientation of one of the neighbors which satisfied second and third conditions (the choice is random) [15].

Finally, we perform *Grain Dilation* iterative method. The routine acts only on points that do not belong to any grains but still have neighboring points, which do belong to grains. A point may not belong to any grain due to the point either not being indexed or due to it belonging to a grain group having fewer members than the set minimum grain size. If the majority of neighbors of a particular point belong to the same grain then the orientation of the particular point is changed to match that of the majority grain. Otherwise, the orientation is randomly changed to match any of the neighboring points, which belong to grains. This process is repeated until each point in the data set becomes a member of a grain. Only points with CI values less than the specified minimum CI value will be modified.

This cleanup procedure was applied for every dataset presented in the thesis. The differences between the raw data and the data after the cleanup are visible in the Figure 5.2. OIM software provides plenty of possibilities to analyze the data. In the following paragraphs, we use some of them as cropping data only from some subarea or color highlighting specific point in 2D maps.

5.3. Experiment 1: Influence of the FIB energy and number of scans

The main goal of this experiment is to investigate the impact of the FIB energy and the number of scans used during the transformation on the resulting crystallography of the transformed bcc structures. Therefore, we designed the experiment as is sketched in the Figure 5.3. This experiment was done on *Structures I.* – four squares whose SEM image is presented in the Figure A.4 (a) in the Appendix and their fabrication is described in the Section A.2.

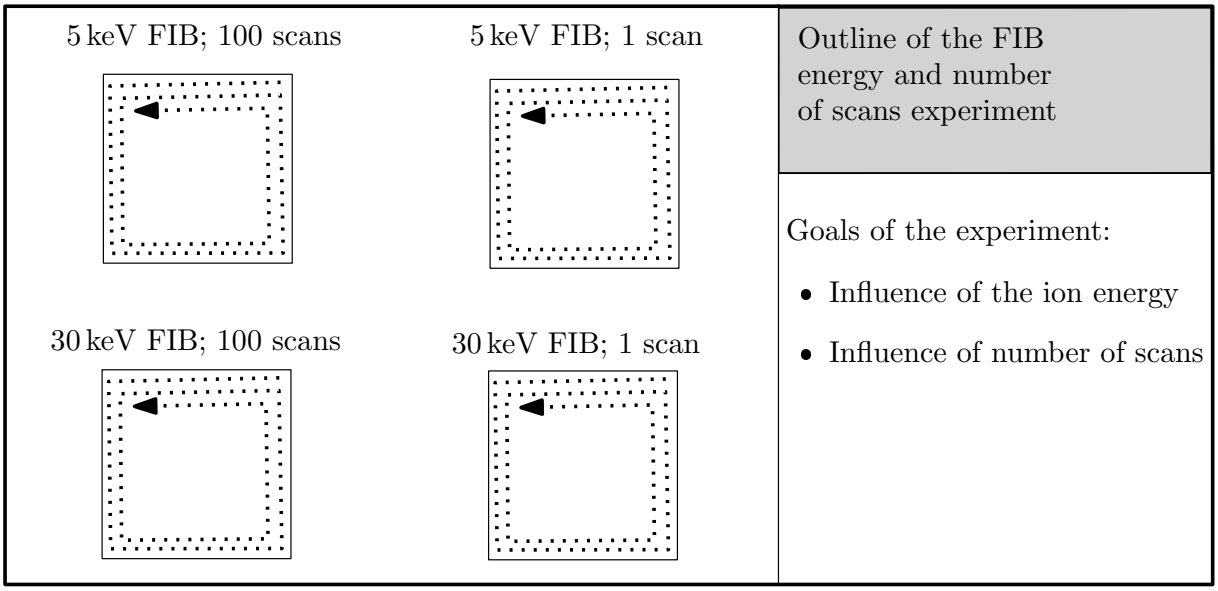

Figure 5.3: An outline of the ion energy and number of scans experiment. Sketch of the analyzed structures with the specified scanning strategy, number of scans, and ion energy.

5.3.1. Motivation of the experiment

From the previous investigations, the influence of the number of scans to magnetic anisotropy was already reported [4], [43]. However, the explanation is not known. We have the hypothesis that this anisotropy behavior can come from different crystallography.

The majority of the previously done FIB transformations were done by 30 keV Ga^+ ions. However, all the crystallographic investigations of the transformed iron-nickel thin film were done by STM after the transformation by the low energetic (4 keV) Ar^+ ions (see the Section 3.2). So far, it was not clear if the ion energy influences the transformation process.

These two inputs inspired the idea to design the presented experiment (see outline in the Figure 5.3).

5.3.2. EBSD measurement

In the Figure 5.4, we presented the orientation IPF maps of four squares fabricated by different FIB energies and number of scans (squares placement is the same as in the

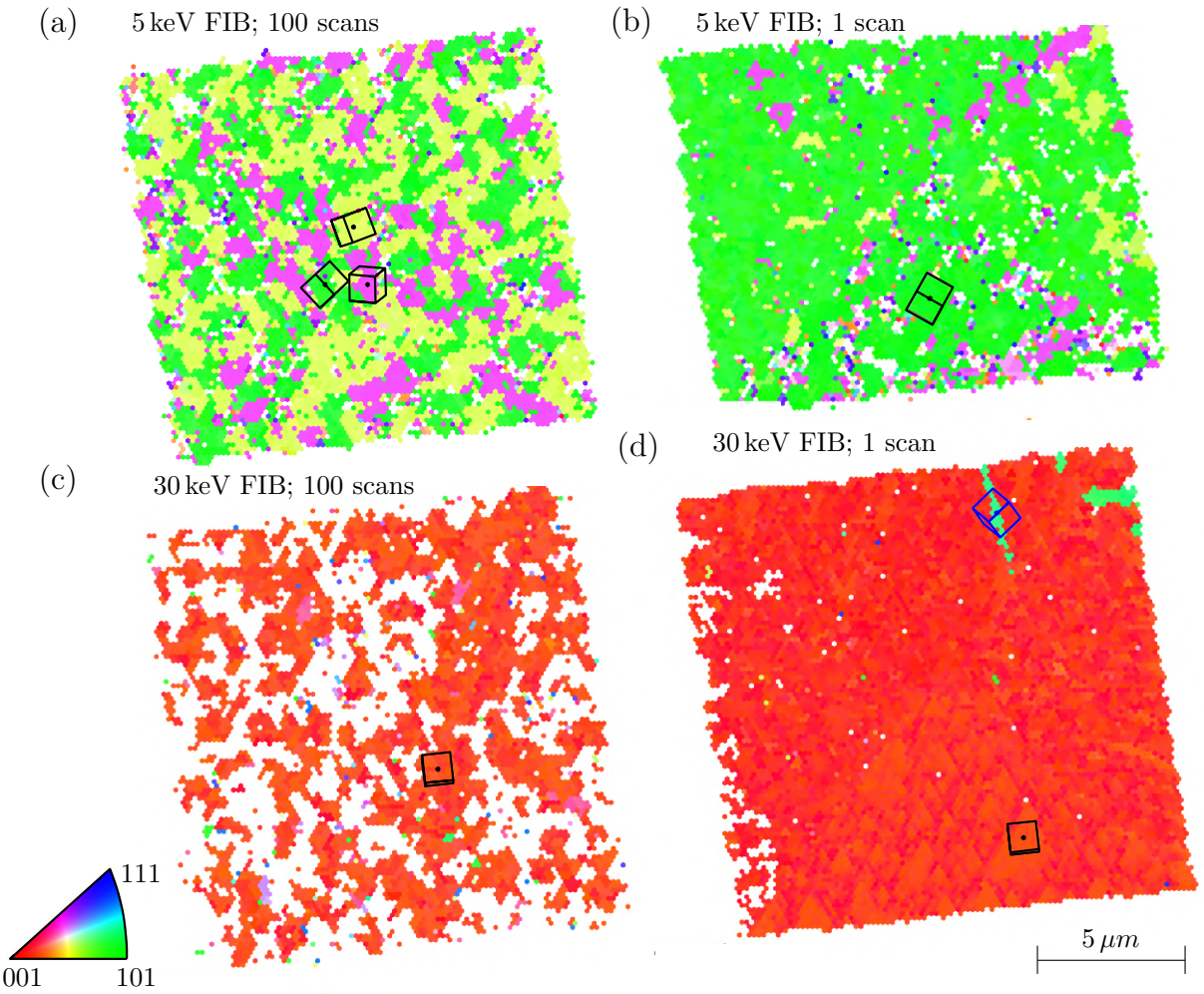

Figure 5.4: IPF map of the squares from *Structures I.* Only bcc pixels are depicted. Characteristic (randomly chosen) pixels are highlighted by schematic crystal lattice unit cell for each square. Parameters used for fabrication the squares: (a) 5 keV FIB, 100 scans; (b) 5 keV FIB, 1 scan; (c) 30 keV FIB, 100 scans; (d) 30 keV FIB, 1 scan.

outline of the experiment). For this purpose, we use the OIM software feature to depict only one phase (bcc in our case). Highlighting by the crystal lattice unit cell turned out to be a great tool for qualitative visualization of the crystal cell orientation.

In the structures fabricated by the ions with the energy of 5 keV [Figure 5.4 (a), (b)], the predominant color is green, what corresponds to the (101) pole from the IPF stereographic triangle. For a single scan, the orientations are much more homogenous than for 100 scans [three dominant poles are highlighted in the subfigure (a)].

For the structures fabricated by the 30 keV ions [Figure 5.4 (c), (d)] we can observe a dominating red color which corresponds to the (001) pole from the IPF stereographic triangle. In the top part of the single scanned square, bcc (101) needles are located. Blue cube in the figure highlights the orientation inside the needle. For 100 scans we observe lots of fcc or not indexed pixels.

By tilting *Structures I.* in the electron microscope, we observed four triangular regions (*bottom, right, top, left*) in the structure fabricated by 30 keV single scan FIB. A similar trend is faintly visible also in the structure fabricated by 5 keV single scan FIB. On the other hand, in the structures fabricated by 100 scans, no similarities were observed. Further details of this analysis are described in the Section A.3. We have the hypothesis that this behavior can be explained by different crystallography in each square. Therefore, we decided to explore the crystallographic ordering in squares more in detail.

In the Figure 5.5 we present such analysis for four regions (*bottom, right, top, left*) of the square fabricated by 30 keV single scan. For this purpose, we cropped the bcc

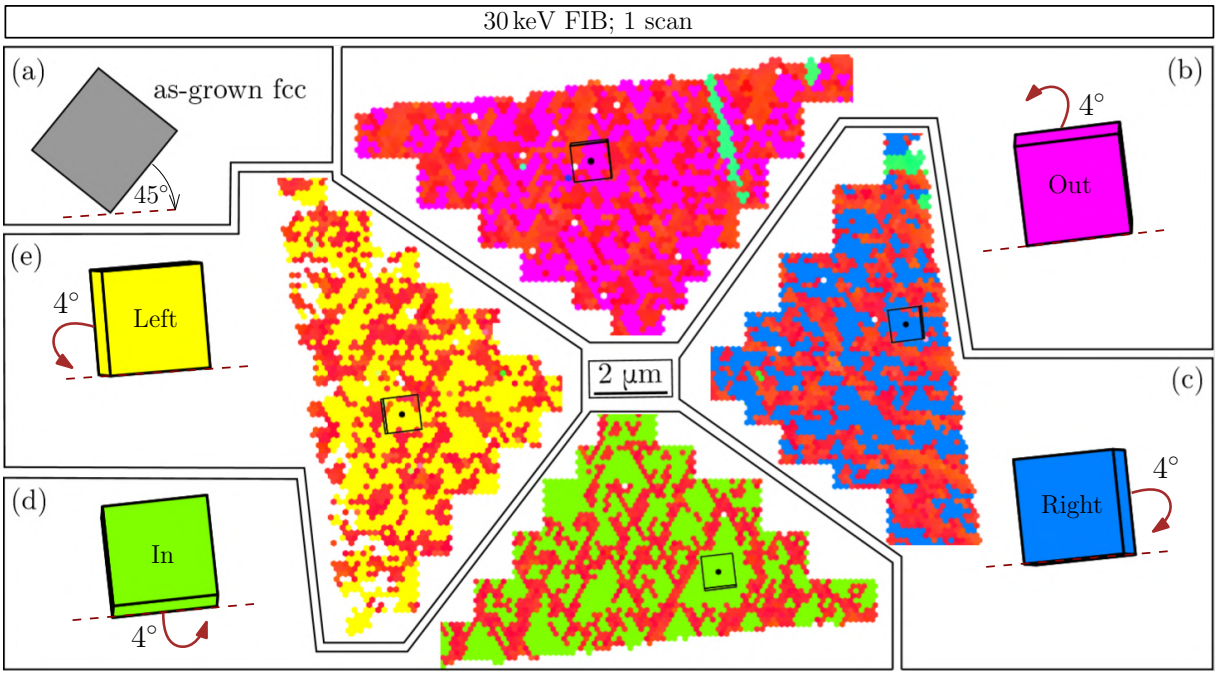

Figure 5.5: Orientation distribution analysis which investigated different orientation domain for each region of the strucutre fabricated by 30 keV single scan FIB. (a) Cubic cell of as-grown fcc measured next to the analyzed square. In-plane misorientation 45° from the bcc cube is marked by black arrow. (b) – (d) subfigures consists of the representative of the prevailing orientation domain and cropped IPF map with the color highlighting of the pixels with misorientation lower then 2.1° from the reference orientation. Reference orientations are mentioned in the Table B.1 in the Appendix. Brown arrows mark out-of plane rotation of the bcc domains.

data in the shapes of these regions (four triangular images in the middle of the Figure 5.5). For each of the regions, we found a different predominant orientation domain. In the Figure 5.5, these are shown as big cubes of a different colors. They differ in the face tilted out-of-plane. Therefore, we refer to them as *in, out, left, right* domain. To get a better insight into their distributions, we employ cumulative *Crystal orientation charts*. For each region, we define predominant orientation as a reference orientation and use it as an input for the charts. In the Figure 5.5, colors (green, yellow, purple, blue) highlight the points with maximum misorientation of 2.1° from the reference orientation of the corresponding region. This value of maximum misorientation retain the same face tilted as in the reference cube. Therefore, we can mark all highlighted points from the region as the same domain. In the Table B.1 in the Appendix, we summarize the data from these charts together with the reference orientations. The minimal representation of the domain in the region is 40%. It happens in the *top* region, which was affected by the presence of a bcc (101) needles [green pixels in the Figure 5.5 (b)].

Using the Euler angles, we looked on the domains mutual orientations more in detail. For this purpose we start from the orientation of the fcc untransformed film [Figure 5.5 (a)]. In the Figure 5.5, both in-plane and out-of-plane rotations from the fcc orientation are demonstrated. All four domains have in-plane misorientation 44° – 46° and out-of-plane tilt 3° – 4° from the fcc. Because the needed rotations during the fcc/bcc transformations are the same, all domains are energetically equivalent. The resulting domains depend only on the FIB scanning strategy and impurities and dislocations in the film.

Then we performed a similar orientation distribution analysis for the structure fabricated by single scan FIB with energy of 5 keV. We cropped the dataset to the same triangular regions (see the center of the Figure 5.6). As can been seen in the Figure 5.6,

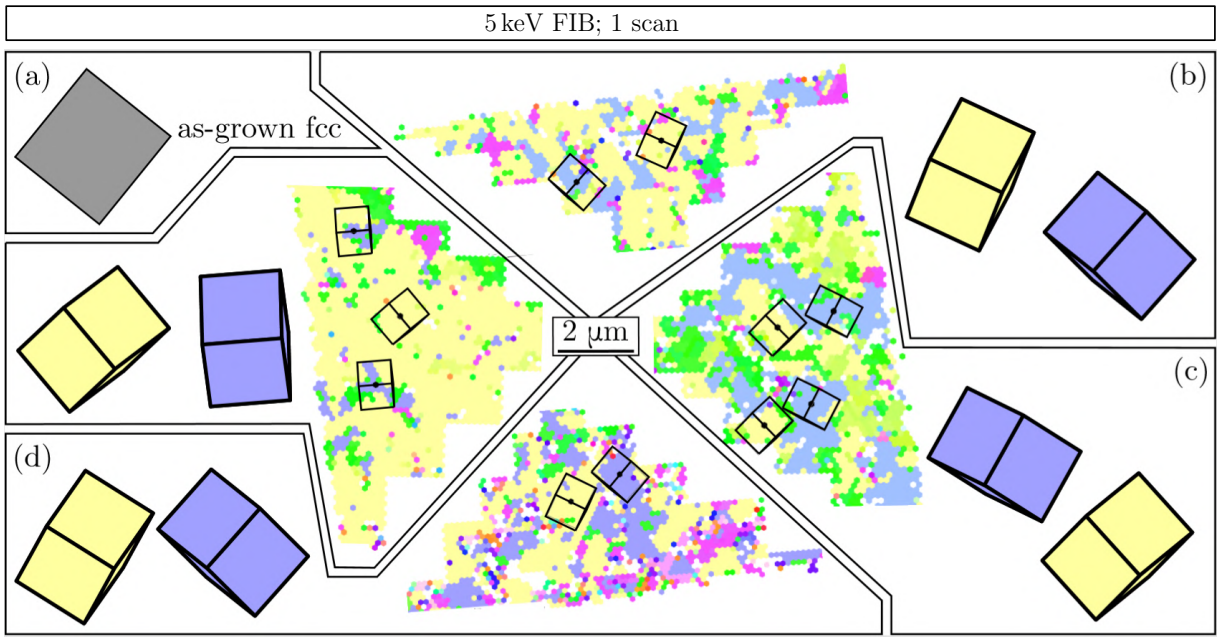

Figure 5.6: Orientation distribution analysis for each region of the strucutre fabricated by 5 keV single scan FIB. Each subfigure consists of the representatives of the two prevailing orientation domains and IPF map with the yellow (misorientation lower then 2°) and lightblue [misorientation from the reference 54° (*left* region) or 60° (*top, right, bottom* region)] highlighting of the pixels. Reference orientations with their corresponding percentage presence are mentioned in the Table B.2.

the situation is more complicated than in the case of structure prepared by a single scan 30 keV FIB. In each region, two predominant domains are present (highlighted by yellow and light blue colors). By the crystal orientation noncumulative chart (it is not handy to use a cumulative chart with two domains in each region) with the reference orientations listed in the Table B.2, prevailing domains are highlighted. In each chart, we highlighted two biggest peaks with the angular width of 1.5°. In the Table B.2, we summarized the results of this analysis. Domains in this table are named by colors used in the Figure 5.6. Orientation distribution is not so clear as in the case of 30 keV FIB single scanned structure. No clear dependence on the FIB scanning direction is visible.

Similar crystallographic domains as in single scanned structures were observed also in the structures irradiated by 100 scans. Nevertheless, their distribution is random. This is consistent with the idea of the stochastic transformation process during the 100 scans irradiation, which we presented in the Section 3.3.

5.3.3. Summary of the experiment

This experiment has showed the different crystallography arrangements for structures transformed by ions with the energy of 30 keV and 5 keV. For low energetic Ga^+ ions, we observed dominating (101) poles [green color in IPF maps in the Figure 5.4(a), (b)]. Whereas the structures transformed by 30 keV have dominating (001) pole [red color in IPF maps in the Figure 5.4(c), (d)].

The second outcome of this experiment is the different distribution of domains in the structures scanned by 100 scans and a single scan (with preserved ion dose). By 100 scans, we introduce random distribution of the orientation domains to the system. Compared to that, by single scan transformation, we observed the presence of the predominant domain in four regions defined by diagonals of the square (presented in the Figure 5.5 and 5.6).

5.4. Experiment 2: Influence of the structure shape

In this experiment, we want to investigate the impact of the shape of the fabricated structures on the crystallographic ordering. Therefore, we designed the experiment as is sketched in the Figure 5.7. We compare EBSD data of the squared structure from *Structures I.* and the circular structure from *Structures II.* Fabrication parameters of both structures are in detail introduced in the Section A.2.

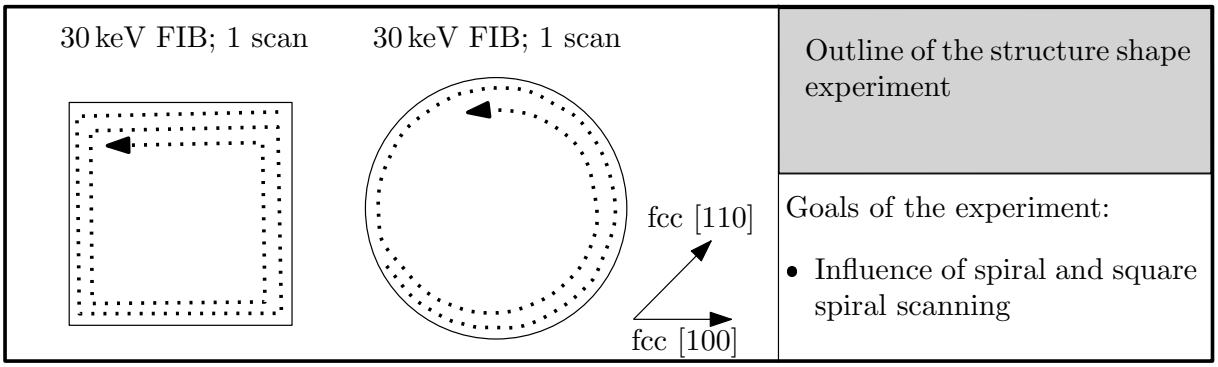

Figure 5.7: An outline of the structure shape experiment. Sketch of the analyzed structures with the specified scanning strategy, number of scans, and ion energy.

5.4.1. Motivation of the experiment

In the previous section, we found the dependence of the crystallographic ordering on the FIB energy and number of scans in squared structures. However, for magnonic structures, various shapes of fabricated structures are needed. Our motivation to investigate the relationship between crystallographic and magnetic properties is to know how these structures serve for spin wave propagation. Therefore, we want to explore whether different structure shape with fixed other parameters affects the crystallography.

5.4.2. EBSD measurement

IPF maps from EBSD measurements of circular and squared structures are presented in the Figure 5.8. At first sight, the same four domains are present in both structures. However, when we compare in-plane misorientation from the as-grown fcc, we realized that in the circular and squared structures, the same domains are in-plane rotated by 13°. This is demonstrated in the Figure 5.8 by the example of *left* domain. Yellow color in the IPF maps highlighted *left* domain as is defined in the Section 5.3.2. Misorientation was extracted from the Euler angles, which are for both case noted in the Figure 5.8. Similar in-plane misorientation was measured for other domains.

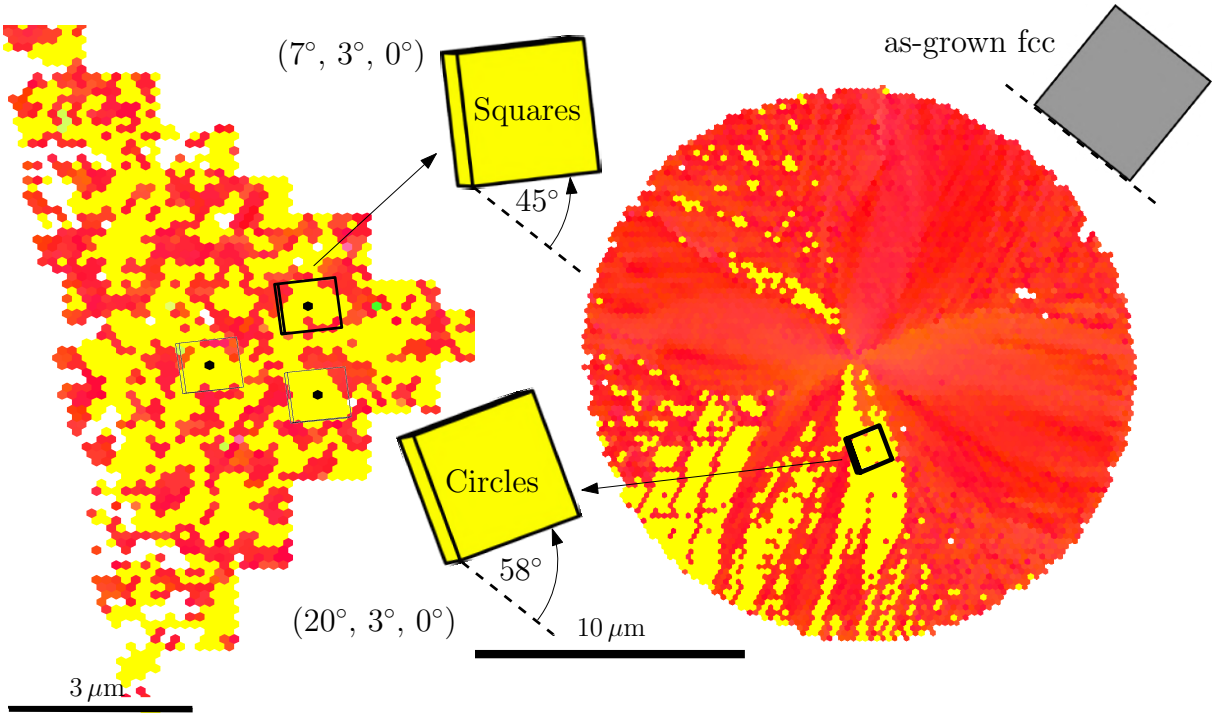

Figure 5.8: Comparison of the *left* domains from the circular and squared structures. Crystal cell with orientation $(20°, 3°, 0°)$ is from circle from *Structures II.* Crystal cell with orientation $(7°, 3°, 0°)$ is from square from *Structures I.* Both analyzed structures were fabricated by single 30 keV FIB. Yellow color in the IPF maps highlights the left domains. Grey square represents as-grown fcc cell. This cell is taken as a reference and in-plane misorientations is marked in the figure.

5.4.3. Summary of the experiment

This experiment showed the same orientation domains defined by the cubic face tilted out-of-plane (*left, right, in, out*) in the squared and circular structures. From the subsequent analysis, we concluded that the same domain from squares and circles differ in in-plane rotation by 13°. That most likely originates from the different scanning direction of these structures.

5.5. Experiment 3: Influence of the concentricity of scanning

Another changeable parameter in the FIB scanning is the direction of the concentricity of the scanning (inside-out or outside-in). In this experiment, we want to investigate the impact of this parameter on the resulting structures. Therefore, we designed the experiment as is sketched in the Figure 5.9. We use EBSD data of an array of circles from *Structures II.* for this analysis. More details about these strucutres can be found in Appendix [see the Section A.2 and the Figure A.4 (b)].

5.5.1. Motivation of the experiment

Concentricity of the beam scanning is another parameter that can affect the properties of the fabricated structures. During the fabrication of *Structures II.* we observed different SEM contrast for circles scanned by opposite concentricity. Partition to the four 90° quadrant can be seen in the cases of the inside-out scanning (see Figure A.7 in Appendix). Moreover, we recognize the so-called *tree texture* in these circles (more details can be found in the Section A.2). Nothing similar was observed for the outside-in scanning. To understand this difference, we performed this experiment.

5.5.2. EBSD measurement

From the EBSD measurement of *Structures II.* we realized that IPF character of the transformed area are qualitatively same (prevailing (001) poles – shades of red in the IPF map) as in squares fabricated by single 30 keV FIB from *Structures I.* Also same orientation domains as in the previous experiments were present. To find the influence

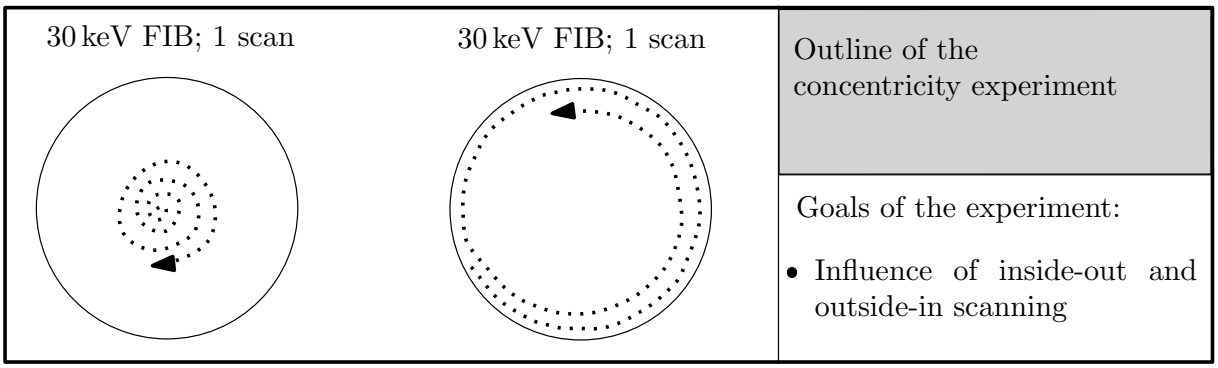

Figure 5.9: An outline of the concentricity of scanning experiment. Sketch of the analyzed structures with the specified scanning strategy, number of scans, and ion energy.

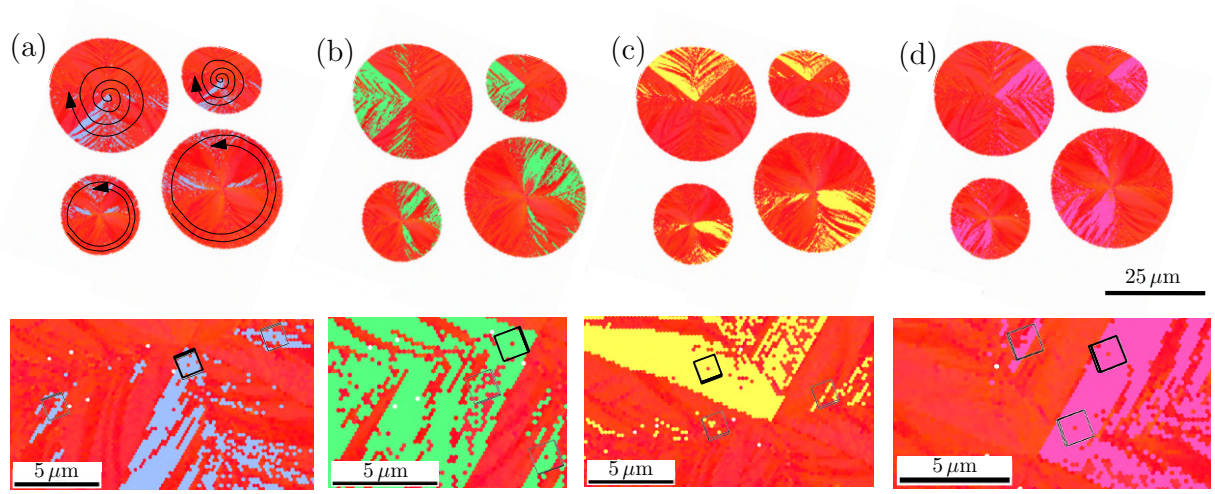

Figure 5.10: Orientation domain analysis of circles scanned inside-out (top row of circles) and outside-in (bottom row of circles). Scanning concentricity is marked in the subfigure (a). Four different domains are highlighted by different colors. Highlighted points have maximum misorientation 2° from the reference orientation. The bottom row shows details from the bigger circle scanned inside-out. (a) *Out domain* with reference orientation $(313°, 4°, 338°)$. (b) *Right domain* with reference orientation $(20°, 94°, 180°)$. (c) *In domain* with reference orientation $(110°, 95°, 271°)$. (d) *Left domain* with reference orientation $(20°, 87°, 180°)$.

of the scanning concentricity on the domains distibution, we performed the orientation distribution analysis. The result of this analysis is presented in the Figure 5.10. In each subfigure, one domain (*out, right, in, left*) with maximum misorientation angles of 2° is highlighted. This analysis clearly showed that the origin of the different SEM contrast of four quadrants in the inside-out circles is crystallographic because in each quadrant, a different domain type is dominant.

Other engaging finding came out from the comparison of the inside-out and outside-in scanned circles. From the color highlighting in the Figure 5.10, we can see that the same domain is on the opposite side of the circle in the case of inside-out and outside-out FIB scanning. For example *In* domain dominates in the top quadrant of inside-out scanned circles and in the bottom part of outside-in scanned circles. Similar reversed behavior can also be observed for the other domains. Because all the other parameters are the same, the origin of this behavior must be in the scanning concentricity.

When we focused more in detail into the domain distribution, we realized that *tree texture* is formed by dominant domains from the adjacent regions (e. g. in the *left* region the *tree texture* is formed by *in* domain and *out* domain). We can conclude that observed *tree texture* contrast has origin in domains distribution.

5.5.3. Summary of the experiment

This experiment dealt with the influence of concentricity of scanning on the crystallographic ordering. Figure 5.11 summarized the distribution of the domains in the analyzed structures. For inside-out scanning, faces of the cubes point to the center. On the other hand, with outside-in scanning, we obtained the cube faces pointing away from the circle center. The same behavior of domains pointing inside or outside of the structure was also observed for the squares (different EBSD measurement).

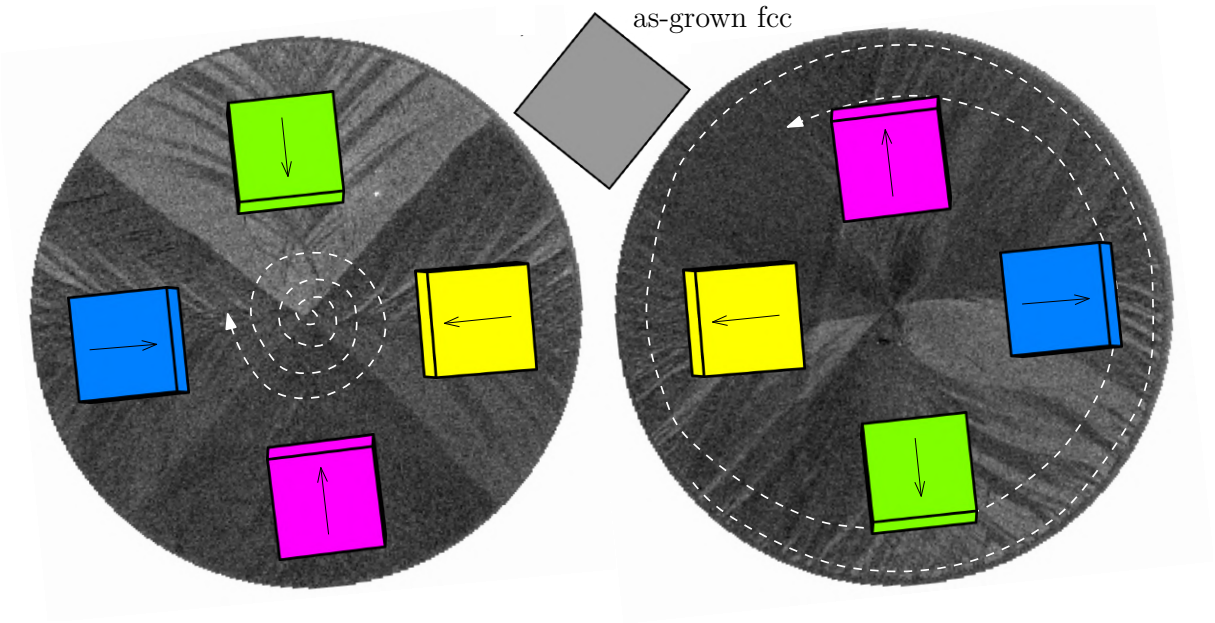

Figure 5.11: Two circles analyzed in the concentricity experiment. White dashed lines mark the inside-out and outside-in scanning. Different distributions for equivalent orientation domains is demonstrated for different concentricity by color cubes. For inside-out scanning, tilted faces point to the center. For outside-in scanning, tilted faces point out from the circle. Grey cube represent as-grown fcc sourandings.

The second finding shows the influence of concentricity to the homogeneity of domains distribution. We observe the creation of four 90° homogenous quadrants (with *tree texture*) for inside-out scanning. Meanwhile, for outside-in scanning, the domain distribution is much less homogenous.

5.6. Experiment 4: Influence of the sense and starting direction of scanning

In the following experiment, we investigate the role of sense (clockwise or counterclockwise) and starting direction of FIB scanning to crystallographic ordering. For this purpose, we measured EBSD on five circles with a different combination of scanning sense and starting scan direction from the *Structures III.* SEM image of these structures, which parameters are described in the subsection A.2, is in the Figure A.5 (a). The design of the experiment is sketched in the Figure 5.12.

5.6.1. Motivation of the experiment

In the previous experiment, we explored the formation of four 90° quadrants observable also in the SEM contrast for the case of inside-out scanning (see Section 5.5). It is not clear if this behavior is caused only by scanning concentricity, or whether other FIB parameters play a role, too. It is also possible that an electron microscope scanning mechanism somehow affects the position of these quadrants. Therefore, we design the experiment with a clockwise and counterclockwise sense of scanning. Alternating starting

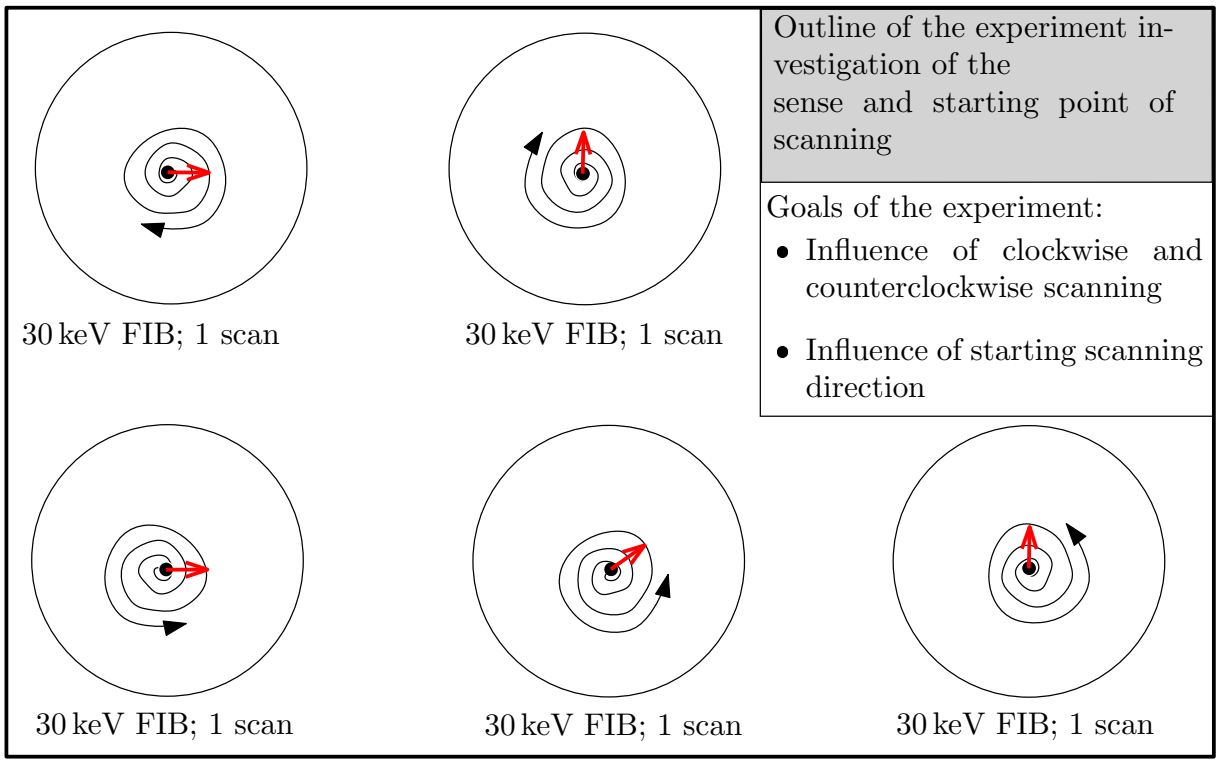

Figure 5.12: An outline of the experiment probing the influence of sense and starting direction of scanning. Sketch of the analyzed structures with the specified scanning strategy, number of scans, and ion energy. Black circular lines mark the sence of scanning (clockwise and counterclockwise). Red arrows mark the starting direction of scanning.

direction of scanning (the direction where the ion beam goes from the center) is equivalent to the sample rotation. It can show if some artifacts of scanning cause the position of quadrants.

5.6.2. EBSD measurement

We want to characterize the influence of alternating parameters of this experiment on the distribution of domains in circles fabricated by a different combination of these parameters (defined in the Figure 5.12). Therefore, we employed crystal orientation charts and performed domain distribution analysis. Its qualitative result is presented in the

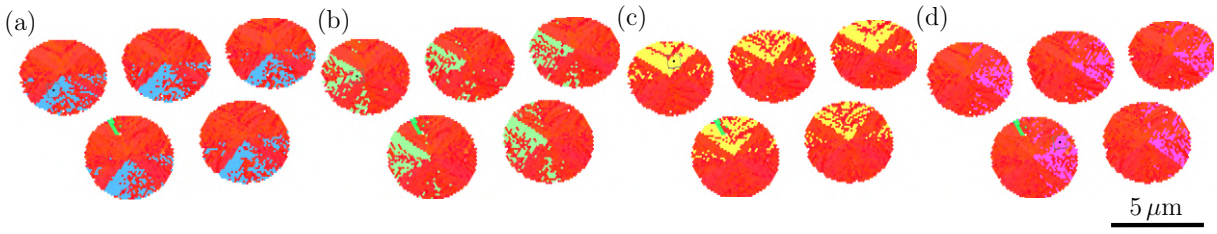

Figure 5.13: Domains distribution analysis of *Structures III*. Same color code as in the Figure 5.10 is used. Highlighted pixels have misorientations lower then 1.8° from the reference orientations. (a) *out* domain, (b) *right* domain, (c) *in* domain, (d) *left* domain. Scanning parameters for each square are defined in the Figure A.5.

Figure 5.13. We used the same color code for the domains (*out, right, in, left*) as in the analysis performed in the Figure 5.10. The maximum misorientation for highlighted pixels is 1.8°.

By evaluating the Figure 5.13, we realize that the distribution of the domains is similar (same predominant domains in the quadrants) in all circles independently of FIB parameters. Hence, we can conclude that the origin of the domain distribution is in the concentricity of scanning.

5.6.3. Summary of the experiment

This experiment shows that the sense and starting direction of scanning have no influence on the distribution of domains in the structures. From this we deduce that the origin of four homogeneous quadrants is in inside-out FIB scanning.

5.7. Experiment 5: Influence of the direction of the fast scanning axis

In this experiment, we want to investigate the influence of the fast scanning axis direction – the direction of one scanning line during structure writing. For this purpose, we compare EBSD data from the squares mutually rotated by 45° from *Structures III.* The design of the experiment is sketched in the Figure 5.14.

5.7.1. Motivation of the experiment

Flajšman already reported about the influence of scanning direction on the properties of the patterned structures. Specifically, it was different SEM contrast and direction of magnetic anisotropy [43]. We have a hypothesis that this difference can come from different crystallography.

Moreover, in the SEM image (see Figure A.7) of the tilted sample we observed eight homogenous triangular areas in the 45° rotated square. Therefore, the EBSD measurement of two squares from *Structures III.* are analyzed in more detail.

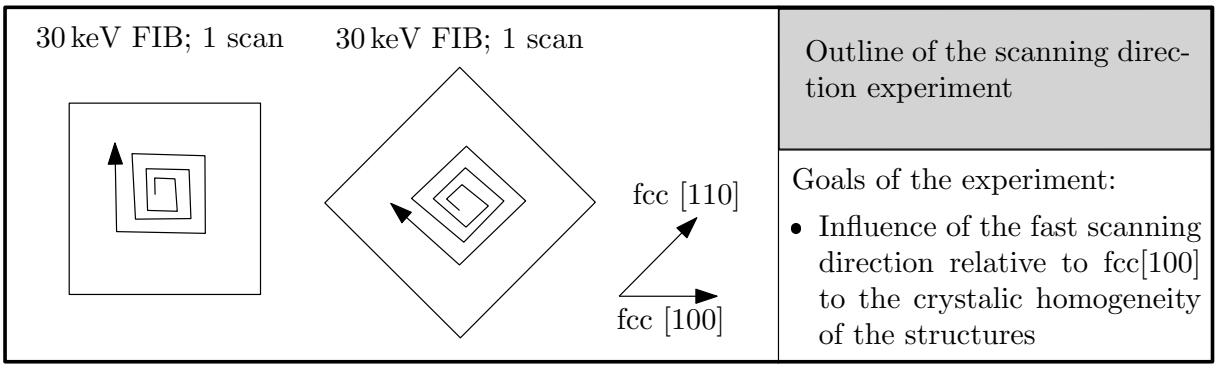

Figure 5.14: An outline of the experiment probing the influence of the direction of fast scanning axis to the homogeneity of the transformed structure. Sketch of the analyzed structures with the specified scanning strategy, number of scans, and ion energy.

5.7.2. EBSD measurement

First of all, we want to compare the homogeneity of the regions in the squares rotated by 0° (fast scanning axis orientation [100]) and 45° (fast scanning axis orientation [110]). We chose one region in each square and made the reference orientation from the predominant domains from these regions. In the Figure 5.15 (a), misorientations from the *out domain* from the bottom triangular region are highlighted. Different colors mark different misorientation intervals with an angular width of 2°. The maximum misorientation for each color interval is in the legend. In the analyzed bottom region, we can find all colors (misorientation from each interval). Therefore, we can say that this region is quite inhomogeneous. By comparison with the SEM image (see Figure A.7), we can determine the correlation between SEM contrast and orientation misorientation. A different story takes place in the subfigure (b). In each region, color highlights the pixels with the maximum misorientation of 1.5° from the reference orientation. We can see, that the vast majority of the pixels from regions have this misorientation. By comparing the subfigures (a) and (b), we can proclaim that the regions in the square rotated by 45° from [100] direction (fast scanning axis orientation [110]) are much more homogeneous than in 0° rotated square.

In next step we portrayed domains for each of eight triangular regions [see cubes in the Figure 5.15 (b)] in the square scanned with fast scanning axis along [110] direction.

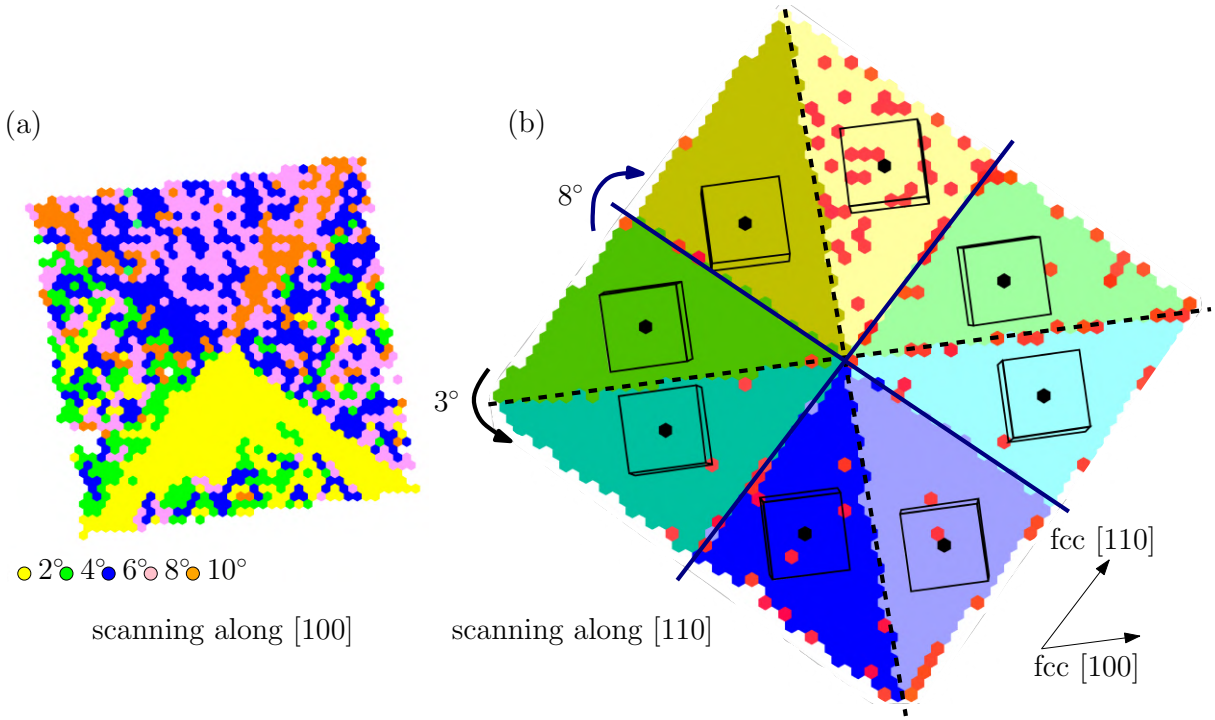

Figure 5.15: The domain analysis of two squares mutually rotated by 45°. (a) Horizontally aligned square from the *Structures III.* for the comparison of homogeneity. Misorientations from the reference *out* domain orientation $(187°, 90°, 87°)$, are highlighted. Different colors mark different misorientation intervals with an angular width of 2°. The maximum misorientation for each color interval is in the legend. (b) Test of the orientation homogeneity. For each of eight triangular regions, by color are highlighted the pixels with maximum misorientation of 1.5°. Blue and black lines are two different types of rotation axes. By rotation around these axes is possible to transform cubic cell from one domain to the neighboring one.

Each domain is defined by two tilted faces. One of these tilts is higher (approx. 5°) and second supplementary (approx. 2°). By the combination of these tilts, eight unique combinations were obtained. We investigate the relationships between the neighboring domains. From the observing of domains Euler angles, it came out that the domains are axially symmetrical around the black dotted and navy solid axes marked in the figure. Rotation by approx. 3° is needed around the black axis. The misorientations between the regions separated by the navy axes are approx. 8°.

5.7.3. Summary of the experiment

In this experiment, we investigated the strong influence of scanning direction on the orientation homogeneity. In the squared structure aligned with the [110] direction, we found eight different orientation domains. These domains are located in eight homogenous triangular region (misorientation maximally 1.5°). We also reported misorientation between neighboring domains regions.

5.8. Perspectives of the orientation analysis

In the previous sections, we analyzed orientation domains in various structures. The main tool for these analyses was *Crystal orientation chart* provided by OIM software. However, for some tasks, it is not the ideal tool. For example, the same orientations are expressed by different equivalent sets of Euler angles, as discussed in the Section 2.1.3. Therefore, we performed some pioneering analysis in the MTEX software (already mentioned in the Section 2.2.4). This software offers lots of functions for crystallographic data analysis. One of them is able to transfer Euler angles to the fundamental region (each orientation has only one representation in the Euler space). Another interesting tool is the rendering of orientation data in the 3D Euler space graph. This, combined with the transfer to the fundamental region, allows us to represent the ratio of the different domains in some region. In the future, we plan to explore the MTEX software options in detail.

5.9. XRD measurements

As was already mentioned in the subsection A.2, we planned to execute the XRD measurement to have a complementary measurement to EBSD. Our goal was to observe some differences in the spectra measured in the structures fabricated with different scanning directions. The spot size of the X-ray beam of this machine is 50 μm. From the discussion with guarantor of the X-ray difractometer, it turned out that dimensions of the structures can be even smaller. Therefore we fabricated two circles with 30 μm diameters with scanning directions perpendicular to [100] direction and rotated by 45° [see Figure A.6 (a), (b)] at 12 nm $Fe_{78}Ni_{22}$ film on Cu#16. However, no signal was observed in the peak originating from bcc lattice. To increase the bcc material volume, we prepared structures with larger diameters of 50 μm, 70 μm and 100 μm [see Figure A.6 (c)]. Nevertheless, no signal appeared even for the biggest circle. Rigaku diffractometer was constructed for analysis of whole films. A simple optical microscope for navigation is therefore a part of the diffractometer. The contrast in this microscope is different from the electron microscope contrast. Therefore, one can not be really sure if the measured area overlayed with the bcc structure. Therefore, we come with the idea to fabricate a new structure (not

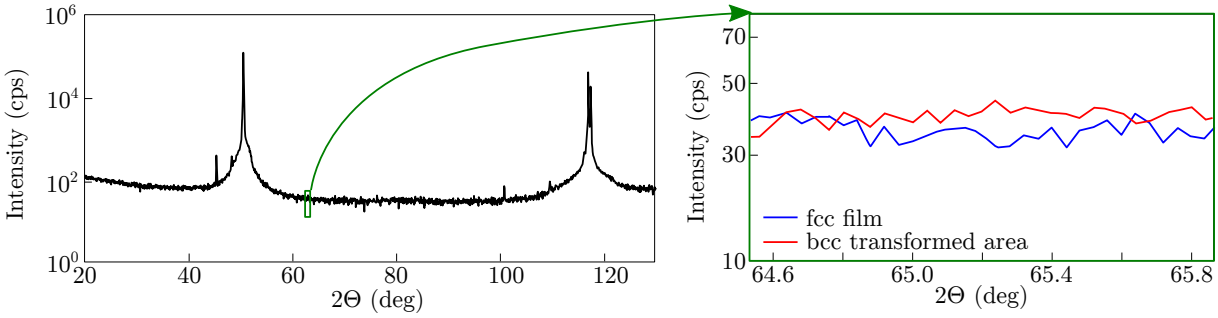

Figure 5.16: XRD measurement in 16 nm thick metastable iron film on Cu#15. In the zoomed area, no significant difference is visible between the spectrum measured in the bcc structure and fcc film. 65° is a position of presumed bcc peak.

present in the Figure) in some exact distance from some characteristic body visible in both microscopes. Unfortunately, this measurement was also without success. As a last resort, we tried to measure the structure fabricated in the thicker film (16 nm, Cu#15) to have more volume of bcc lattice [see the Figure A.6 (d)]. Regrettably, in this case, we did not detect the bcc signal, too. The data from this measurement are presented in the Figure 5.16.

6. Magnetic experiments

In this chapter we present the magnetic anisotropy analysis done by Kerr microscopy. In the Section 6.1 we describe the typical magnetic anisotropy measurement. In the sections 6.2 and 6.3 we present two analysis done in structures described in the Appendix A. In this work, we do not present the theoretical background of the magnetic anisotropy and magnetic energies. The good theoretical description is given in the doctoral thesis of L. Flajšman [43].

6.1. Magnetic anisotropy mesurement workflow

Different direction of magnetic anisotropy for different FIB scanning angles in the metastable iron system was already investigated [4]. In this work, we want to correlate the direction of magnetic anisotropy with the crystallography information inspected in the previous chapter. Therefore, we have decided to study the angular dependence of the shapes of magnetic hysteresis loops on the crystalographic orientation of the structures in the external magnetic field. For this purpose, we employed the Kerr microscopy measurement. In the analysis, we always save the Kerr image for each external magnetic field value for each angle of the sample. In order to obtain the hysteresis of the individual regions of the structures, one needs to analyze the intensity (measured as a grey level proportional to magnetization) evolution as a function of the external magnetic field. We performed this postprocessing in a Labview software created by L. Flajšman. This program allows us to select multiple areas (regions) and extract the corresponding hysteresis loops at the same time. Because from these measured hysteresis loops it is not possible to extract magneto-optical angles (e. g. Kerr ellipticity), we always normalize obtained intensity to the highest value of the loop. To visualize the magnetic anisotropy dependence on the direction of the external magnetic field, we plotted the data as polar remanent plots (Figures 6.1 – 6.5). In the radial axis we plot the normalized remanent magnetization (average of the absolute values of two values of Kerr signal in the zero magnetic field). In the angular axis is the direction of the applied magnetic field. In our case, 0° corresponds to the magnetic field perpendicular to the horizontal direction in the aligned crystal system ([010] crystallographic direction).

6.2. Influence of FIB energy and number of scans to magnetic anisotropy

In this experiment, we investigate the magnetic anisotropy of four squares fabricated by alternating FIB energy and the number of scans. Fabrication of these structures is described in the Section A.2.

6.2.1. Motivation of the experiment

In the Section 5.3 we reported different crystallographic behavior for the squares from *Structures I.* prepared by different FIB parameters (5 and 30 keV; 1 and 100 scans). By this experiment, we want to investigate their anisotropic magnetic behavior and correlate them with the crystallographic information. Magnetic remanent plots in the systems fabricated by 30 keV, and both 1 and 100 scans were already measured [4], [43] nevertheless the origin of their behavior it is not fully understood. In the case of structures fabricated by 5 keV FIB, it will be the first measurement of the magnetic anisotropy.

6.2.2. Magnetic anisotropy measurement

We performed the Kerr microscopy measurement and subsequent postprocessing as it is described in the Section 6.1. In this measurement, we extracted the hysteresis loops from each triangular quadrant from all four squares from *Structures I.* (see the position of the measuring point in the Figure 6.1 – 6.4).

First, we analyze the Kerr data from the squares fabricated by 100 scans 5 keV (Figure 6.1) and 30 keV (Figure 6.2). In both cases, only weak magnetic anisotropy is observed.

When we look at the polar plots evaluated from the Kerr data measured from the square fabricated by 5 keV single scan FIB (see Figure 6.3), we see the similar shapes of plots for opposite regions, which are scanned in the same scanning direction [regions (1) – (3) and (2) – (4)]. Moreover, they are rotated relative to each other by 90°. Nevertheless,

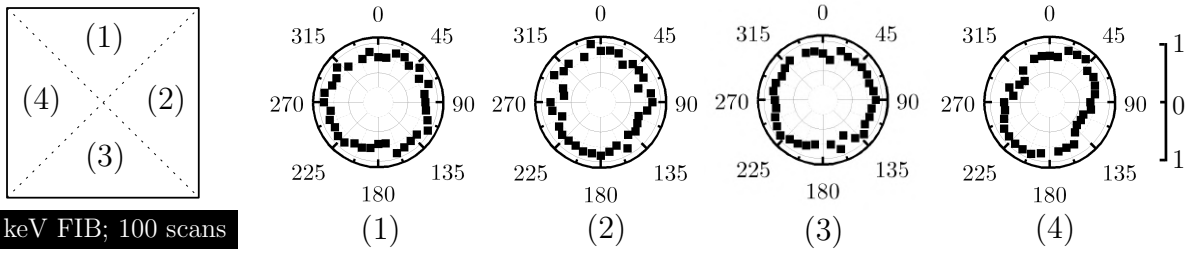

Figure 6.1: Remanent polar plots measured in the rotating magnetic external field. Magnetic signal is extracted from four triangular regions of the square fabricated by 100 scans 5 keV FIB. Remanence in the radial axis is normalized to the maximum value. In the angular axis is a rotation of the magnetic field. 0° corresponds to the filed aligned with [010] crystallographic direction.

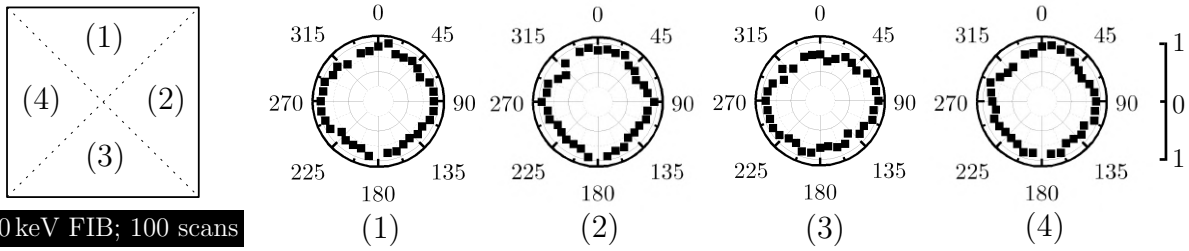

Figure 6.2: Remanent polar plots measured in the rotating magnetic external field. Magnetic signal is extracted from four triangular regions of the square fabricated by 100 scans 30 keV FIB. Remanence in the radial axis is normalized to the maximum value. In the angular axis is a rotation of the magnetic field. 0° corresponds to the filed aligned with [010] crystallographic direction.

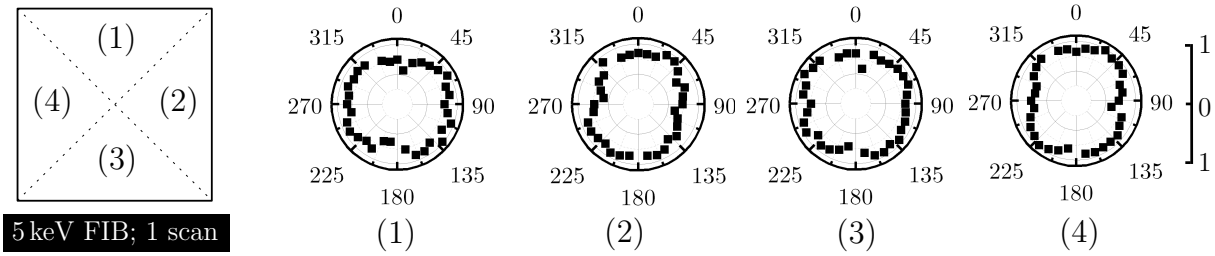

Figure 6.3: Remanent polar plots measured in the rotating magnetic external field. Magnetic signal is extracted from four triangular regions of the square fabricated by single scan 5 keV FIB. Remanence in the radial axis is normalized to the maximum value. In the angular axis is a rotation of the magnetic field. 0° corresponds to the filed aligned with [010] crystallographic direction.

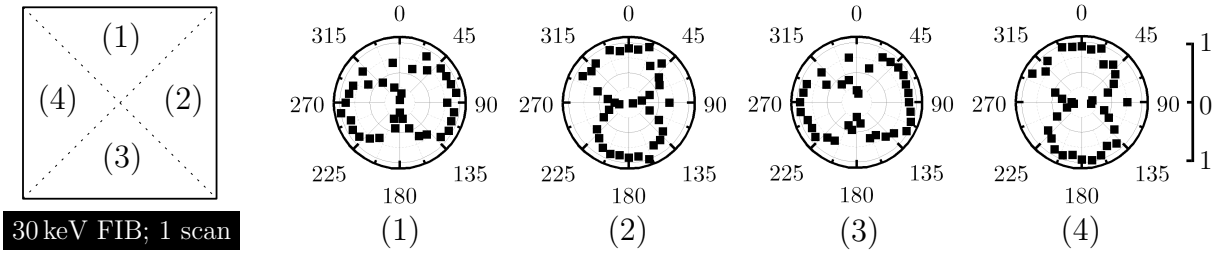

Figure 6.4: Remanent polar plots measured in the rotating magnetic external field. Magnetic signal is extracted from four triangular regions of the square fabricated by single scan 30 keV FIB. Remanence in the radial axis is normalized to the maximum value. In the angular axis is a rotation of the magnetic field. 0° corresponds to the filed aligned with [010] crystallographic direction.

the difference between the maximum and minimum values in each polar graphs is not considerable, and therefore the anisotropic behavior is only weak.

The remanent polar plots from the square fabricated by 30 keV single scan FIB is presented in the Figure 6.4. We can clearly recognize strong uniaxial anisotropy behavior with the same direction of the easy axis for the regions scanned in the same direction.

6.2.3. Summary of the experiment

We measured polar remanent plots for four squares fabricated by a different combination of ion energy and a number of scans from *Structures I.* For squares transformed by 100 scans, we see only weak magnetic anisotropy. On the other hand, by the single scan fabrication, we introduce the anisotropy to the system. This anisotropy is much stronger in the structures fabricated by 30 keV than by 5 keV. The discussion of these results concerning the crystallography of the structures is taking place in the Section 7.1.

6.3. Magnetic anisotropy in homogeneous regions

In this experiment, we want to investigate the magnetic anisotropy of the squared structure rotated by 45° from the [100] horizontal direction. For this purpose, we analyze the big square from *Structures IV.* (for details about the structure see Section A.2).

6.3.1. Motivation of the experiment

In the Section 5.7 we investigated the presence of eight orientation domainsin the 45° rotated square. The goal of this experiment is to explore the influence of this crystallographic ordering on the magnetic anisotropy. EBSD analysis was done on the square from *Structures III.* We decided to execute the Kerr measurement on the bigger square from *Structures IV.*, which is fabricated by the same FIB parameters in order to get a better signal from the eight regions and reduce the effect of region edges.

6.3.2. Magnetic anisotropy measurement

In the Figure 6.5 we present polar remanent plots from eight triangular regions (mark in the left part of the figure). In the plots, all investigated structures show clear uniaxial anisotropy. By comparing the easy axis directions (fitted in the figure) from the graphs, we can distinguish four possible easy axis orientation. As is shown in the Figure 6.5 the same easy axis directions correspond to the regions located symmetrically around the center [e. g. region (5) has same direction as region (1)].

6.3.3. Summary of the experiment

From the Kerr microscopy measurement of square rotated by 45° from [100] crystallographic direction, we could notice magnetic anisotropy behavior with four possible easy axis orientation. The discussion of these results concerning the crystallography of the structure is taking place in the Section 7.2.

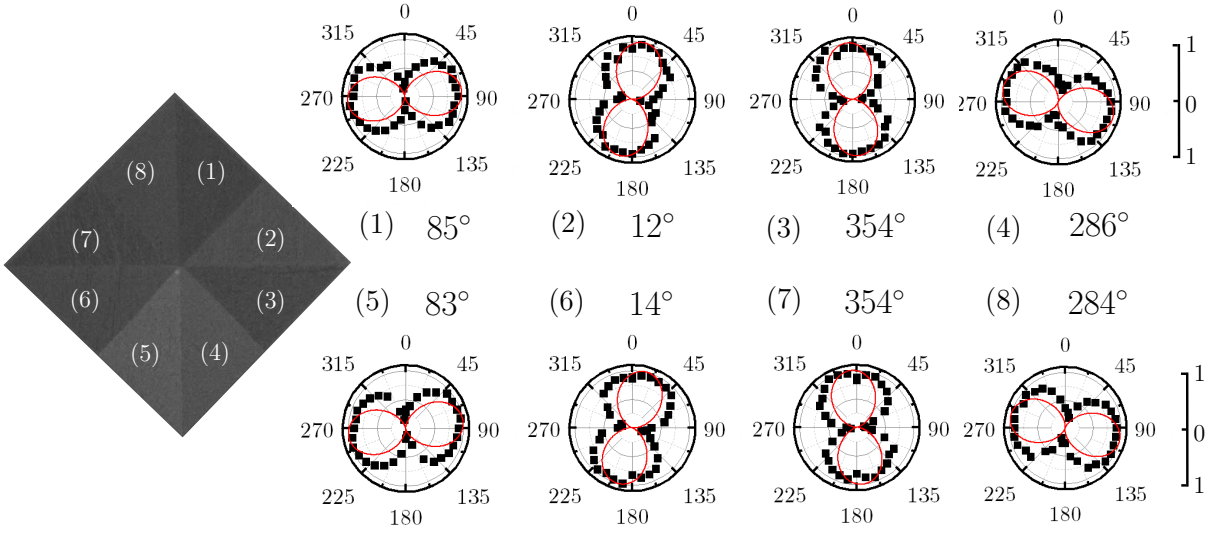

Figure 6.5: Remanent polar plots measured in the rotating magnetic external field. Magnetic signal is extracted from eight triangular regions of the square fabricated by single scan 30 keV FIB. Square is rotated by 45° from the [100] crystallographic direction. Remanence in the radial axis is normalized to the maximum value. In the angular axis is rotation of the magnetic field. 0° corresponds to the filed aligned with [010] crystallographic direction. Plots placed in one column exhibit the same magnetic behavior. By the red lines the easy axis directions are fitted and mentioned for each polar plot.

7. Discussion of the crystallographic and magnetic results

In this chapter, we want to summarize, discuss, and correlate the results from crystallographic (Chapter 5) and magnetic (Chapter 6) measurements. All analyses were done on structures presented in the Appendix A.

7.1. Influence of different transformation number of scans and FIB energy to magnetic and crystallographic properties

In this section, we discuss the measurements done in four squares from *Structures I.* combining different FIB energies (5 keV and 30 keV) and a number of scans (single and 100 scans). Crystallographic experiment is presented in the Section 5.3 and magnetic one in the Section 6.2.

Before this work, it was belived that the transformed metastable iron film is always bcc(110), what is observed by LEED and STM in the films irradiated in-situ by broad Ar^+ beam. By formation of four different bcc(110) orientation domains, the origin of the magnetic anisotropy in the transformed structures were even explained (more details in the Section 3.3). Nevertheless, with EBSD measurement presented in this thesis, we revealed, that the crystallographic system of transformed iron in the structures fabricated by 30 keV Ga^+ FIB is bcc(100). However, bcc(110) systems were found in the structures fabricated by 5 keV FIB. From this, we can conclude that the transformation process is highly dependent on ion energy.

We found different orientation of domains in structures fabricated by both FIB energies (5 keV, 30 keV). In the case of 30 keV single scan, we reported four (or eight in special cofiguration) domains which differ in the cubic face slightly tilted out-of-plane. These tilted faces are parallel with the direction of scanning in the regions. We showed a big influence of the number of scans on the orientation homogeneity in the regions of structures. After the fabrication by 100 scans, the distribution of domains is random. This supports the theory of stochastic bcc nucleation on the impurities. We also tried to unify the measured (110) domains with the expected one from [4] (see the Figure 3.4). We more often observed the misorientation of 60° between two domains. Unfortunately, the misorientations in the expected model were 20°, 90°, and 110°.

When we compare magnetic remanent polar plots with the crystallographic information from the relevant structures, we can proclaim several findings. In both structures fabricated by 100 scans the anisotropic behavior is not present. From the EBSD analyses we know, that these structures have a random distribution of orientation domains. From

this we can conclude, that for the presence of magnetic anisotropy in the fabricated structure, the domains homogeneity is needed. When we compare both structures fabricated by a single scan, we see much lower anisotropy in the structure fabricated by 5 keV. This is caused by the presence of two domains in each region (less homogeneity). However, an occurrence of domains is not totally random and therefore, for the structures fabricated by a single 5 keV scan is magnetic anisotropy higher than for 100 scanned structures.

In the structure with strong magnetic anisotropy (single scan 30 keV FIB), we observed different directions of the easy axis for the regions written by the different directions of the FIB scanning (see Figure 6.4). When we look to the predominant domain in each region (see Figure 5.5), we can conclude that with the magnetic field perpendicular to the out-of-plane tilted face the measured hysteresis loop has low remanence (hard axis loop). In the configuration with the magnetic field parallel with the tilted face, we measured the hysteresis loop with high remanence (easy axis loop). This finding explains the rotation of the easy axis by 90° in the regions with the different orientation domains.

7.2. Influence of the direction of the fast scanning axis to the magnetic and crystallographic properties

In this section, we discuss the difference between the homogeneity of domains in the squares from *Structures III.* mutually rotated by 45° (Section 5.7). We also discuss the results of Kerr microscopy analysis of the square with the fast scanning axis aligned with [110] crystallographic direction (Section 6.3).

From the comparison of the orientation domain distribution in the Figure 5.15 came out the strong influence of scanning direction on the quality of the transformed film. In the square rotated by 45° from the [100] direction, we observed eight triangular regions with misorientation lower than 2°. This is quite important result because in homogenous structures the spin wave propagation length is increased. In *Structures IV.* we fabricated four squares misaligned by ±5° and ±10° from the 45° rotated square. From the SEM observation, it is visible that with the angular misfit, the homogeneity of the regions is lower (see Figure A.7).

When we compare remanent plots from the 45° rotated square (Figure 6.5) with the horizontally aligned square (Figure 6.4), we can declare, that in the first case the remanent curves are significantly smoother. This can be caused by the high homogeneity of the measured areas.

In the Figure 6.5, four different directions of the easy axis are presented. If we correlate this directions with the orientations of domains in the relevant regions (see Figure 5.15), we can observed similar behavior as was discussed in the Section 7.1 – magnetic field perpendicular to the tilted faces caused the low remanence (hard axes hysteresis loop); magnetic field parallel with tilted faces cause the high remanence (easy axis hysteresis loop). In this case of eight orientation domains, the situation is a little bit more complicated because each domain is defined by two tilted cubic faces (more details in the Section 5.7). However, higher tilt has a bigger influence on the direction of the easy axis (dominant tilted face determines if the easy axis direction will be around 0° or 90°). The slightly tilted faces [dashed lines in the Figure 5.7 (c)] then differentiate the directions of easy axis for the regions with the same main tilted face

7.3. Overview of alternating FIB parameters and its importance to the resulting properties

In the Section 7.1 and the Section 7.2 we already discussed the influence of the FIB energy, a number of scans, and the direction of the fast scanning axis on the crystallographic and magnetic properties of the resulting structures. Here we want to mention other FIB parameters that have some impact on the resulting structure. In the Section 5.4 we showed the influence of the structure shape, and in the Section 5.5 we explored the effect of the concentricity of scanning. On the other hand, in the Section 5.6 no influence of the sense and starting direction of scanning was found. These findings will be useful to keep in mind in the future magnonics structures fabrication.

7.4. XRD measurement perspectives

In the Section 5.9 we presented unsuccessful XRD measurements done at structures described in the Section A.2. To use some of the fabricated structures, we performed EBSD measurement at the structure from the Figure A.6 (a). This measurement showed bcc (110) elongated needles aligned with the direction of scanning in bcc (100) matrices typical for 30 keV FIB. The structures fabricated in the thicker film than 16 nm or analyzing the whole film transformed by broad in-situ ion beam can be the way for future XRD measurements.

8. Conclusion

In this thesis, we present the investigation of the properties of the unique system of metastable $Fe_{78}Ni_{22}$ thin films – material suitable for magnonic applications. We focused on a deep understanding of the influence of UHV conditions during the depositions of metastable films and parameters of the focus ion beam (FIB) irradiation on the crystallographic and magnetic properties of the resulting magnetic structures written into the film. With a better understanding of these properties, we are able to prepare magnonic structures tailored to specific application.

The first three chapters were devoted to the brief introduction to this thesis, the basics of crystallography, and the overview of the metastable iron project. In the Chapter 4, we showed several depositions of metastable films on different suitable substrates. Based on the previous investigation [3], we thought that higher CO backpressure during depositions can stabilize the resulting layer as a stable nontransformable fcc nonmagnetic phase. Nevertheless, in this work we present multiple depositions performed in the range of CO pressure from 4×10^{-11} mbar to 1×10^{-6} mbar, and all of these layers were subsequently transformed by FIB. Based on the follow up analysis, we also reported about the influence of the CO backpressure on the ion dose needed for the successful transformation and on the magnitude of the magnetic anisotropy field (important property for the propagating spin waves).

The most direct and useful findings came from the set of electron back-scatter diffraction (EBSD) measurements performed on the structures prepared by irradiation with alternating FIB parameters. We found links between the FIB parameters, crystallographic ordering of resulting structures, and magnetic anisotropy. We explored the influence of the ion energy on the crystallographic structures of transformed areas. Ions with energy of 5 keV form bcc(110), whilst energy of 30 keV form bcc(100). This is quite unexpected result because, based on the in-situ UHV low energetic ions transformation, it was thought that bcc is always in (110) structure. This assumption was even used to explain the changing direction of the magnetic anisotropy introduced into the structures by FIB [4]. This explanation had to be reviewed with respect to our novel results.

We also studied more in detail the crystallographic orientation of the crystal lattice in the transformed structures. When the structure was fabricated by 30 keV FIB, we observed four crystallographic domains that differed in the out-of-plane tilt of the cubic face by approx. 5° in dependence on the FIB scanning direction. This result explains the changes in the SEM contrast with tilting the sample in the regions written in the different scanning directions. This behavior was observed previously without the explanation [43]. With the knowledge of the crystallographic ordering, we can conclude that the tilt needed to maximize the contrast is the same as the out-of-plane tilt of the crystal lattice. This is caused by aligning the sample with the channeling direction for electrons.

In the Chapter 7 we discussed the connections between crystallography and magnetic anisotropy. We concluded that the strongest magnetic anisotropy is introduced into the

structures fabricated by a single 30 keV FIB scan. This is caused by domain homogeneity in the regions scanned in the same scanning direction. With lower ion energy (5 keV), such a region consists of two domains and a weaker magnetic anisotropy. When we took into account orientation of domains in structures fabricated by 30 keV, we saw that hard axis is perpendicular to the out-of-plane tilted cubic edge. This result is essential to real understanding of the magnetic behavior of our system.

FIB direct writing allow us to tune several parameters of scanning and ion beam. In the Chapter 7 we presented how these parameters influence the crystallography and magnetism of the transformed structures. These results will be taken into account in the future fabrication of magnonic structures. More engaging finding is the key role of the FIB fast scanning axis direction. By aligning this axis with [110] crystallographic direction we obtain the highly homogeneous structures. This is quite interesting for the magnonic waveguide fabrication because high homogeneity caused the high magnetic anisotropy and high spin wave propagation length.

References

[1] A., Chumak, Vasyuchka V., Serga A. and Hillebrands B. Magnon spintronics. *Nature Physics*. 2015. Vol. 11, no. 6, 453–461. Available from: doi:10.1038/nphys3347.

[2] S., Neusser and Grundler D. Magnonics: Spin waves on the nanoscale. *Advanced Materials*. 2009. Vol. 21, no. 28, 2927–2932. Available from: doi:10.1002/adma.200900809.

[3] J., Gloss, Shah Zaman S., Jonner J., Novotny Z., Schmid M., Varga P. and Urbánek M. Ion-beam-induced magnetic and structural phase transformation of Ni-stabilized face-centered-cubic Fe films on Cu (100). *Applied Physics Letters*. 2013. Vol. 103, no. 26, 262405. Available from: doi:10.1063/1.4856775.

[4] URBÁNEK, M., L. FLAJŠMAN, Křižáková V., Gloss J., Horký M., Schmid M. and Varga P. Research Update: Focused ion beam direct writing of magnetic patterns with controlled structural and magnetic properties. *APL Materials*. 2018. Vol. 6, no. 6, 060701. Available from: doi:10.1063/1.5029367.

[5] KITTEL, C. *Introduction to solid state physics*. 8th ed. Wiley, 2005. ISBN 9780471415268.

[6] KŘIŽÁKOVÁ, V. *Magnetic properties of materials based on metastable Fe-Ni films*. 2016. Mater's thesis. Brno Univeristy of Technology.

[7] MATHWORKS. *Rotations, Orientation, and Quaternions* [online]. [Accesed 2020-05-19]. Available from: `https://www.mathworks.com/help/fusion/examples/rotations-orientation-and-quaternions.html`.

[8] WIKIPEDIA. *Rotation formalisms in three dimensions* [online]. [Accesed 2020-05-19]. Available from: `https://en.wikipedia.org/wiki/Rotation_formalisms_in_three_dimensions`.

[9] MAN, O. *Application of electron backscatter diffraction in material engineering*. 2010. PhD thesis. Brno University of Technology.

[10] M., Birkholz. *Thin film analysis by X-ray scattering*. John Wiley & Sons, 2006. ISBN 3527607048.

[11] WIKIPEDIA. *Euler angles* [online]. [Accesed 2020-05-21]. Available from: `https://en.wikipedia.org/wiki/Euler_angles`.

[12] J., Bunge H. *Mathematische Methoden der Texturanalyse: Mit 86 Abbildungen und 31 Tabellen, sowie 7 Abbildungen und 9 Tabellen im Anhang*. Akademie-Verlag, 1969.

[13] O., Engler and Randle V. *Introduction to texture analysis: macrotexture, microtexture, and orientation mapping*. CRC press, 2009.

[14] A., Morawiec. *Orientations and rotations*. Springer, 2003.

[15] *OIM Analysis^{TM} User's Guide*. 2019.

[16] J., Schwartz A., Mukul K., Adams B. L. and Field D. P. *Electron backscatter diffraction in materials science*. Springer, 2009. ISBN 978-0-387-88135-5.

[17] WIKIPEDIA. *Pole figure* [online]. [Accesed 2020-06-04]. Available from: `https://en.wikipedia.org/wiki/Pole_figure`.

[18] GLOSS, J. *Metastable iron-nickel thin films*. 2019. PhD thesis. TU Wien.

[19] HYDRARGYRUM. *Bragg law* [online]. 2011 [Accesed 2020-04-04]. Available from: `https://en.wikipedia.org/wiki/X-ray_crystallography#/media/File:Bragg_diffraction_2.svg`.

[20] S., Nishikawa and Kikuchi S. Diffraction of cathode rays by calcite. *Nature*. 1928. Vol. 122, no. 3080, 726–726. Available from: doi:10.1038/122726a0.

[21] L., Reimer. *Scanning Electron Microscopy*. Springer Berlin, Heidelberg, 1985. ISBN 978-3-540-38967-5.

[22] RANDLE, V. Theoretical framework for electron backscatter diffraction. In: *Electron backscatter diffraction in materials science*. Springer, 2000, p. 19–30. ISBN 978-1-4757-3205-4.

[23] KELLER, RR et al. EBSD measurement of strains in GaAs due to oxidation of buried AlGaAs layers. *Microelectronic engineering*. 2004. Vol. 75, no. 1, 96–102.

[24] KZ., Baba-Kishi. Review Electron backscatter Kikuchi diffraction in the scanning electron microscope for crystallographic analysis. *Journal of materials science*. 2002. Vol. 37, no. 9, 1715–1746.

[25] J., Tarasiuk and Gerber Ph. Bacroix B. Estimation of recrystallized volume fraction from EBSD data. *Acta materialia*. 2002. Vol. 50, no. 6, 1467–1477.

[26] WILKINSON, A. J. Measurement of elastic strains and small lattice rotations using electron back scatter diffraction. *Ultramicroscopy*. 1996. Vol. 62, no. 4, 237–247.

[27] INSTRUMENTS, Oxford. *Diffraction silicon pattern* [online]. [Accesed 2020-06-30]. Available from: `http://www.ebsd.com/10-ebsd-explained`.

[28] *The Hough transform*. [online]. [Accesed 2020-04-17]. Available from: `http://www.tsdconseil.fr/log/opencv/ext/hough/index-en.html`.

[29] HOUGH, P. *Method and means for recognizing complex patterns*. Google Patents, 1962. US Patent 3,069,654.

[30] WRIGHT, S. I. Fundamentals of automated EBSD. In: *Electron backscatter diffraction in materials science*. Springer, 2000, 51–64.

[31] EDAX. *OIM Analysis* [online]. [Accesed 2020-06-10]. Available from: `https://www.edax.com/products/ebsd/oim-analysis`.

[32] R., Hielscher. *MTEX* [online]. [Accesed 2020-06-10]. Available from: `https://mtex-toolbox.github.io/`.

[33] WA., Jesser and Matthews J. WO. Evidence for pseudomorphic growth of iron on copper. *Philosophical Magazine*. 1967. Vol. 15, no. 138, 1097–1106. Available from: doi:10.1080/14786436708222752.

[34] A., Biedermann, Tscheließnig R. Schmid M. and Varga P. Crystallographic Structure of Ultrathin Fe Films on Cu(100). *Phys. Rev. Lett.* [online]. 2001. Vol. 87, 086103. Available from: doi:10.1103/PhysRevLett.87.086103. Available from: `https://link.aps.org/doi/10.1103/PhysRevLett.87.086103`.

[35] W., Rupp, Biedermann A., Kamenik B., Ritter R., Klein CH., Platzgummer E., Schmid M. and Varga P. Ion-beam induced fcc-bcc transition in ultrathin Fe films for ferromagnetic patterning. *Applied Physics Letters*. 2008. Vol. 93, no. 6, 063102.

[36] S., Zaman S., Dvořák P., Ritter R., Buchsbaum A., Stickler D., Oepen H. P., Schmid M. and Varga P. In-situ magnetic nano-patterning of Fe films grown on Cu (100). *Journal of Applied Physics*. 2011. Vol. 110, no. 2, 024309.

[37] A., Biedermann, Tscheliessnig R., Schmid M. and Varga P. Local atomic structure of ultra-thin Fe films grown on Cu (100). *Applied Physics A*. 2004. Vol. 78, no. 6, 807–816. Available from: doi:10.1007/s00339-003-2435-7.

[38] S., Zaman S., Oßmer H., Jonner J., Novotnỳ Z., Buchsbaum A., Schmid M. and Varga P. Ion-beam-induced magnetic transformation of CO-stabilized fcc Fe films on Cu (100). *Physical Review B*. 2010. Vol. 82, no. 23, 235401. Available from: doi:10.1103/PhysRevB.82.235401.

[39] CH., Sandweg, Kajiwara Y., Chumak A., Serga A., Vasyuchka V., Jungfleisch M., Saitoh E. and Hillebrands B. Spin pumping by parametrically excited exchange magnons. *Physical review letters*. 2011. Vol. 106, no. 21, 216601. Available from: doi:10.1103/PhysRevLett.106.216601.

[40] J., Gloss, Horkỳ M., Křižáková V., Flajšman L., Schmid M., Urbánek M. and Varga P. The growth of metastable fcc Fe78Ni22 thin films on H-Si (1 0 0) substrates suitable for focused ion beam direct magnetic patterning. *Applied Surface Science*. 2019. Vol. 469, 747–752. Available from: doi:10.1016/j.apsusc.2018.10.263.

[41] CHANG, C. Outdiffusion of Cu through Au: Comparison of (100) and (111) Cu films epitaxially deposited on Si, and effects of annealing ambients. *Applied physics letters*. 1989. Vol. 55, no. 26, 2754–2756. Available from: doi:10.1063/1.101944.

[42] A., Meunier and Gilles B. Verdier M. Cu/Si (0 0 1) epitaxial growth: role of the epitaxial silicide formation in the structure and the morphology. *Journal of Crystal Growth*. 2005. Vol. 275, no. 1-2, e1059–e1065. Available from: doi:10.1016/j.jcrysgro.2004.11.132.

[43] FLAJŠMAN, L. *Magneto-optical study of the dynamic properties of magnetic nanostructures and nanostructured metamaterials*. 2019. PhD thesis. Brno Univeristy of Technology.

[44] L., Flajšman, Wagner K., Vaňatka M., Gloss J., Křižáková V., Schmid M., Schultheiss H. and Urbánek M. Zero-field propagation of spin waves in waveguides prepared by focused ion beam direct writing. *Physical Review B*. 2020. Vol. 101, no. 1, 014436. Available from: doi:10.1103/PhysRevB.101.014436.

[45] O., Wojewoda, Hula T., Flajšman L., Vaňatka M., Gloss J., Holobrádek J., Staňo M., Stienen S., Körber L., Schultheiß K., Schmid M., Schultheiß M. and Urbánek M. *Propagation of spin waves through a Néel domain wall* [online]. 2020. Available from: https://arxiv.org/abs/2005.05690.

[46] UNIVERSITY, Augsburg. *MWPCVD diamond* [online]. 2014 [Accesed 2019-07-04]. Available from: `www.physik.uni-augsburg.de/exp4/_Research/Diamond/`.

[47] J., Ullmann, Heger P., Pinkert K. and Baba K. Ions as a useful tool for carbon film deposition and modification. *Nuclear Instruments and Methods in Physics Research Section B: Beam Interactions with Materials and Atoms*. 1995. Vol. 106, no. 1-4, 96–105. Available from: doi:10.1016/0168-583X(95)00685-0.

[48] EDAX. *Understanding Electron Backscatter Diffraction (EBSD) Background Corrections* [online]. [Accesed 2020-06-25]. Available from: `https://www.edax.com/-/media/ametekedax/files/resources/tips_tricks/understandingebsdbackground%20corrections.pdf`.

[49] TESCAN. *Electron Channelling Pattern Acquisition on Polycrystalline Materials* [online]. 2015 [Accesed 2020-06-18]. Available from: `http://library.tescan.com/attachments/article/63/AE_151008_TESCAN_electron_channelling_pattern_acquisition_on_polycrystalline_materials_web.pdf`.

List of abbreviations

AES	Auger electron spectroscopy
APPH	average peak-to-peak height
BCC	body centered cubic
BSE	Backscattered electron
BLS	Brillouin light scattering
CI	Confidence index
EBSD	Electron backscatter diffraction
ECP	Electron chanelling pattern
FCC	face centered cubic
FIB	Focus ion beam
IQ	Image quality
IPF	Inverse pole figure
LEED	Low-energy electron diffraction
ML	monolayer
MRAM	Magnetic random access memories
MWPCVD	Microwave plasma chemical vapor deposition
LN_2	Liquid nitrogen
ND	Normal direction
OIM	Orientation mapping
PF	Pole figure
PINUP	Projekt Ionenneutralisation und Ultraviolett-Photoelektronenspektroskopie
QCM	Quartz crystal microbalance
RD	Rolling direction

SC	simple cubic
SEM	Scanning electron microscopy
SE	Secondary electrons
SMOKE	Surface Magneto-Optical Kerr effect
STM	Scanning tunneling microscopy
TD	Transverse direction
TSP	Titanium sublimation pump
UHV	Ultra-high vacuum
WD	Working distance
XRD	X-ray diffraction
YSZ	Yttria-stabilized zirconia

A. Structures fabrication by focus ion beam

In this appendix, we introduce the procedure of FIB fabrication of bcc structures, which are used in experiments in the Chapter 5 and 6. In the Section A.1 we present pseudo-Kikuchi lines as a tool for aligning the sample with the distinguished crystallographic direction before the writing of the structures. This is necessary to control the FIB scanning direction – an essential parameter for the resulting properties of the transformed areas. In the Section A.2 the overview of all structures with their essential properties is given. In the Section A.3 we report the SEM observation of the structures contrast evolution during the tilting of the sample.

A.1. Aligning the sample before the FIB transformation

Flajšman already reported [43] about the presence of the faint patterns [see the Figure A.1 (a)] during the SEM observation of the whole sample with the specific condition (working distance (WD), scanning mode,...). It has been proven that these patterns are so-called electron channeling patterns (ECP) formed from the pseudo-Kikuchi lines [49]. The contrast forming these patterns comes from the different atomic distribution in different directions (from different views), which creates the so-called channels. The sketch of the same crystal observed from different directions is presented in the Figure A.1 (b). When the electron beam is close to the diffraction Bragg condition of the channeling plane, the output signal changes, especially in the backscattered electrons (BSE). Resulting lines in ECP are called pseudo-Kikuchi, because the creation process is quite similar to the process of the Kikuchi pattern creation in the EBSD (see Section 2.2.3). The ECP is a rich source of information about the crystallographic arrangement and sample orientation. It allows precise alignment of the sample directly in the SEM in both the rotation and the tilt. The overlaid pseudo-Kikuchi lines calculated for the fcc Cu(100) in the Figure A.1 (c) match the observed pattern nicely. The red lines come from diffraction on {100} planes, and we typically aligned them horizontally [rotation is indicated by the red arrow in the Figure A.1 (a)] to have a reference direction to FIB scanning direction.

Typically we observed ECP in the Tescan Lyra 3 microscope with low WD ($\sim$4 mm), wide-field scanning mode, small magnification [whole sample displayed in the view field as in the Figure A.1(a)] and primary electron energy of 5 keV. Alternatively, the channeling scanning mode can be employed. In this mode, a thin parallel beam is rocking around a point on the surface. Unfortunately, sometimes it is quite challenging to set up the microscope to display a clear ECP. Therefore, we arranged an assisted session with T. Šamořil

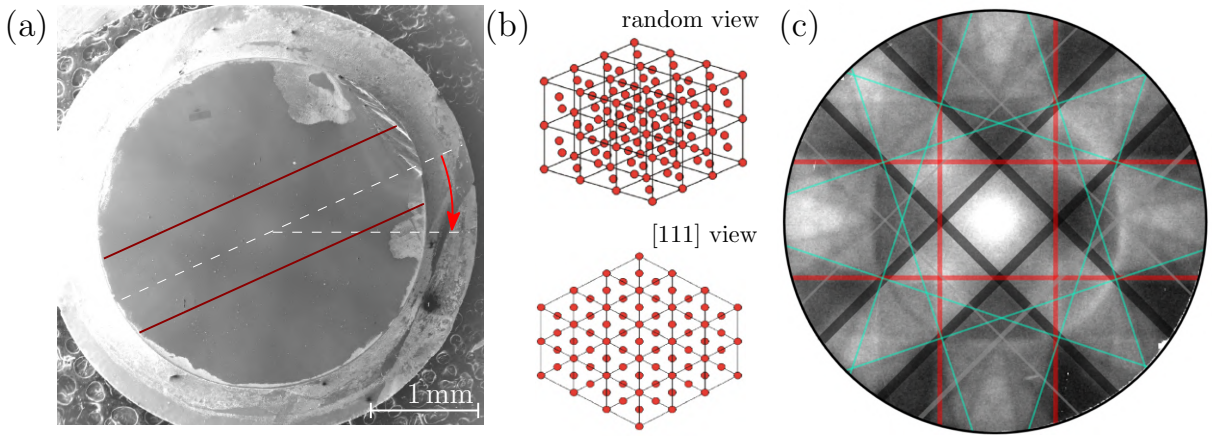

Figure A.1: Electron channeling patterns (ECP) with pseudo-Kikuchi lines. (a) Typically observed pattern on the copper crystal with the 12 nm of the $Fe_{78}Ni_{22}$ film. The red arrow marks the rotation needed to align [100] direction horizontally. (b) The schema of different atomic distribution densities and channels when looking at an fcc crystal lattice from different angles. Adapted from [49]. (c) ECP in WD 3 mm acquired by primary electron energy 5 keV. The image is processed by ImageJ (quadratic background subtraction) and overlaid by four most intensive Kikuchi lines calculated in the KLine software for fcc Cu(100). Red lines correspond with the diffraction on the (200) crystallographic plane. Adapted from [43].

to find the ideal parameters of the microscope to reveal the optimal ECP. The most significant improvement comes with higher electron energy (20 keV). With this energy, it is not necessary to use low WD because already the conventional WD of 9 mm provides bright enough ECP. Another emendation comes with a retractable BSE detector [normally, the detector of secondary electrons (SE) is used]. ECPs acquired at the same sample (Cu #16 with 12 nm $Fe_{78}Ni_{22}$) are presented in the Figure A.2 (a) wide field scanning mode, SE detector, (b) channeling scanning mode, SE detector, (c) channeling scanning mode, BSE detector. We also tried to gain ECP from the different systems used in the metastable iron project. Regrettably, even with tunning the parameters, we were not able to get the ECP from pure copper crystal and silicon substrate with the metastable iron-nickel film. It was most likely caused by little changes in the crystal lattice that broke the Bragg diffraction condition or by impurites and dislocations. On the other hand, we were successful with pure silicon sample. This ECP is presented in the Figure A.2 (d) (WD 9 mm, wide field scanning mode, SE detector). We also tried to display the ECP from the transformed area in channeling scanning mode. Unfortunately, no difference in the pseudo-Kikuchi lines was observed. Most likely, it is because of too thin bcc film and contribution from the copper substrate.

A.2. Structures fabrication

After the sample aligning, FIB tuning takes place. Fixed parameters for structures fabrication are ion beam pitch 10 nm (1/3 of spot diameter), and ion beam current approx. 160 pA (depends on setting of the lenses and selected FIB aperture and its working time). To determine the high enough ion dose for fcc/bcc transformation, we performed the so-

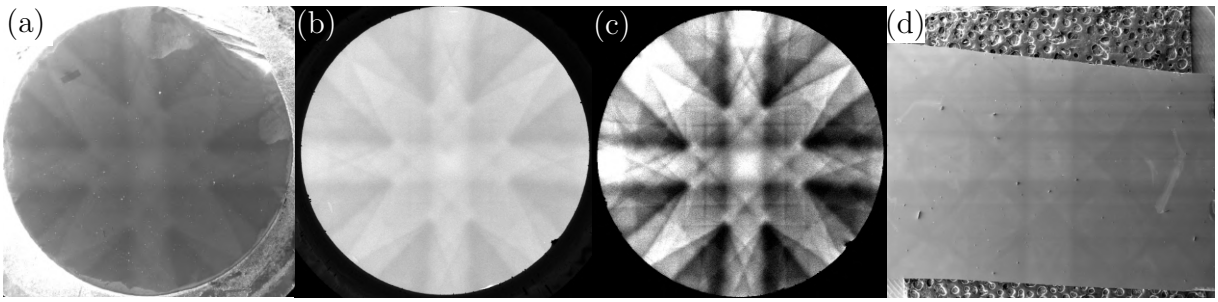

Figure A.2: ECPs acquired during the optimization of the microscope parameters. Cu#16 with 12 nm $Fe_{78}Ni_{22}$ imaged at WD 9 mm with 20 keV electron beam by (a) wide field scanning mode and SE detector, (b) channeling scanning mode and SE detector, (c) channeling scanning mode and BSE detector. (d) Silicon crystal without the metastable film imaged at WD 9 mm with 5 keV electron beam by the wide field scanning mode and SE detector.

called dose test. It consists of an array of squares with increasing ion dose. It differs in the parameter called *Exp factor*, which affects the time spent by ion beam in one spot. Such dose tests are presented in the Figure A.3. The contrast observation determines the optimally transformed structure (higher ion doses cause the sputtering of the film). Required structures are consequently fabricated with the *Exp factor* of this chosen structure.

We fabricated a couple of structures for crystallographic and magnetic characterization presented in this thesis. First experiments were done in *Structures I.* [see Figure A.4 (a)] – four $15\times15\,(\mu m)^2$ squares combining two FIB energies (5 keV, 30 keV) with two numbers of scans (single scan, 100 scans). The idea behind these experiments is to probe how these parameters influence the crystallography of the transformed area. It was already observed without any explanation by L. Flajšman that in areas transformed by 100 scans no magnetic anisotropy is present. Also different transformation behavior in SEM for structures transformed by single scan and 100 scans were reported [4]. The rest of the experiments were done for fixed FIB energy – 30 keV and number of scans – 1, and we varied only the structures shapes, dimensions, crystallographic orientations and scanning strategy.

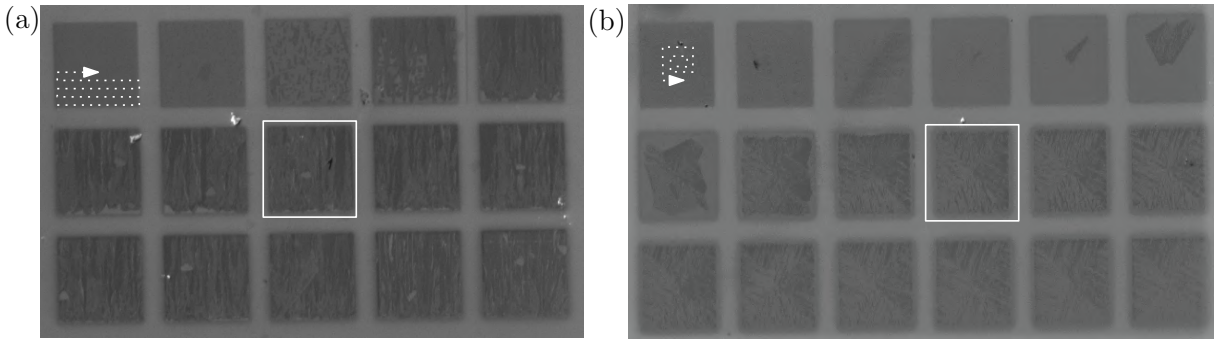

Figure A.3: Dose test with (a) zig-zag and (b) inside-out scanning strategy. Black color corresponds to transformed bcc phase. By contrast observation, the ideal ion doses (from the structures marked by white squares) are chosen to fabricate the structures for analysis.

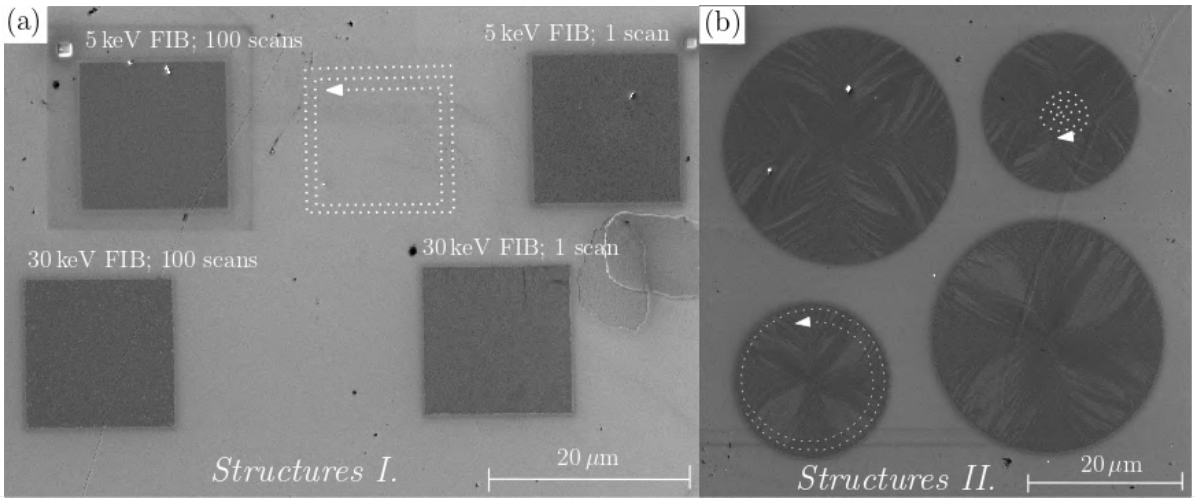

Figure A.4: (a) *Structures I.* written with different combinations of the FIB energy and number of scans. Ion doses used in all squares are the same. The scanning strategy is outside-in. (b) *Structures II.* written by 30 keV and 1 scan. Bottom circles are scanned outside-in and upper ones inside-out.

Second experiments were done in *Structures II.* [see Figure A.4 (b)] – four circles combining two scanning strategies (inside-out, outside-in) and two diameters (20 μm and 30 μm).

Significant contrast differences were recognized in circles fabricated by different scanning strategies by the SEM inspections of *Structures II.* In inside-out scanned circles, we observed four distinguishable 90° circular sectors separated by white lines. These sectors are best observable during the tilt test presented in the Section A.3. Nothing similar is visible for outside-in scanning strategy. Because it is not clear if the origin of these sectors is in the crystallography or in the scanning manner of the microscope, we fabricated *Structures III.* [see Figure A.5 (a)] – 5 circles scanned inside-out and combining two directions of scanning (clockwise, counterclockwise) with three starting angles of scanning ($0°, 45°, 90°$ against the horizontal direction). With circles we observed differences in structures scanned inside-out and outside-in. Therefore we added to the last line in *Structures III.* three inside-out scanned squares (outside-in square is part of *Structures III.*).

We observed unexpected behavior for the square rotated by 45° from the horizontal (100) direction. Two other squares ($0°, 90°$) are divided into four regions by two square diagonals. In the case of 45° rotated square, we observed eight distinguishable triangular regions. In addition to diagonal dividing there is also separation around the lines connecting centers of the opposite sides of the square. For better resolution between all regions we tilted the sample (see the subsection A.3). Unfortunately, the 45° rotated square from *Structures III.* ($15\times15\,\mu m^2$) is not big enough to extract a magnetic signal from eight regions independently. Therefore, we fabricated the same structure with larger dimensions (center of *Structures IV.*). To deeper understand the forming of the eight triangular regions, we added to *Structures IV.* four squares inclined at the angles of $-10°, -5°, 5°, 10°$, from the 45° rotated square. Also in these inclined squares, eight regions are present. However, with the angular deviation of $\pm10°$, the transformed films are less homogeneous, which is manifested by the presence of more needles with different contrast.

In the Chapter 5 we presented EBSD measurements of structures introduced above. As a complementary crystallography measurements we chose XRD (described in the Sec-

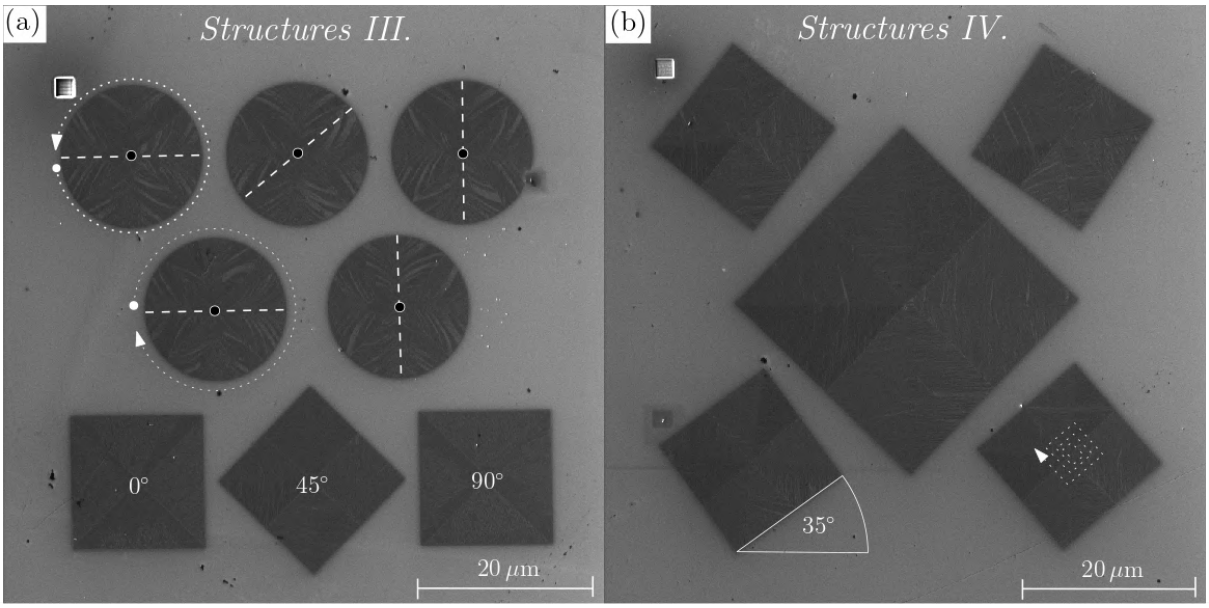

Figure A.5: Structures fabricated by 1 scan 30 keV FIB. (a) *Structures III.* prepared by inside-out scanning strategy. Upper circles are scanned counterclockwise, bottom circles clockwise (marked by dotted circles). The directions where scanning of each sub-circle started and ended are marked by dashed lines. Squares are scanned with $0°, 45°, 90°$ against the horizontal direction. (b) *Structures IV.* prepared by inside-out scanning strategy. Angles of the squares against the horizontal direction vary from 35° to 55°. Big square (45°) is prepared for precise magnetic measurement.

tion 2.2.2). To this purpose, we fabricated five fields of structures with different dimensions and scanning directions (see Figure A.6). The whole XRD story is described in the Section 5.9.

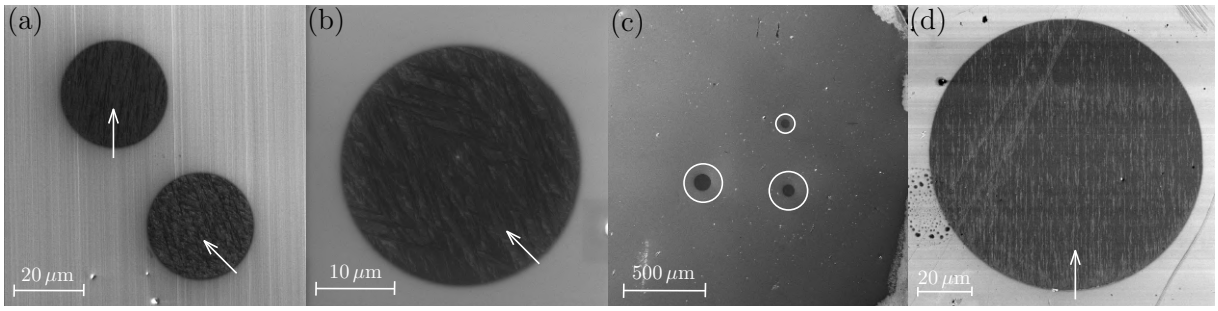

Figure A.6: Structures prepared for XRD measurement. White arrows mark the FIB direction during the zig-zag scanning. In (a), (b), (c) are the structures fabricated at 12 nm $Fe_{78}Ni_{22}$ film on Cu#16 with different diameters and FIB scanning direction. (d) Structure in the thicker 16 nm $Fe_{78}Ni_{22}$ on Cu#15.

A.3. Contrast evolution during tilting the sample

Flajšman already reported about the changing of the contrast with tilting the sample [43]. After the FIB irradiation, we tilted *Structures I. – IV.* to precharacterize them in-situ. In the Figure A.7 the change of SEM contrast is nicely visible. For two circles from

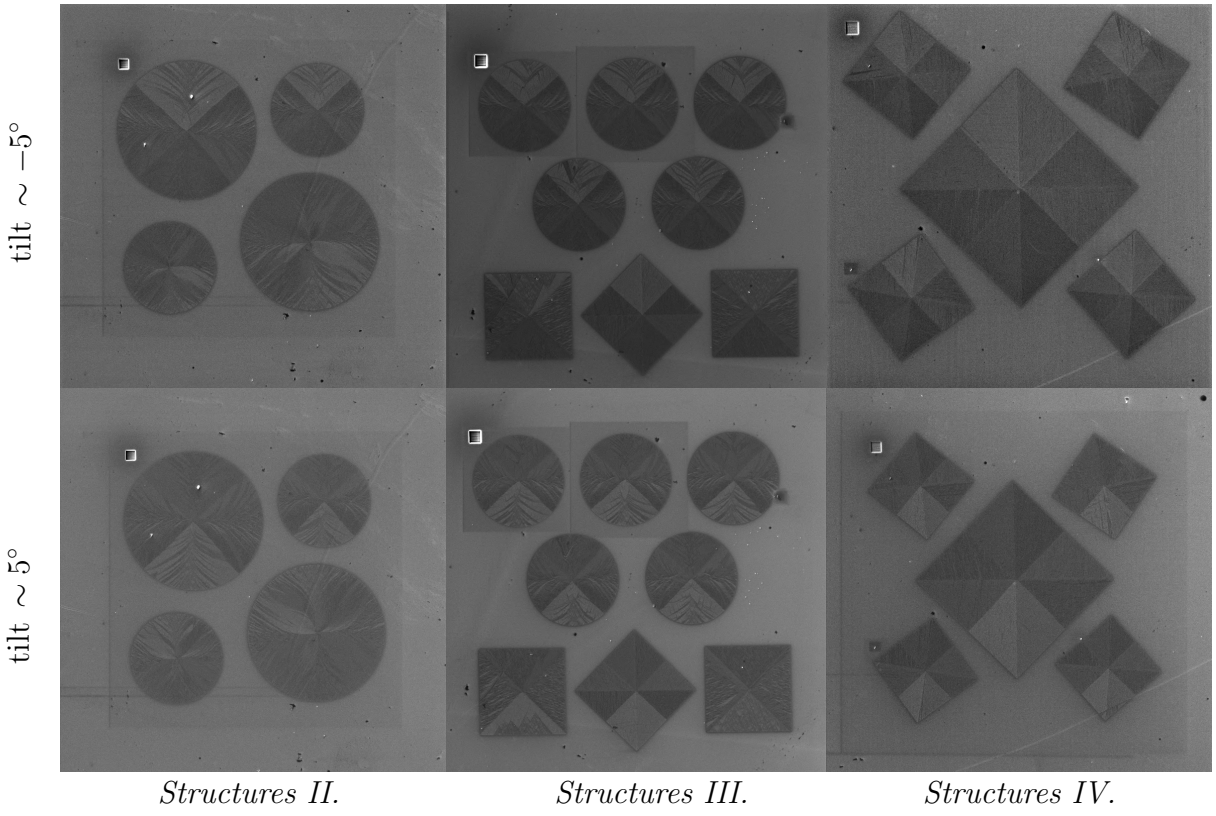

Figure A.7: Structures fabricated in the subsection A.2 observed under the tilt $\sim \pm 5°$. Alternating contrast is visible. The textures of transformed structures are more significantly visible.

Structures II. scanned inside-out, division to four quadrants is present. For each quadrant, so-called *tree texture* is recognized. We performed a tilt test also after the in-plane 90° rotation. Then the contrast change appeared in the second two quadrant (left, right in the Figure A.7). For circles from *Structures III.* no dependency on starting direction is observed. For 45° rotated square from *Structures III.* and *Structures IV.* eight triangular homogenous regions are observed.

To better understand the contrast evolution during the varying of the tilt, we focused on one of the squares from *Structures I.* We acquired series of images in the tilt range from $-10°$ to 10° with fine step (chosen images are in the Figure A.8). Consequently, we performed data analysis in the software ImageJ. We took the mean values of the intensity histogram from the bottom and upper triangular region and deducted them. The extremes of this difference are from pictures acquired at $-5°$ and 5° tilt.

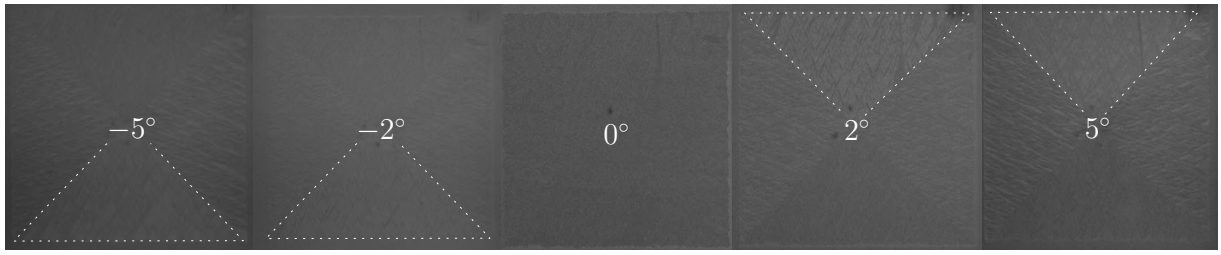

Figure A.8: Tilt test of square (30 keV, 1 scan) from *Structures I.* Images of five different tilts are presented. By the dotted lines are marked the areas used in data processing.

B. Orientation domain analysis

In this appendix, we attach complementary tables, which were used during the observations of the domain distribution in the Section 5.3.

Domain distribution analysis for square fabricated by single scan 30 keV FIB

Table B.1: Summary of the orientation distribution analysis (structure fabricated by single scan 30 keV FIB) from the EBSD measurement of *Structures I.* done by crystal orientation cumulative charts. Data from the structure were cropped to four areas listed in the column Region. In the second column are reference orientations in Euler angles defined by Bunge notation. In the last column are fractions of pixels from the region with the misorientation lower then 2.1°. Corresponding data are presented in the Figure 5.5.

Region	Reference orientation	Misorientation less then 2.1°
Top [Figure 5.5 (b)]	(6°, 89°, 183°)	Purple (40%)
Right [Figure 5.5 (c)]	(206°, 3°, 71°)	Blue (42%)
Bottom [Figure 5.5 (d)]	(6°, 90°, 175°)	Green (55%)
Left [Figure 5.5 (e)]	(173°, 177°, 77°)	Yellow (56%)

Domain distribution analysis for square fabricated by single scan 5 keV FIB

Table B.2: Summary of the orientation distribution analysis (structure fabricated by single scan 5 keV FIB) done by crystal orientation charts. Data from the structure was cropped to four areas listed in the column Region. In the second column are reference orientations in Euler angles defined by Bunge notation (later was realized, that both orientation are almost equivalent). In the last column are the most common domains from the corresponding regions with their percentage occurrence. They are named by the color of the domains representatives from the Figure 5.6.

Region	Reference orientation	2 most common domains
Left [Figure 5.6 (a)]	(44°, 44°, 178°)	Yellow (75%), Blue (8%)
Top [Figure 5.6 (b)]	(60°, 45°, 0°)	Yellow (58%), Blue (21%)
Right [Figure 5.6 (c)]	(44°, 44°, 178°)	Yellow (29%), Blue (30%)
Bottom [Figure 5.6 (d)]	(60°, 45°, 0°)	Yellow (41%), Blue (26%)